

Summer 2012

## Documenting Magnatic Processes at Filicudi Island, Aeolian Arc, Italy: Integrating Quantitative Modeling and Plagioclase Textural and in situ Compositional Data

Michelle Harris  
*Central Washington University*

Follow this and additional works at: <https://digitalcommons.cwu.edu/etd>



Part of the [Geology Commons](#), [Geomorphology Commons](#), [Geophysics and Seismology Commons](#), [Mineral Physics Commons](#), and the [Volcanology Commons](#)

---

### Recommended Citation

Harris, Michelle, "Documenting Magnatic Processes at Filicudi Island, Aeolian Arc, Italy: Integrating Quantitative Modeling and Plagioclase Textural and in situ Compositional Data" (2012). *All Master's Theses*. 1450.

<https://digitalcommons.cwu.edu/etd/1450>

This Thesis is brought to you for free and open access by the Master's Theses at ScholarWorks@CWU. It has been accepted for inclusion in All Master's Theses by an authorized administrator of ScholarWorks@CWU. For more information, please contact [scholarworks@cwu.edu](mailto:scholarworks@cwu.edu).

DOCUMENTING MAGMATIC PROCESSES AT FILICUDI ISLAND,  
AEOLIAN ARC, ITALY: INTEGRATING QUANTITATIVE  
MODELING AND PLAGIOCLASE TEXTURAL  
AND *IN SITU* COMPOSITIONAL DATA

---

A Thesis  
Presented to  
The Graduate Faculty  
Central Washington University

---

In Partial Fulfillment  
of the Requirements for the Degree  
Master of Science  
Geology

---

by  
Michelle Harris  
July 2012



CENTRAL WASHINGTON UNIVERSITY

Graduate Studies

We hereby approve the thesis of

Michelle Harris

Candidate for the degree of Master of Science

APPROVED FOR THE GRADUATE FACULTY

\_\_\_\_\_

\_\_\_\_\_  
Dr. Wendy Bohrson, Committee Chair

\_\_\_\_\_

\_\_\_\_\_  
Dr. Chris Mattinson

\_\_\_\_\_

\_\_\_\_\_  
Dr. Michael Rowe

\_\_\_\_\_

\_\_\_\_\_  
Dean of Graduate Studies

ABSTRACT

DOCUMENTING MAGMATIC PROCESSES AT FILICUDI ISLAND,  
AEOLIAN ARC, ITALY: INTEGRATING QUANTITATIVE  
MODELING AND PLAGIOCLASE TEXTURAL  
AND *IN SITU* COMPOSITIONAL DATA

by

Michelle Harris

July 2012

Documenting the physiochemical processes that influence magma composition is critical for forecasting eruption styles and managing volcanic hazards. Compositional diversity of magmas develops through recharge, assimilation, and fractional crystallization (RAFC) within subvolcanic magma reservoirs. Integration of MELTS modeling, whole rock, plagioclase textural and *in situ* elemental and isotopic data from Filicudi Island, Italy allow documentation of the roles and relative chronology that RAFC played in the magmatic evolution and elucidates aspects of the magma plumbing system structure.

Results indicate a polybaric magma plumbing system with deeper (3.5-4 kilobars) and shallower (0.5-1.2 kilobars) storage regions. Within the deeper system, FC acted to differentiate magma, while water contents acted to suppress plagioclase growth. Differentiated magma intruded to shallower levels, where plagioclase crystallized rapidly resulting in monotonous textures and high anorthite contents. Within the shallower

system, recharge from the deeper system and continued FC contributed to the compositional diversity observed on Filicudi Island.

## ACKNOWLEDGMENTS

I would like to begin my acknowledgments by thanking my advisor, Dr. Wendy Bohrson. She brought me back to the Pacific Northwest and instilled a long-term love for volcanoes, igneous petrology, and geochemistry. She has not only inspired me to be a better scientist, but also has taught me to aim high in my future goals. I hope to be half the professor she is someday. I would have never found such an amazing advisor without the help of Dr. Paul Hoskin of the University of Auckland, so to him I also give special thanks.

I would also like to thank Dr. Chris Mattinson, of Central Washington University, one of my committee members, for strengthening my love of petrography and spending many long hours with me discussing and reviewing my project. Many thanks also go to Michael Rowe of Washington State University, my other committee member, for taking the time to teach me how to use the Electron Microprobe and providing support with my thesis.

I have received substantial analytical help from Dr. Adam Kent, Dr. Andy Ungerer, and Matt Lowen at Oregon State University and Dr. Charles Knaack, Dr. John Wolff, and Scott Boroughs at Washington State University. Many thanks also go to Dr. Frank Ramos and his wife of New Mexico State University for opening their home to me. I'd also like to thank him and his graduate student Sean Scott, for spending their Saturdays teaching me about radiogenic isotopes. Moreover, I like to thank my colleague Aaron Mayfield for all the help and for the collaboration with the MELTS modeling.

Finally, none of this would be possible without my family and friends. To them I want to say thank you for supporting my decision to go back to school and always believing in me. I owe the most to my mother, MaryAnn Harris, who not only let me live in her basement rent-free for a year prior to starting my MS, but also never stopped telling me that I can be whatever I want to be. I also especially want to thank my siblings, Monica Harris, Dian Poyssick, Scott Harris, and Alli Poyssick, for understanding I will forever be a broke college student and loving me anyway. To my father, Alexander Harris (RIP), I want to thank you for instilling in me a continuing scientific curiosity and deep love of the outdoors. Most of all, I owe completion of this project to Kevin Thomas. Without his devoted love, caring, and support, I would have been lost.

Due appreciation goes to the National Science Foundation, Sigma Xi, and Central Washington University for funding this project.

## TABLE OF CONTENTS

Chapter		Page
I	INTRODUCTION .....	1
II	BACKGROUND .....	6
	Geologic Setting .....	6
	Filicudi Island .....	7
	Crystal Growth Stratigraphy .....	18
	Quantitative Modeling .....	24
III	METHODS .....	25
	Whole Rock Analysis .....	25
	<i>In situ</i> Plagioclase Textural and Compositional Analysis .....	30
	MELTS Modeling .....	34
IV	RESULTS .....	36
	Overview .....	36
	Whole Rock Major and Trace Element Data .....	36
	Whole Rock Sr and Nd Isotope Data .....	48
	Petrography .....	50
	<i>In situ</i> Plagioclase Data .....	64
	MELTS Models .....	90
V	DISCUSSION .....	92
	Overview .....	92
	Stratigraphy .....	94
	Magma Chamber Processes .....	94
	Magma Chamber Structure and Evolution .....	101
VI	CONCLUSIONS .....	107
	Future Work .....	109
	REFERENCES .....	110

TABLE OF CONTENTS (Continued)

Chapter	Page
APPENDIXES.....	Back Pocket
Appendix A- Raw Electron Microprobe Data .....	Back Pocket
Appendix B- Raw Trace Element Data .....	Back Pocket
Appendix C- NDIC Images and Major/Trace Traverses.....	Back Pocket
Appendix D- Raw Sr Isotope Data .....	Back Pocket
Appendix E- NDIC Images and Major $^{87}\text{Sr}/^{86}\text{Sr}$ Traverse .....	Back Pocket
Appendix F- Petrography.....	Back Pocket

## LIST OF TABLES

Table		Page
1	Stratigraphic column listing eruptive groups and lithostratigraphic units from youngest to oldest .....	11
2	Methods, results and interpretations of previous authors who have studied Filicudi Island. ....	16
3	Whole rock major and trace element data, calc-alkaline volcanic rocks from Filicudi Island, Italy. ....	44
4	Whole rock Sr and Nd isotope data. ....	48
5	Modal abundances of volcanic rocks from Filicudi Island. ....	51
6	Five textural types identified in Filicudi volcanic rock. ....	65
7	Stratigraphic sequence of groups and rock names documented for each sample .....	71
8	<i>In situ</i> plagioclase trace element averages and standard deviations .....	80
9	<i>In situ</i> plagioclase $^{87}\text{Sr}/^{86}\text{Sr}$ data for Groups 2, 4, and 5. ....	86
10	Summary of interpretations and evidence for magmatic processes for Groups 2, 4, and 5. ....	93



## LIST OF FIGURES

Figure		Page
1	Map showing location of Aeolian Archipelago, Southern Tyrrhenian Sea, Italy after Santo & Peccerillo (2008).....	2
2	Geologic map and stratigraphy of Filicudi Island modified from Tranne <i>et al.</i> (2000). .....	3
3	IUGS Volcanic Rock Classification (LeBas <i>et al.</i> , 1986) for Filicudi, Alicudi, and Salina whole rock samples .....	4
4	Whole rock SiO <sub>2</sub> wt. % plotted against whole rock (a) MgO, (b) FeO, (c) CaO, (d) Al <sub>2</sub> O <sub>3</sub> , (e) K <sub>2</sub> O, (f) Na <sub>2</sub> O, (g) TiO <sub>2</sub> and (h) P <sub>2</sub> O <sub>5</sub> wt. %. .....	39
5	Whole rock SiO <sub>2</sub> wt. % plotted against whole rock compatible trace elements (a) Ni, (b) Sc, (c) Cr, and (d) Sr ppm for Filicudi samples.....	40
6	Whole rock SiO <sub>2</sub> wt. % plotted against whole rock incompatible trace elements (a) Rb, (b) Ba, (c) Th, (d) U, (e) Zr, and (f) Nb ppm for Filicudi samples .....	41
7	Whole rock SiO <sub>2</sub> wt. % plotted against whole rock Rare Earth Elements (a) La, (b) Nd, (c) Eu, and (d) Lu ppm for Filicudi samples.....	42
8	Chondrite-normalized REE diagrams for Filicudi Island.....	43
9	Whole rock isotope results for Filicudi, Alicudi and Salina .....	49
10	Cross-polar (XP) photomicrograph of basalt, Fil 10-13, from Group 2 on Filicudi.....	52
11	Cross-polar (XP) photomicrograph of plagioclase with clinopyroxene inclusion in basalt, Fil 10-13, from Group 2 on Filicudi.....	53
12	Cross-polar (XP) photomicrograph of basalt/basaltic andesite Fil 10-15, from Group 2 on Filicudi .....	54

## LIST OF FIGURES (Continued)

Figure		Page
13	Cross-polar (XP) photomicrograph of basaltic andesite, Fil 10-6, from Group 2 on Filicudi.....	55
14	Photomicrographs of anhedral hornblende phenocrysts showing oxides rims in plane polar light (left) and cross-polar light (right).....	56
15	Cross-polar (XP) photomicrograph of plagioclase exhibiting core with boxy sieving and simple twinning, and euhedral rims .....	57
16	Cross-polar (XP) photomicrograph of basalt, Fil 10-2, from Group 2a on Filicudi.....	58
17	Cross-polar (XP) photomicrograph of plagioclase phenocrysts displaying anhedral, embayed, and monotonous cores, while rims show subhedral monotonous growth .....	58
18	Cross-polar (XP) photomicrograph of basaltic andesite, Fil 10-1, from Group 4 on Filicudi.....	59
19	Cross-polar (XP) photomicrograph of plagioclase phenocrysts displaying crystal bending, highly sieved cores (both dusty and spongy), and fairly anhedral monotonous rims .....	60
20	Cross-polar (XP) photomicrograph of andesite, Fil 10-3, from Group 4 on Filicudi. ....	61
21	Cross-polar (XP) photomicrographs of the two populations of plagioclase phenocrysts in andesite Fil 10-3, of Group 4 from Filicudi.....	62
22	Cross-polar (XP) photomicrograph of andesite, Fil 10-10, from Group 5 on Filicudi.....	63
23	Cross-polar (XP) photomicrograph of plagioclase phenocrysts displaying euhedral highly sieved to patchy/spongy cores with glassy inclusions and oscillatory or monotonously zoned rims.....	63
24	Example of textural type #1 (monotonous).....	66

## LIST OF FIGURES (Continued)

Figure		Page
25	Example of textural type #2 (complex oscillatory) .....	66
26	Example of textural type #3 (sieved/patchy core with oscillatory/ monotonous rim) .....	67
27	Example of textural type #4 (monotonous/oscillatory core with sieved/patchy rim).....	67
28	Example of textural type #5 (sieved/patchy core and sieved/ patchy rims).....	68
29	Whole rock SiO <sub>2</sub> wt. % plotted against plagioclase An mol% ranges for Groups 2, 4, and 5 on Filicudi Island .....	69
30	Whole rock SiO <sub>2</sub> wt. % plotted against average plagioclase An mol % for all samples in Groups 2, 4, and 5 on Filicudi Island. ....	70
31	Delta An (rim-core) plotted against core An mol% values reported by composition and group.....	72
32	Whole rock SiO <sub>2</sub> wt.% plotted against plagioclase trace elements (a) Mg (ppm), (b) Ti (ppm), (c) FeO (wt. %), (d) Sr (ppm), (e) Ba (ppm), and (f) La (ppm).....	74
33	Whole rock SiO <sub>2</sub> wt.% plotted against average plagioclase trace elements with standard deviations (a) Mg (ppm), (b) Ti (ppm), (c) FeO (wt. %), (d) Sr (ppm), (e) Ba (ppm), and (f) La (ppm).....	79
34	Plagioclase An (mol%) content plotted against plagioclase trace elements (a)Mg (ppm), (b) Ti (ppm), (c) FeO (wt. %), (d) Sr (ppm), (e) Ba (ppm), and (f) La (ppm).....	83
35	In situ plagioclase <sup>87</sup> Sr/ <sup>86</sup> Sr isotopes plotted against whole rock SiO <sub>2</sub> (wt. %) for Groups 2, 4, and 5.....	85
36	Delta (rim-core) <sup>87</sup> Sr/ <sup>86</sup> Sr values plotted on a bar graph for samples from Groups 2, 4, and 5.....	89

## LIST OF FIGURES (Continued)

Figure		Page
37	Plagioclase in situ Sr <sup>87</sup> Sr/ <sup>86</sup> Sr values plotted against An (mol %) for cores (filled symbols), rims (unfilled symbols), and intermediates (crosses).....	90
38	MgO (wt%) plotted against SiO <sub>2</sub> (wt. %) for the polybaric best-fit MELTS runs 12 and 15 and Filicudi whole rock data.....	91
39	Whole rock REE divided by their lowest values.....	96
40	Rare Earth Elements Dy/Yb and La/Yb plotted against whole rock SiO <sub>2</sub> .....	97
41	Schematic illustrations of the polybaric magma plumbing system beneath Filicudi Island associated with Groups 2, 4, and 5. ....	106

## CHAPTER I

### INTRODUCTION

Documenting the physiochemical processes that influence magma composition is critical for forecasting eruption style and managing volcanic hazards. Although studies have documented how compositional diversity develops in magmas on Earth, controversy remains regarding the roles that recharge, assimilation, and fractional crystallization (RAFC) play in magmatic evolution.

The recent to active Aeolian Archipelago in the Southern Tyrrhenian Sea, Italy (Figure 1) has been the focus of numerous studies because of the large geochemical variability observed within the volcanic arc, emplaced on continental crust (Francalanci & Santo, 1993, Nazzareni *et al.*, 2001, Santo & Peccerillo, 2008, Santo, 2000, Santo *et al.*, 2004, Santo *et al.*, 1995). The seven islands and several seamounts vary compositionally from tholeiitic to calc-alkaline to shoshonitic to potassic alkaline, providing an ideal location in which to study the effects of crustal magmatic processes on compositional evolution (Francalanci & Santo, 1993).

Filicudi Island, in the western sector of the arc, is made up of several geometrically complicated overlapping eruptive centers (Figure 2) that have erupted a compositional range from calc-alkaline basalt (51 wt. % SiO<sub>2</sub>) to high-K andesite (62 wt. % SiO<sub>2</sub>) (Figure 3) that cannot be simply related by fractional crystallization, implying crustal contamination and/or recharge played vital roles. Previous geochemical studies of Filicudi Island have related its magmatic and compositional evolution to the presence of

several small, separated magma chambers that experienced both fractional crystallization and assimilation processes (Santo *et al.*, 2004). However, previous studies have been restricted to whole rock methods, which yield data about the average characteristics of the components that comprise the rock, including crystals and groundmass. *In situ* studies of minerals can document data on a smaller spatial scale that may also provide a chronologic record of processes that influence compositional diversity (e.g., Davidson *et al.*, 2005).

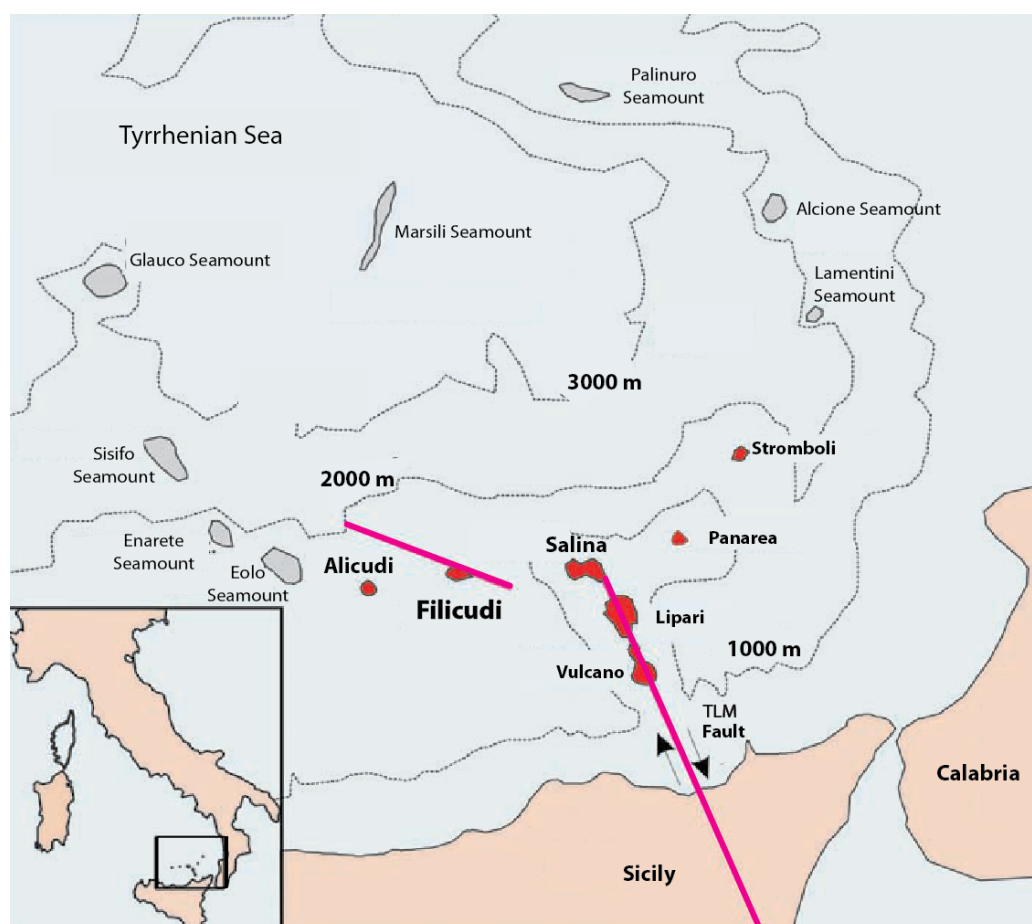


Figure 1: Map showing location of Aeolian Archipelago, Southern Tyrrhenian Sea, Italy after Santo & Peccerillo (2008). Filicudi and the other main volcanic islands are shown in red while seamounts are shown in grey. The Tindari-Letojanni-Malta (TLM) tectonic line is shown in pink. Inset shows the approximate location of the Aeolian arc in relation to mainland Italy and Sicily.

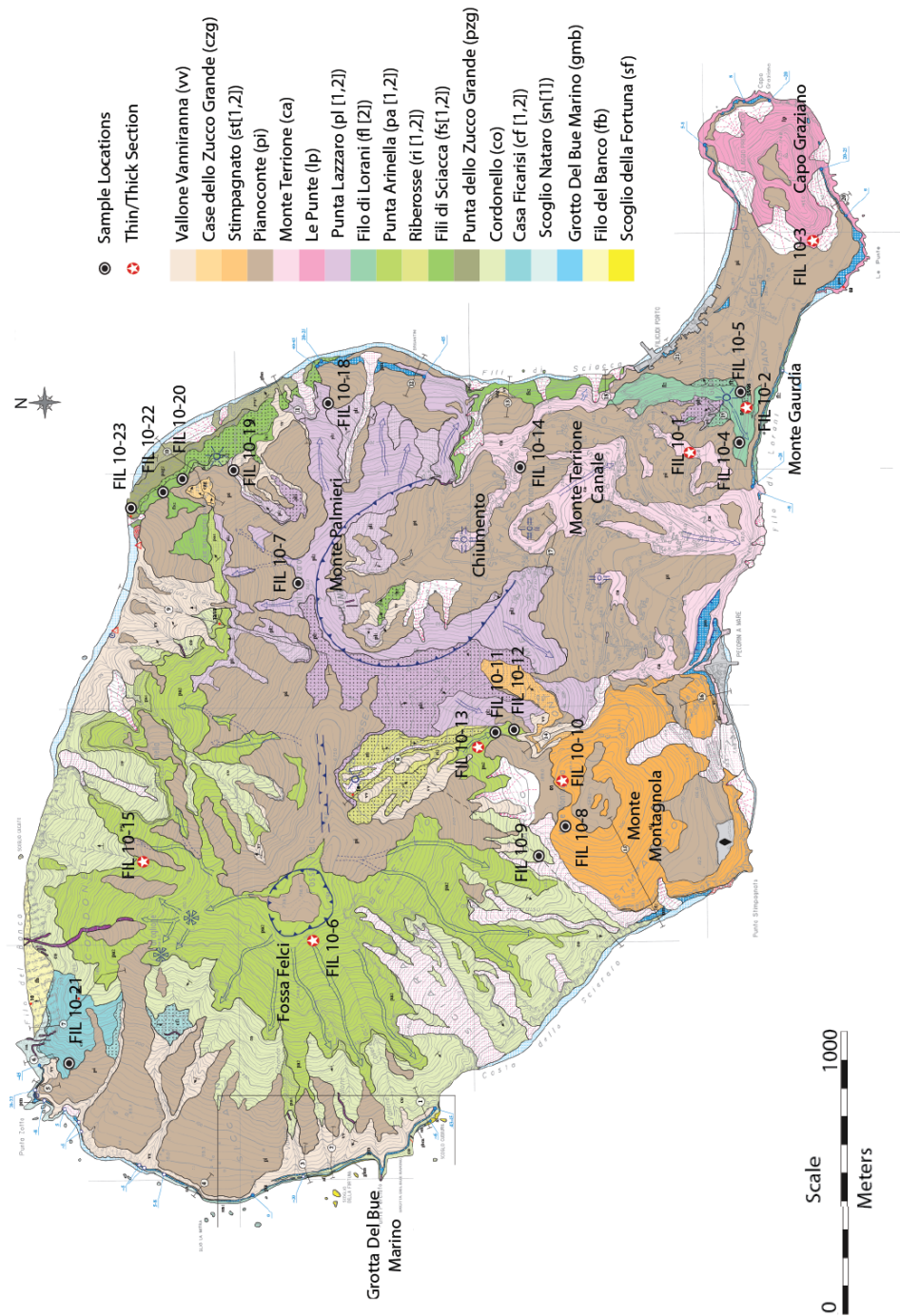


Figure 2: Geologic map and stratigraphy of Filicudi Island modified from Tranne *et al.* (2000). Colors correspond to different eruptive units and are listed in stratigraphic order from youngest to oldest in key. Black symbols represent locations of sample collection for this study. Samples marked with red stars represent the seven samples chosen for *in situ* plagioclase analysis. Arrows on map depict direction of lava flow, while snowflake shape depicts locations of volcanic necks or plugs.

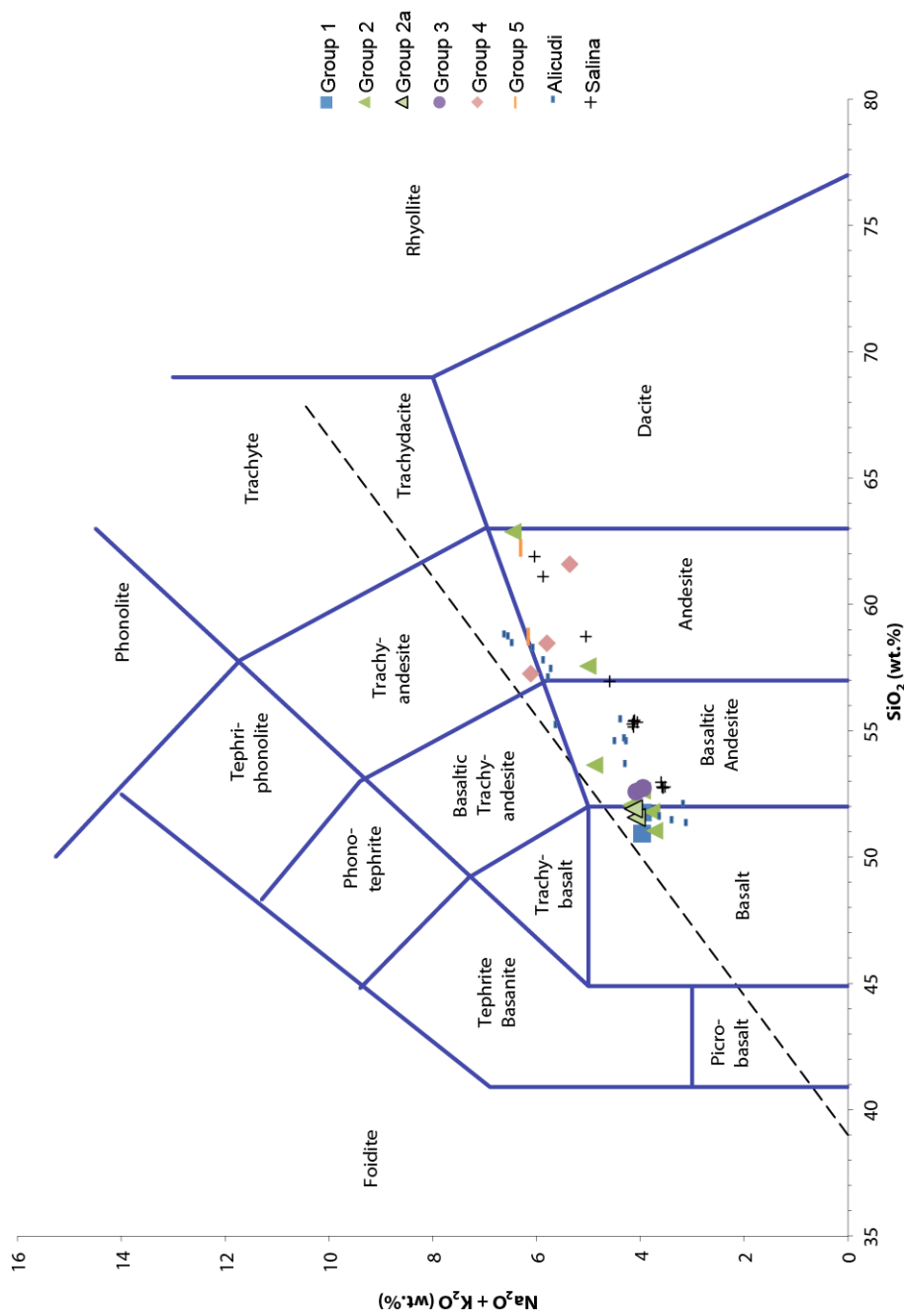


Figure 3: IUGS Volcanic Rock Classification (LeBas *et al.*, 1986) for Filicudi, Alicudi, and Salina whole rock samples. Groups were developed using the relative stratigraphy of Tranne *et al.* (2000). See Table 1 (Stratigraphic column) for detailed description of which samples correspond which groups. Alicudi data and Salina data are shown for comparison.



The objective of my study is to integrate new whole rock data with plagioclase textural and *in situ* major and trace element and isotopic data to reveal compositional and isotopic heterogeneities at the sub-grain scale. At the core of this investigation is the incorporation of MELTS modeling with the *in situ* data, which will allow for documentation of the quantitative roles and relative chronology of the RAFC processes identified. Understanding the chronological order of the processes that affected Filicudi's magmatic evolution will allow for theories regarding magma chamber dynamics and triggering mechanisms of individual eruption cycles (e.g., Davidson *et al.*, 2007; Ginibre *et al.*, 2007).

CHAPTER II  
BACKGROUND  
Geologic Setting

Filicudi Island is one of seven major islands (Alicudi, Salina, Lipari, Vulcano, Panarea, Stromboli) and eight seamounts (Lamentini, Alcione, Palinuro, Marsili, Glauco, Sisifo, Enarete, Eolo) that make up the active Aeolian archipelago in the southern Tyrrhenian Sea, Italy (Barberi *et al.*, 1974) (Figure 1). The Aeolians sit on a ~15-20 km thick continental margin between the NW dipping Ionian Sea crust and Italy's southwestern tip (Calabria) (Barberi *et al.*, 1974). The NW dipping Mediterranean subduction zone represents the on-going collision of the African and European plates.

The main tectonic features of the Aeolian archipelago have been described in detail elsewhere (Morelli *et al.*, 1975) and will only be briefly summarized here. Convergence between the African and European plates has been steadily ongoing since the break up of Pangaea (~200 million years ago). Approximately 10 Ma, the African plate began rotating counterclockwise relative to the European plate causing back-arc extension and the opening of the Tyrrhenian sea (Morelli *et al.*, 1975). Presently, extension has ceased, and shortening is instead being accommodated by a diffuse transtensional zone called the Tindari-Letojanni-Malta Escarpment fault (TLM) (Santo & Peccerillo, 2008) (Figure 1).

The Aeolian Islands are the focus of numerous studies because the complex tectonic regime associated with the TLM fault appears to sharply influence the geochemical, petrological, and volcanic characteristics of each island (Villari & Nathan,

1978). The NNW-SSE striking TLM fault acts to divide the Aeolians into three groups: the Western, Central, and Eastern segments. Each segment can be associated with distinct geochemical domains ranging from calc-alkaline (CA) and high-K calc-alkaline (HKCA) to shoshonitic (SHO) and potassic (KS) rocks (Francalanci & Santo, 1993). The Western sector includes the apparently extinct islands of Alicudi, Filicudi, and Salina. Typical subduction-related CA to HKCA magmas characterize all three islands, and their rocks are among the oldest in the arc. The Central sector includes the active islands of Lipari and Vulcano. These two islands display compositional ranges from HKCA to SHO and are characterized by their alignment along the TML fault. The island of Salina has been included in the Central sector by some (De Rosa *et al.*, 2003, Villari & Nathan, 1978) because of its alignment along the TML fault, and is included in the Western sector by others because it straddles the geochemical boundary between CA and HKCA rocks (Francalanci & Santo, 1993, Santo, 2000, Santo *et al.*, 2004, Santo *et al.*, 1995). The Eastern segment includes the islands of Panarea and active Stromboli, which predominately erupt SHO to KS rocks (Villari & Nathan, 1978). The increasingly potassic nature of the lavas from west to east along the arc has been attributed to the steepening in time and space of the Ionian subducting slab (Villari & Nathan, 1978).

#### Filicudi Island

Filicudi Island was first mapped by Cortese and Sabatini (1892) and has been the focus of numerous stratigraphic, petrologic and geochemical studies since (De Rosa *et al.*, 2003, Francalanci & Santo, 1993, Manetti *et al.*, 1995, Santo, 2000, Santo *et al.*,

2004, Santo *et al.*, 1995, Tranne *et al.*, 2000, Villari & Nathan, 1978). The island of Filicudi is located on the western side of the Aeolian arc and was formed during the Pleistocene over an 18 km thick crust (Morelli *et al.*, 1975). The island rises 2000 m from the seafloor and reaches 774 m above sea level (Fossa Felci), leaving 1226 m of the island submerged (Francalanci & Santo, 1993). The non-active, small (9.5 km<sup>2</sup>), composite volcano has a complex volcanic structure that includes geometrically complicated, overlapping eruptive centers (e.g. Scoglio Cuddura, Fossa Felci, Monte Gaurdia, Monte Palmieri, Capo Grazino, Monte Terrione, Monte Montagnola) (Tranne *et al.*, 2000) (Figure 2). The volcano has erupted calc-alkaline basalts to high-K andesites and rare dacites in the form of lava flows, pyroclastic flows, thick mudflows, and a few domes that formed from dominantly Strombolian-type activity (Villari & Nathan, 1978).

### *Stratigraphy*

The abundance of vegetation and lack of fresh outcrops on the island hamper efforts to clearly document the stratigraphy of Filicudi. As a result, different stratigraphic, geochronologic (e.g. K/Ar, <sup>40</sup>Ar/<sup>39</sup>Ar), and eruptive histories have been proposed (De Rosa *et al.*, 2003, Manetti *et al.*, 1995, Santo *et al.*, 1995, Tranne *et al.*, 2000).

On the basis of <sup>40</sup>Ar/<sup>39</sup>Ar data, volcanic activity ranges in age from 1.02 to 0.04 Ma (Francalanci & Santo, 1993, Santo, 2000, Villari & Nathan, 1978), making Filicudi Island the oldest island in the Aeolians. However, a more recent K/Ar age of 211± 5 ka has been reported on a lava from same stratigraphic position as that previously dated at

1.02 Ma by  $^{40}\text{Ar}/^{39}\text{Ar}$  dating (De Rosa *et al.*, 2003); this introduces some uncertainty regarding the ages of the oldest sampled rocks on the island.

The latest stratigraphic study based on marine terrace identification has documented several formations belonging to three synthemms (Paleofilicudi, Punta Zotta, and Punta Perciato) and two supersynthemms (Cala Fico and Punte Le Grotticelle) (Tranne *et al.*, 2000). Within the synthemms, lithosomes are separated into 6 Groups based on eruptive stratigraphy and are documented with like colors on the geologic map (Figure 2). The Tranne *et al.* (2000) stratigraphic classification system has been adopted for this study.

Table 1 has been provided to aid in understanding the similarities and differences of the relative stratigraphy of the different lithosomes. Column 1 contains the 6 Groups based on Tranne *et al.* (2000); columns 2 and 3 contain the samples from this study within their associated informal lithostratigraphic unit name adopted from Tranne *et al.* (2000). Within each Group, the stratigraphic relationship of the informal lithostratigraphic units (formations) remains unclear. Column 4 is provided for a comparison between the relative stratigraphy of Tranne *et al.* (2000) and Santo (2000). Cycle numbers listed from 1-4 reflect the stratigraphy that Santo (2000) developed using field, petrological, geochemical, isotopic investigations (details to follow), whereas column 5 lists all ages in ka documented by different authors for selected informal lithostratigraphic units. For example, the Punta dello Zucco Grande formation, documented by Santo *et al.* (1995) as being 1.02 Ma and by Santo (2000) as belonging to Cycle I, is instead classified in this study as being within Group 2 eruptive products

because of the K/Ar age of  $211 \pm 5$  ka (De Rosa *et al.*, 2003) and a more recent  $^{40}\text{Ar}/^{39}\text{Ar}$  age of  $192.1 \pm 2.2$  ka (Creamer *et al.*, 2011). Accordingly for this study, the first 3 columns will be used to interpret the relative stratigraphy on Filicudi Island in accordance with the geologic map of Tranne *et al.* (2000) and radiometric ages of De Rosa *et al.* (2003) and Creamer *et al.* (2011).

Table 1. Stratigraphic column listing eruptive groups and lithostratigraphic units from youngest to oldest.

Group based on Tranne <i>et al.</i> (2000)	Sample # based on this study	Lithostratigraphic units based on Tranne <i>et al.</i> (2000)		Cycle based on Santo (2000)	Age (ka) <sup>(1)(2)(3)</sup>
5- Monte Montagnola		vv	Vallone Vanniranna		
		czg	Case dello Zucco Grande		
	10-8 <b>10-10</b>	st (1,2)	Stimpagnato	III	80.5 ± 9.4 (3)
		pi	Pianoconte		
4- Capo Graziano	<b>10-1</b> 10-14	ca	Monte Terrione	III	166 ± 4 (2) 170 ± 4 (2)
	<b>10-3</b>	lp	Le Punte	III	190 ± 30 (1)
	10-7 10-18 10-17	pl (1,2,3)	Chiumento 2 Punta Lazzaro	III	250 ± 80 (1)
2a- Monte Gaurdia	<b>10-2</b> 10-4 10-5	fl2	Filo di Lorani	III	190 ± 70 (1) 210 ± 70 (3)
	<b>10-6</b> 10-11 10-12 <b>10-13</b> <b>10-15</b>	pa2	Punta Arinella	III	
		ri (1,2)	Riberosse		
2- Fossa Felici	10-20 10-22	fs2	Fili di Sciacca	III	230 ± 70 (1)
	10-23	pzg(1, 2)	Punta dello Zucco Grande	I	1020 ± 100 (1) 211 ± 5 (2) 192.1 ± 2.2 (3)
	10-9	co	Cordonello	III	219 ± 5 (2)
	10-21	cf (1, 2)	Casa Ficarisi	II	205.5 ± 3.9 (3) 208.7 ± 2.8 (3)
	10-16	sn(1)	Scoglio Nataro	II	390 ± 140 (1)
1- Punta Zotta		gmb	Grotto Del Bue Marino	II II	
		fb	Filo del Banco	IV	182.2 ± 26.7 (3)
		sf	Scoglio della Fortuna	IV	172.8 ± 20.4 (3)
0- Paleofilicudi		*sm	Scoglio di Montenassari	IV	40 ± 40 (1)

(1) Santo *et al.* (1995), (2) DeRosa *et al.* (2003), (3) Creamer *et al.* (2011). \* Scoglio di Montenassari unit not shown on map because its part of the La Canna volcanic neck to the SE of the island. Samples in BOLD were chosen for thick/thin section analyses.

*Petrology and Mineralogy*

Santo *et al.* (2004) provide a detailed petrological and geochemical investigation of Filicudi volcano that will be briefly summarized here. Volcanic rocks from Filicudi are dominated by basalt to andesite and are porphyritic with holocrystalline to hypocrystalline seriate groundmass texture. Phenocrysts make up 30-50 vol %, with plagioclase being the most abundant mineral (20-39 vol %). Plagioclase is present in all samples, and typically shows complex zoning, sieved textures or patchy zoning and a wide range of compositions (An % 50-95).

Basalts also contain clinopyroxene (cpx) and olivine (ol) with rare microphenocrystic orthopyroxene (opx). Clinopyroxene phenocrysts vary in abundance (2-20 vol %), are colorless, have dusty textures, and are euhedral to round. Both augitic and diopsidic compositions have been reported within the same rock. Olivine is generally euhedral in basalts. Moreover, olivine is typically zoned, contains iddingsite rims or is mantled by cpx, providing evidence of disequilibrium. Orthopyroxene is unzoned and rarely shows reaction rims of cpx. Basaltic andesites share the same mineral assemblage as basalts but have less olivine, which is subhedral to corroded, and more orthopyroxene microphenocrysts. High-K andesites contain mostly plagioclase with a bimodal compositional distribution, lesser amounts of cpx and opx, and opaquely altered euhedral biotite and hornblende. Microphenocryst assemblages closely mimic phenocrysts, and accessory minerals include titanomagnetite, ilmenite and apatite.



### *Magmatic Evolution*

A combination of three magmatic processes are known to play vital roles in creating differences in magmatic evolution within volcanoes: Recharge, Assimilation, and Fractional Crystallization, abbreviated RAFC (Spera & Bohrson, 2004). Recharge is the injection of new, hotter magma into an existing magma and has been proposed to trigger volcanic eruptions (Clynne, 1999). Assimilation is the mixing between magma and melt from surrounding rock and typically results in a more silicic magma (Spera & Bohrson, 2004). Fractional Crystallization occurs within most magmas and is the processes of formation and segregation of solid minerals from liquid melt (Spera & Bohrson, 2004).

Investigations of magmatic processes and mechanics that have affected the magmatic evolution of Filicudi Island have been provided by Santo (2000), Santo *et al.* (2004) and Santo and Peccerillo (2008) using major and trace element and isotopic analysis on whole rock volcanic samples and xenoliths; geochemical and temporal variations of stratigraphic sequences; and oxygen isotope variations within clinopyroxene. Table 2 has been provided to aid in the understanding of the different authors' methods, results, and magmatic evolution interpretations on Filicudi Island.

Santo (2000) defined four main cycles of volcanic activity based on a combination of field data and radiometric dating documented by Santo *et al.* (1995). Petrological, geochemical and Sr isotopic investigations revealed that each of the four cycles displayed: repeated reversals to more basic magmas that all displayed common geochemical signatures, an overall increase in SiO<sub>2</sub> content with time, and higher

$^{87}\text{Sr}/^{86}\text{Sr}$  in basaltic rather than andesitic products. The magmatic evolution of calc-alkaline basalts to high-K andesites erupted during the first three cycles was attributed to AFC processes based on similarities in general trends displayed by major and trace elements, differences in Sr isotopic ratios, and the presence of comagmatic cumulate xenoliths (Santo, 2000).

Santo (2000) proposed three models to explain the data documented during the first three cycles of magmatic activity. The first model proposed a Mixing Assimilation Storage Homogenization (MASH) zone, a concept originally proposed by Hildreth and Moorbath (1988), at the base of the crust to explain the mafic magmas displaying common geochemical signatures. In this scenario, primitive calc-alkaline magmas induce melting of wall rock, assimilate this melt, mix and fractionate, allowing production of homogenous parental melt. Small batches of magma then ascended through the crust separately, experiencing different pressure-temperature paths. This model, however, did not explain the different isotopic signatures of the basalts and andesites.

The second model proposed an Assimilation/Equilibrium Crystallization (AEC) interaction model to explain the higher Sr isotope ratios in mafic rocks. Because mafic liquids typically have higher liquidus temperatures, they were able to assimilate more crustal material, allowing the Sr isotopic ratios to become more radiogenic than the high-K andesites (Santo, 2000). This model, however, did not address the common geochemical signatures.

In an attempt to explain the common geochemical signatures of mafic rocks, slight variations in eruptive units, and Sr isotope range, Santo (2000) proposed a third

model in which two distinct chambers existed beneath Filicudi at different crustal depths. The first chamber was under higher pressures and was water-rich, which allowed fractionation of Fe-Mg phases and suppression of plagioclase crystallization. Within this deeper chamber MASH processes were occurring, allowing mafic magmas to acquire similar geochemical signatures. During subsequent ascent through different conduits to shallower levels, plagioclase crystallization commenced, and magmas experienced different episodes of assimilation, mixing, and crystal fractionation leading to the observed geochemical similarities and isotopic differences seen within the first three cycles.

Another research group, Santo *et al.* (2004), proposed a complex, multistage, polybaric evolution in which AFC played a dominant role. Santo *et al.* (2004) used the Santo (2000) data and added new whole rock Sr, Nd and Pb isotopic analyses as well as LILE/HFSE ratios. Findings indicated that cycles shared geochemical similarities and isotopic differences similar to past studies documented by Santo (2000). Again three interpretations were proposed to explain observed trends.

Similarities in geochemical signatures were hypothesized to be a result of magmatic activity occurring separately in time and/or space via similar AFC processes. However, unlike Santo (2000), the observed isotopic variability between basalt and andesite was hypothesized to have originated from a heterogeneous mantle source (i.e., not from assimilation). Santo *et al.* (2004) suggested that Filicudi magmas were derived from a MORB-like mantle source that underwent metasomatism by slab-derived fluids.

Table 2. Methods, results and interpretations of previous authors who have studied Filicudi Island.

Reference	Observations	Interpretation	Comments
Santo (2000)	1. Mafic magmas display common geochemical signatures 2. Slight geochemical differences observed among different eruptive units	1. Common signature result of MASH occurring in deep chamber. Primitive CA magmas induce melting of wall rock, assimilate, mix and fractionate allowing homogenous parental melt to form 2. Slight differences are the result of small batches of magma ascending along distinct P-T paths.	Model does not account for observation 3
Santo (2000)	3. Sr isotopes more radiogenic in mafic rather than silicic rocks	3. Assimilation Equilibrium Crystallization (AEC) proposed to occur in deep chamber. Higher temperatures of mafic melt allowed more assimilation of crustal material	Model does not account for observation 1
Santo (2000)	Observations 1, 2, 3	Two distinct chambers at different depths. In deeper one, Fe-Mg phase fractionate, plagioclase crystallization suppressed. MASH occurred. In shallower chamber, plagioclase formation and AFC occurred.	Model attempts to account for all observations
Santo <i>et al.</i> (2004)	1. Mafic magmas display common geochemical signatures 2. Slight geochemical differences observed	1-2. Similar AFC processes occurring on isotopically distinct magmas within shallow reservoirs (separately in time and/or space).	Model does not account for observation 3
Santo <i>et al.</i> (2004)	3. Higher Sr isotope signatures in mafic rocks	3. Mantle source heterogeneity produced two isotope signatures (low and high Sr) caused by metasomatism from slab-derived fluids.	Model does not account for observation 1
Santo <i>et al.</i> (2004)	Observations 1, 2, 3	Complex, multistage, polybaric evolution. Low $^{87}\text{Sr}/^{86}\text{Sr}$ magmas ascended to shallow levels and experienced AFC processes. Later a tectonic regime shift allowed high $^{87}\text{Sr}/^{86}\text{Sr}$ magmas from deep reservoir to mix with the low $^{87}\text{Sr}/^{86}\text{Sr}$ magmas within the shallow reservoir.	Model attempts to account for all observations
Santo and Peccerillo (2008)	1. Negative $^{87}\text{Sr}/^{86}\text{Sr}$ - $\delta^{18}\text{O}$ correlations and decreases in both Sr- and O- isotopes with increasing $\text{SiO}_2$	1. Assimilation Equilibrium Crystallization (AEC) occurring within a deep chamber. The higher temperatures of mafic melt and lack of crystallization enabled mafic melt to assimilate more crustal material driving Sr- and O- isotopes up in mafic magma.	1. Model does not account for observation 2
Santo and Peccerillo (2008)	2. Positive $^{87}\text{Sr}/^{86}\text{Sr}$ - $\delta^{18}\text{O}$ correlations and increases in both Sr- and O- isotopes with increasing $\text{SiO}_2$	2. AFC processes occurring within shallow reservoirs, separately in time and/or space. Overwhelming negative $^{87}\text{Sr}/^{86}\text{Sr}$ - $\delta^{18}\text{O}$ correlations from the deep chamber acted to mask any large positive $^{87}\text{Sr}/^{86}\text{Sr}$ - $\delta^{18}\text{O}$ correlations.	2. Model attempts to account for all observations

Combining the two hypotheses, Santo *et al.* (2004) proposed a model that involved complex, multistage, polybaric evolution. Within a deep, higher-pressure chamber, plagioclase growth was suppressed and high-pressure cpx formed. Subsequently, isotopically distinct magmas (low  $^{87}\text{Sr}/^{86}\text{Sr}$ ) from isotopically distinct mantle sources were emplaced into separate shallow magma reservoirs where they experienced similar AFC processes. During the third eruptive cycle, modification of the magmatic plumbing system occurred via a shift in the tectonic stress regime that allowed batches of more radiogenic-Sr isotope magmas to be erupted simultaneously with lower-Sr isotope ratio magmas from the shallower chambers (Santo *et al.*, 2004).

A third research group, Santo and Peccerillo (2008), used oxygen isotope variations from phenocrystic clinopyroxene to investigate the mechanisms by which magmas evolved in Filicudi's magma plumbing system. Oxygen isotope signatures may provide insight into crustal contamination because, in contrast to Sr isotopes, they can be very sensitive indicators of crustal involvement (Santo & Peccerillo, 2008). For example, shallow AFC processes produce positive  $^{87}\text{Sr}/^{86}\text{Sr} - \delta^{18}\text{O}$  correlations because of the incorporation of bulk crust.

Results from Santo and Peccerillo (2008) documented an abundance of negative  $^{87}\text{Sr}/^{86}\text{Sr} - \delta^{18}\text{O}$  correlations and decreases in both Sr- and O-isotopes ratios with increasing silica content. They also documented a few single vents displaying positive  $^{87}\text{Sr}/^{86}\text{Sr} - \delta^{18}\text{O}$  correlations and increases in both Sr- and O- isotope ratios with increasing silica content.

Santo and Peccerillo (2008) argue because the positive correlations of  $^{87}\text{Sr}/^{86}\text{Sr} - \delta^{18}\text{O}$  and increases in both Sr- and O- isotope ratios with increasing silica content are

generally interpreted to be indicative of AFC processes, the observed abundance of negative  $^{87}\text{Sr}/^{86}\text{Sr}-\delta^{18}\text{O}$  correlations and decrease in both Sr-and O-isotopes ratios with increasing silica contents, can be attributed to the Assimilation Equilibrium Crystallization (AEC) processes. Unlike AFC, during AEC, no crystal fractionation takes place. Instead, hotter, mafic magma MELTS larger quantities of crustal wall rock, forcing both Sr-and O- isotopic ratios to higher values within the Si-poor magmas than those observed in the more Si-rich magmas (Santo & Peccerillo, 2008).

Integration of results allowed Santo and Peccerillo (2008) to propose a magma chamber structure. The few positive correlations observed between Sr- and O- isotopes developed from similar AFC processes occurring within separate shallow magma chambers. However, these AFC processes were subordinate to AEC processes occurring within a deep chamber (Santo & Peccerillo, 2008). The higher degree of crustal contamination by the mafic MELTS acted to offset any AFC signatures that accumulated within the shallow chambers.

### Crystal Growth Stratigraphy (CGS)

The significance that RAFC processes have on a magmatic system can be determined through textural, elemental and isotopic zoning patterns within individual volcanic crystals (Davidson *et al.*, 2007a, Ginibre *et al.*, 2007, Humphreys *et al.*, 2006, Streck, 2008, Tsuchiyama, 1985, Viccaro, 2010). Minerals record thermodynamic changes in their textural and compositional zoning patterns (Ginibre *et al.*, 2007). Because of this, the core to rim growth zones in minerals typically represent a

chronological sequence from old to young in the evolution of the magma from which the mineral crystallized. *In situ* textural investigations of phenocrysts can document the relative timing of RAFC events, while *in situ* compositional variations in  $^{87}\text{Sr}/^{86}\text{Sr}$  can document magma mixing and contamination processes (Ramos & Tepley, 2008).

Plagioclase, a mineral stable within many magmas from basalt to rhyolite, keeps a record chemically from core to rim of the conditions under which it grew (Humphreys *et al.*, 2006). Plagioclase is the most widely used mineral in CGS studies for several reasons. First, it is typically one of the first minerals to come on the liquidus, ensuring its core to rim growth records as much of the magmatic history as possible. Secondly, diffusive exchange between Ca and Na ions in the two end-members (Anorthite (An) - Ca rich and Albite (Ab) - Na rich) of plagioclase is relatively slow. Thus, dissolution surfaces and other textural changes are preserved in response to changes in magma temperatures, pressures, compositions, and water contents (Davidson *et al.*, 2007a). Lastly, the mineral typically contains sufficient concentrations of Sr to allow for viable *in situ* Sr isotopic geochemical work (Davidson *et al.*, 2007a).

#### *Plagioclase Textural Zoning*

Textural and relative compositional zoning data on plagioclase crystals can be determined by using Nomarski Differential Interference Contrast (NDIC), a reflected light technique used to image textures, and Back-Scattered Electron (BSE) images, obtained using an electron microprobe to provide compositional data on plagioclase growth zones.

Normal zoning is the expression of compositional variability as the crystal and melt follow a liquid line of descent. For plagioclase, normal zoning compositions range from calcic to sodic (Ginibre *et al.*, 2007). Reverse zoning indicates a compositional inversion within the crystal growth stratigraphy and often indicates a recharge event has occurred (Ginibre *et al.*, 2007).

Oscillatory zoning in plagioclase is the repetitive occurrence of Na-rich and Ca-rich compositional bands or growth zones. On a small spatial scale (5-10  $\mu\text{m}$ ) oscillations (< 10 mol% compositional change) have been interpreted to be from closed system changes (i.e., kinetic effects), while on a larger spatial scale (20-30 $\mu\text{m}$ ) oscillations (> 10 mol% compositional change) have been interpreted to occur from open system changes such as recharge and/or assimilation (Ginibre *et al.*, 2007, Humphreys *et al.*, 2006).

Monotonous/unzoned or textureless plagioclase indicates there were few changes in the melt composition from which the mineral was growing. Plagioclase that grows very quickly, and does not have sufficient time for the surrounding melt to compositionally or kinetically change, will display monotonous zoning (Streck, 2008). This can be seen in plagioclase microlites that remain unzoned because of their fast growth directly prior to an eruption. Likewise, plagioclase crystals can preserve their monotonous textures if they have a high anorthite (Ca end-member) content. Moreover, experimental studies have shown that when high anorthite plagioclase crystals are introduced into a more albitic (Na-end member) melt, the interface between the crystal and melt is smooth, and reflects little to no dissolution or textural changes (Tsuchiyama, 1985).



A sieved or mantled texture documented in plagioclase is a reaction between a Na-rich plagioclase and a Ca-rich melt (Humphreys *et al.*, 2006). Partial dissolution at the interface between a sodic-rich core and calcic-rich melt causes complex oscillatory zoning or resorption around the rim and a sieve-like or holey-texture to form within preexisting plagioclase cores. The hotter calcic-rich melt is typically introduced into the shallow crust via recharge processes and is then mixed with the more sodic-rich melt (Tsuchiyama, 1985).

Patchy texture refers to corrosion or sieving in plagioclase cores that was subsequently filled with melt (glass) and/or new mineral (plagioclase) (Streck, 2008). A patchy or irregularly distributed zoning pattern can be found in plagioclase that initially grew under high water pressures and then experienced partial resorption in response to magma ascent and associated decreases in temperature and  $p\text{H}_2\text{O}$  (Humphreys *et al.*, 2006, Streck, 2008).

#### *Elemental Zoning in Plagioclase*

Although imaging techniques allow for relative compositional changes to be documented, quantitative compositional changes within the plagioclase growth zones require additional analysis. The electron microprobe can document compositional variations in crystals from core to rim, and the most typical compositional parameter assessed in plagioclase is the molar % anorthite content (An) ( $\text{Ca}/(\text{Ca}+\text{Na})\cdot 100$ ) (Davidson *et al.*, 2007b). Changes in An content in a plagioclase crystal can correspond to changes in magma composition; an increase in An content can indicate a shift towards more mafic magmas, whereas a decrease can correspond to a shift toward more felsic

composition. This, however, is not always the case as other parameters such as changing water content, pressure etc., can also act to change An contents (Davidson *et al.*, 2007b). For example, the appearance of large (>0.1 mm) high-Ca plagioclase crystals in a andesite is somewhat uncommon, but can occur if H<sub>2</sub>O acts to suppress plagioclase crystallization until after the appearance of Fe-Mg silicates (Sisson & Grove, 1993). The plagioclase that crystallizes is Ca-rich, and its removal (i.e., fractionation) acts to increase the silica and alkali contents in the residual liquid (Sisson & Grove, 1993).

Ginibre *et al.* (2002) have linked the scale of elemental changes to kinetic influences versus melt compositional changes. High amplitude/low frequency (HALF) An changes (> 10 mol % over a spatial scale of 20-30  $\mu\text{m}$  or across a textural boundary) have been experimentally determined to be caused by recharge or assimilation within a system (Ginibre *et al.*, 2002). Likewise high frequency/low amplitude (HFLA) An changes (+/- 10 mol % over a spatial scale of 5-10  $\mu\text{m}$  or across a textural boundary) indicate kinetic effects that can be associated with decompression, degassing, and convection within a magma system (Ginibre *et al.*, 2002).

Trace element compositions obtained from elemental zoning investigations can be related to the melt composition by partition coefficients (Ginibre *et al.*, 2007). Just as the frequency and amplitude of the An content within different growth zones allow documentation of processes that affected crystal growth, changes in trace elements allow for identification of RAFC processes or kinetic effects. An increase in An content without an associated trace element change likely indicates kinetic closed system changes occurred within the system, whereas an increase in An content with associated changes in

trace elements such as Mg, Sr, and Fe indicate recharge or assimilation may have occurred (Ginibre *et al.*, 2002). The bulk compositional change that occurs to host magma undergoing assimilation or recharge has a stronger impact on partitioning of trace elements in plagioclase than the compositional dependence of partition coefficients (Ginibre *et al.*, 2007).

#### *Sr Isotopic Zoning in Plagioclase*

Investigating *in situ* variations in isotopic composition across a set of crystal dissolution surfaces can provide a history of magma system evolution (Davidson *et al.*, 2007a). Isotopic variations among crystals indicate that they have crystallized from magmas with distinct isotope characteristics (Davidson *et al.*, 2007a). Changes in the isotopic composition of a magma could be due to mixing with another magma of a different isotopic composition (recharge) and/or to crustal contamination (assimilation) (Davidson *et al.*, 2007a). Therefore, as the magma changes composition, the minerals crystallizing at that time record the new isotopic input within each textural zone and effectively record a snapshot of the magma system during growth (Davidson *et al.*, 2007a).

During fractional crystallization, strontium isotopes are not differentially incorporated into growing minerals, and thus plagioclase and the magma from which it grew share the same  $^{87}\text{Sr}/^{86}\text{Sr}$  signature. When *in situ* differences in  $^{87}\text{Sr}/^{86}\text{Sr}$  within plagioclase crystals are documented, the indication is that a distinct magma was introduced into the system and the new signature is recorded in a particular growth zone. Thus, an increase in the  $^{87}\text{Sr}/^{86}\text{Sr}$  ratio most likely indicates assimilation of magma

characterized by more radiogenic Sr occurred, and a decrease most likely indicates recharge of a less radiogenic magma occurred.

### Quantitative Modeling

Documenting the major element evolution and associated quantitative changes in physical properties within a magmatic system can be done using the MELTS thermodynamic model (Ghiorso, 1997, Ghiorso & Sack, 1995). The quantitative modeling program uses input parameters such as parental magma composition, water content,  $fO_2$ , pressure, and temperature, and combines them with thermodynamic properties to predict mass and major element compositions of minerals and MELTS. MELTS results document changes in mineral assemblages, An contents of plagioclase, and masses of solid crystals and melt, as they occur in a series of steps in temperature and pressure (for polybaric runs) along the liquid line of descent. Best-fit models allow for documentation of the depth, temperature, and water content of magmatic systems including key information about the temperature at which different minerals came onto the liquidus.

## CHAPTER III

### METHODS

#### Whole Rock Analysis

Nineteen representative volcanic rock samples from Filicudi Island were collected by a field party that included Drs. Wendy Bohrson and Jeff Lee, Rachel Hunt, Aaron Mayfield, Brad Pitcher and Michelle Miller (CWU), Jeff Creamer (UCSB) and Angela Doherty (University of Naples) during a field season in 2010. Sample locations were chosen based on descriptions by Santo (2000) and the map of Tranne *et al.* (2000). Two fresh, fist-size samples were collected from each outcrop. The first was collected to make billets for thick and thin sections, while the second was broken in the field (to minimize contamination acquired by processing in a laboratory) into chips to be used for geochemical analysis.

Whole rock x-ray fluorescence (XRF) and inductively coupled plasma-mass spectrometry (ICPMS) analyses were performed at Washington State University's GeoAnalytical Lab in order to obtain major and trace element concentrations. Whole rock strontium, and neodymium isotopic analyses were performed at New Mexico State University by Thermal Ionization Mass Spectrometry (TIMS).

#### *X-Ray Fluorescence (XRF)*

Major and select trace elements were collected via XRF analysis at Washington State University. Sample preparation and analysis were similar to that described by Johnson *et al.* (1999). Approximately 28 grams from each sample were ground into a

powder in a swing mill with tungsten carbide surfaces for two minutes. Three and a half grams of each powder were weighed and mixed for ten minutes in a plastic jar with 7.0 grams of spec pure dilithium tetraborate ( $\text{Li}_2\text{B}_4\text{O}_7$ ). All 19 powders were then placed into individual graphite crucibles, placed on a silica tray, and loaded into a muffle furnace for 5 minutes until glass bead fusion took place. Once the beads cooled, they were reground in the swingmill for 35 seconds and then were refused in the graphite crucibles for 5 minutes. Resulting beads were polished and washed in an ultrasonic cleaner. After beads were thoroughly cleaned, they were loaded into the Thermo-ARL Advant'XP+ WDXRF spectrometer for elemental analysis.

The XRF ran using a Rhodium target at 60 kV and 60 mA with full vacuum and a 29 mm mask for all elements and samples (Johnson *et al.*, 1999). The concentrations of 29 elements were measured by comparing x-ray intensities for each element with the intensities of 106 known standards used to calibrate the instrument approximately every 10 months. In order to maximize and track single run precision, two internal standards (BCR-C and GSP-2) and two pure vein-quartz blanks, as well as a duplicate bead (10-2R) were loaded along with samples. Precision for measurements of elements at  $2\sigma$  was: major elements  $\leq 1.0\%$  except for MnO, MgO, and  $\text{Na}_2\text{O}$  which are  $\leq 1.5\%$ ; Nb, Cr, Sc, V, and Ni  $\leq 8\%$ ; Ba, Rb, Sr and Zr  $\leq 2.5\%$ ; abundances  $\leq 10$  ppm are qualitative only.

#### *Inductively Coupled Plasma Mass Spectrometry (ICPMS)*

Whole rock trace element analysis was also completed at Washington State University using ICPMS technology, known for its greater detection capabilities of rare earth elements (REEs) (Johnson *et al.*, 1999). Sample preparation for ICPMS samples

was similar to that of the XRF samples and occurred at the same time. Once samples were powdered, ~ 2 grams of powder were mixed with 2 grams of spec pure dilithium tetraborate ( $\text{Li}_2\text{B}_4\text{O}_7$ ). Samples were then placed into individual graphite crucibles, placed on a silica tray, and loaded into a muffle furnace for 30 minutes. After cooling, the bead was reground and 250 mg were weighed and placed into a Teflon container for several steps of progressive acid dissolution. The first dissolution step consisted of using 2 ml of  $\text{HNO}_3$ , 6 ml of HF, and 2 ml  $\text{HClO}_4$ . Following dissolution, samples were evaporated on a hot plate. Once dry, the sides of the Teflon vial were rinsed with a small amount of DI water. The second dissolution required the addition of 2 ml of  $\text{HClO}_4$ , followed by a second round of hot plate evaporation. The third dissolution required the addition of 10 ml of DI water, 3 ml of  $\text{HNO}_3$ , 8 drops  $\text{H}_2\text{O}_2$ , and 3 drops of HF. The samples were then warmed on a hot plate until a clear solution was produced. DI water was then added until the entire sample weighed 60 grams.

Fourteen samples at a time were loaded into the Agilent model 7700 ICPMS where they were further diluted an additional 10X at the time of analysis using Agilent's Integrated Sample Introduction System (ISIS) (Knaack *et al.*, 1994). Three USGS rock standards were also loaded to document instrumental accuracy. A duplicate sample (10-2R) was used to document instrumental precision. Instrumental drift was corrected using Ru, In, and Re as internal standards, while oxide inferences were corrected using two mixed-element solutions with elements added to quantity specific oxide, isobaric, and doubly charged interferences. (Knaack *et al.*, 1994). Precision for the method at  $2\sigma$  was:  $\leq 2.5\%$  except for Th, U, and Pb, which were  $\leq 4.5\%$ . Long term precision of  $\leq 3\%$  is

achieved using this method, and accuracy relative to several accepted rock powder standards is less than 10% for elements analyzed at levels greater than 1/10<sup>th</sup> chondrite (Knaack *et al.*, 1994, Boroughs *et al.*, 2010 – personal communication).

### *Thermal Ionization Mass Spectrometry (TIMS)*

Whole rock strontium and neodymium isotope analyses were conducted using column chemistry in a class 1000 clean lab and analyzed using a VG Sector 54-30 thermal ionization mass spectrometer at New Mexico State University. Approximately 0.1 gram of each of the 19 whole rock powers, made using the swing mill at WSU, were placed in a 15 ml Teflon beaker. Samples were dissolved using 3 ml of concentrated HNO<sub>3</sub> and 3 ml of concentrated HF. Beakers were then capped and left overnight on a hotplate to allow for complete digestion. Samples were then evaporated and 5-6 ml of 7N HNO<sub>3</sub> were added, Teflon beakers were capped and left overnight on a hot plate. A last round of dissolution and evaporation used 5-6 ml of 6N HCl. Once evaporated, 1 ml of 2.5N HCl was added, and solutions were placed into 2 ml Teflon tubes and centrifuged for 3 minutes. Cation exchange column chemistry was then used to purify strontium, and concentrate REEs.

Quartz columns filled with cation exchange resin were pretreated with 10 ml of 2.5N HCl. Teflon beakers (15ml) were then placed below columns to collect all remaining washes. One half a ml of centrifuged samples was loaded onto the column. Loading was followed by two washes of 0.5 ml 2.5N HCl, a 9.5 ml 2.5N HCl wash, and a 5 ml 2.5N HCl wash. Clean 7 ml Teflon beakers were then placed under the cation



columns and 6 ml of 2.5 N HCl was added to collect purified Sr. Following successful collection of Sr, a second group of clean beakers was placed under the cation columns and 10 ml of 6N HCl was added to collect REEs. Beakers were placed on a hotplate to evaporate acid, and cation exchange columns were cleaned using 6N HCl.

REE columns were pretreated with 10 ml of 0.25N HCl. REE samples were dissolved in 0.5 ml of 0.25N HCl. Samples were then loaded onto the columns. Following loading, columns were washed twice with 0.5 ml 0.25N HCl, followed by 1 ml and 4 ml 0.25N HCl washes. Neodymium was collected in clean Teflon beakers using 6 ml of 0.25N HCl. Beakers containing purified Nd solutions were removed and dried on a hot plate.

Samples were then dissolved with 1-2  $\mu\text{L}$  of 5%  $\text{HNO}_3$ , and loaded on to filaments. For neodymium analyses, a triple assembly with Rhenium filaments was used. The sample was loaded onto one side only. The side filament volatilized the sample while the center filament ionized the sample. For strontium analyses, a single Rhenium filament was used, and samples were loaded with tantalum oxide and phosphoric acid. Ten loaded filaments, nine samples and one standard (JNdI-1 Nd or NBS 987 Sr), were then placed in a turret and loaded into the source of the mass spectrometer, and the source was pumped down. Standards had typical uncertainties of  $\pm 0.00001$  for both Nd and Sr isotope ratios, and all data were then compiled by a computer. Sr/Nd isotope analysis used 5 collections in dynamic mode with Sr normalizing to  $^{87}\text{Sr}/^{86}\text{Sr} = 0.1194$  and Nd normalizing to  $^{146}\text{Nd}/^{144}\text{Nd} = 0.7219$ .

There is no LA-ICPMS protocol for measuring  $^{87}\text{Sr}/^{86}\text{Sr}$  in groundmass, so each sample's groundmass collected using a microdrill, and analyzed with the TIMS at New Mexico State University. Samples of groundmass for each of the seven thick sections (discussed below) were obtained using a the semi-automated New Wave Microdrill at Washington State University. Operating parameters for the drill were set to complete three passes of 600  $\mu\text{m}$  length at 15  $\mu\text{m}$  depth per pass. Samples were collected using 1-2 drops of DI water and a pipet tip, and were placed into 7 ml Teflon beakers. Column microchemistry and thermal ion mass spectrometry were then completed on one groundmass sample from each thick section at New Mexico State University. Methods for column chemistry and TIMS analysis are fundamentally the same as those described for obtaining whole rock isotopes.

#### *In situ* Plagioclase Textural and Compositional Analysis

The seven least-altered samples that represent the range of magma compositions on Filicudi Island were chosen for thick ( $\sim 100\ \mu\text{m}$ ) and thin ( $\sim 30\ \mu\text{m}$ ) section preparation. Plagioclase textural data documented five textural types obtained using Nomarski and Back Scattered Electron (BSE) techniques on thick sections. Plagioclase crystals representing each of five identified textures were chosen for detailed core to rim traverses using Electron Microprobe Analysis (EMPA) at Washington State University to document changes in major and trace elements, especially anorthite and FeO contents. Trace element analysis was performed on selected plagioclase crystals at Oregon State University using a laser-ablation inductively coupled plasma mass spectrometer (LA-

ICP-MS) in order to gain core to rim trace elements, specifically Sr, Mg, Ba, La, and Ti, concentrations. Sr isotopic analyses were then collected at Washington State University's GeoAnalytical Lab by laser ablation using a multiple-collector inductively coupled plasma mass spectrometer (LA-MC-ICPMS) in order to document changes in strontium isotopes between core and rim.

#### *Nomarski Differential Interference Contrast Microscopy*

Plagioclase crystals from the seven 100  $\mu\text{m}$  thick sections were imaged and classified into one of five textural groups using Nomarski Differential Interference Contrast Microscopy (NDIC). NDIC is a beam splitting, reflected light technique used to enhance the contrast between fine-scale textural features of individual crystals (Lang, 1969). Polished thick sections were first etched using fluoroboric acid ( $\text{HBF}_4$ ) for 20-22 seconds. The acid preferentially dissolves Ca-rich zones of the plagioclase crystals, leaving micro-topographic relief of Na-highs and Ca-lows. NDIC images were obtained using a Nomarski filter under reflected light from a petrographic microscope fitted with a Nomarski prism and digital camera at Central Washington University. Approximately 40 plagioclase crystals per sample were photographed to document a wide range of textures and to guide choice of electron microprobe analysis locations.

#### *Electron Microprobe Analysis (EMPA)*

Major and selected trace element data (e.g., Fe) were collected from core to rim of plagioclase crystals using a JEOL 8500F Field Emission electron microprobe at

Washington State University under the direction of Dr. Michael Rowe. The probe was set to have an accelerating potential of 15 kV, a beam current of 30 nA, and a 4  $\mu\text{m}$  diameter spot size. Etched thick sections were carbon coated prior to EMPA. Approximately ~30 plagioclase crystals were chosen from each of the seven thick section samples using a classification system that combined textures and sizes. Roughly three crystals for each of the five recognized textures types and each of the three different sizes, large (<2mm), medium (~1-2mm), and small (~1-0.5 mm), were probed. Two or three microlites (<0.5 mm) were also probed from core to rim. Backscatter Electron (BSE) images were taken of each crystal prior to collection of elemental data. Exact analysis locations were selected using both BSE and Nomarski images and were based on locations of textural boundaries. A known standard Labradorite was also analyzed in between every ~30 points to ensure instrumental precision. Resolution for the probe is 4-microns and quantitative uncertainty is typically 1-2% relative. Detection limits for given elements are generally better than 0.02 wt. % and be found in Electronic Appendix A.

#### *Laser Ablation Inductively Coupled Plasma Mass Spectrometer (LA-ICPMS)*

##### *Trace Elements*

Trace elements from core to rim of select plagioclase crystals were analyzed using a Thermo Xseries2 quadrupole inductively coupled mass spectrometer at the W.M. Keck Collaboratory for Plasma Spectrometry at Oregon State University (OSU), under the direction of Dr. Andy Ungerer and Dr. Adam Kent. Approximately 10-15 plagioclase crystals per sample were chosen based on crystal sizes and changes in anorthite content

obtained from EMPA. Sample preparation included removing the carbon coat applied for EMPA. Operating conditions were set at a 7 Hz pulse rate, and a 30  $\mu\text{m}$  circular spot size. The laser energy was set to 4.8  $\text{J}/\text{cm}^2$  that used 70% attenuation of a 5 mJ beam. Instrument calibration used GSE-1G and GSD-1G as well as basalt glasses BHVO-2G and BCR-2G as secondary standards. Spot locations were chosen based on textural boundaries seen on Nomarski images, relative core and rim locations, and areas of large (>10 mol %) Anorthite changes. Ablated material was mixed with argon gas at a 0.8 L/min flow rate, and was aspirated into a tiny radio frequency generator, where plasma was created. The quadrupole then separated the elements based on charge and mass ratio, and the ions were detected using a collector. The collector fed to an onboard computer where data were reduced, processed and output into an Excel sheet. The Excel output was then further processed using OSU in-house scripts called LaserTram and LaserCalc, which run in Visual Basic within Excel. Processed data can be found in Electronic Appendix B and complete core to rim profiles of major and trace elements can be found in Electronic Appendix C.

### *Radiogenic Isotopes*

*In situ* strontium isotope analysis of cores and rims from plagioclase crystals were collected at Washington State University's GeoAnalytical Lab using a ThermoFinnigan Neptune laser ablation multiple-collector inductively coupled plasma mass spectrometer (LA-MC-ICPMS). Plagioclase crystals chosen for analysis were the same as those chosen for trace element analysis. However, unlike LA-ICPMS trace element analyses, the laser

to collect Sr isotopes rasters back and forth in a single trench, resulting in substantially deeper trough and larger ablation area. Troughs typically were 600  $\mu\text{m}$  long, and 60  $\mu\text{m}$  wide, so locations were chosen based on available area. Where possible, core, intermediate region, and rim analyses were completed. Locations were chosen to minimize exposure to inclusions that might cause Rb spikes. Two to three smaller phenocrysts of sufficient size ( $> 600 \mu\text{m}$ ) were also ablated.

Operating parameters were set to make three ablation passes with each pass having a scan speed of 11-  $\mu\text{m}$  per second allowing an overall trough depth of 70 to 130  $\mu\text{m}$ . Sr isotope values were derived from 30 ratios measured in 8-second integrations. The instrument was calibrated by analyzing a known plagioclase standard (SRP) five to six times, before and after each thick section. An in-house data reduction program accounted for interferences with elements such as Rb,  $\text{Yb}^{2+}$ , and  $\text{Er}^{2+}$  (Ramos *et al.*, 2004). Interference corrected Sr isotope ratios were then recalculated using a correction factor obtained by taking the average value obtained from the standard runs, divided by the accepted value of the standard. Typical results for  $^{87}\text{Sr}/^{86}\text{Sr}$  yield a reproducibility of  $<0.00005$ . Raw *in situ* Sr isotope data can be found in Electronic Appendix D and complete core to rim profiles of major element and Sr isotope analysis can be found in Electronic appendix E.

### MELTS Modeling

Quantitative models were generated using the thermodynamic phase equilibria program MELTS (Ghiorso & Sack, 1995) to document the major element evolution and associated changes in physical properties within the Filicudi Island magma system along

the liquid line of descent. A sample from Santo *et al.* (2004) was chosen and input as the most primitive composition (MgO wt. % of 10.34). Liquidus temperatures were specified by MELTS based on input from the sample. Fifteen separate models were run, each varying initial and final pressure (4 kb-20 bar), temperature (1500° C-1000° C), and water content (5-3 wt. %) in order to obtain the conditions that best fit whole rock major element data from all nineteen samples on Filicudi Island. Oxygen fugacity was initially set to the HM buffer and then allowed to self-buffer during the run. Initial parameters for the 15 runs were based off of ~300+ models run on the neighboring island of Salina, which shares similarities in whole rock major and trace element trends (A. Mayfield, pers. communication, 2012) (Figure 3-7).

## CHAPTER IV

### RESULTS

#### Overview

Nineteen whole rock samples were analyzed for major and trace elements and Sr and Nd isotopes, and seven samples were chosen for *in situ* plagioclase analysis that included NDIC imaging, EMP major and trace element and LA-ICPMS trace element and Sr isotope analysis. Whole rock data are presented as a package and compared to the neighboring islands of Salina and Alicudi. For each *in situ* technique, results of seven samples chosen for thick and thin section analysis will be presented in order based on Groups developed using the relative stratigraphy of Tranne *et al.* (2000) (Table 1).

#### Whole Rock Major and Trace Element Data

Whole rock samples for Filicudi Island span a compositional range from basalt to andesite (50.93-62.87 wt. % SiO<sub>2</sub>) with two samples straddling the boundary between andesite and trachyandesite (Figure 3). As SiO<sub>2</sub> increases, MgO, FeO, CaO, Al<sub>2</sub>O<sub>3</sub>, and TiO<sub>2</sub> generally decrease, whereas K<sub>2</sub>O and Na<sub>2</sub>O increase (Table 3, Figure 4). P<sub>2</sub>O<sub>5</sub> abundances are similar among most samples with one exception (sample FIL 10-8).

Compatible trace elements Ni and Sc decrease as SiO<sub>2</sub> increases, whereas Cr abundances vary among samples (Figure 5). Sample FIL 10-22 has 38 ppm Cr, which is much higher than all other samples. The remaining samples plot as two arrays between 50.93 and 62.8 SiO<sub>2</sub>. A systematic trend between SiO<sub>2</sub> and Sr is lacking, although in general the trend from more mafic to more silicic samples is negative, and samples with



similar  $\text{SiO}_2$  have a range of Sr concentrations that varies by up to 100 ppm. One sample, Fil 10-11, is clearly the exception as it has 714 ppm of Sr and 62.9 wt. %  $\text{SiO}_2$ .

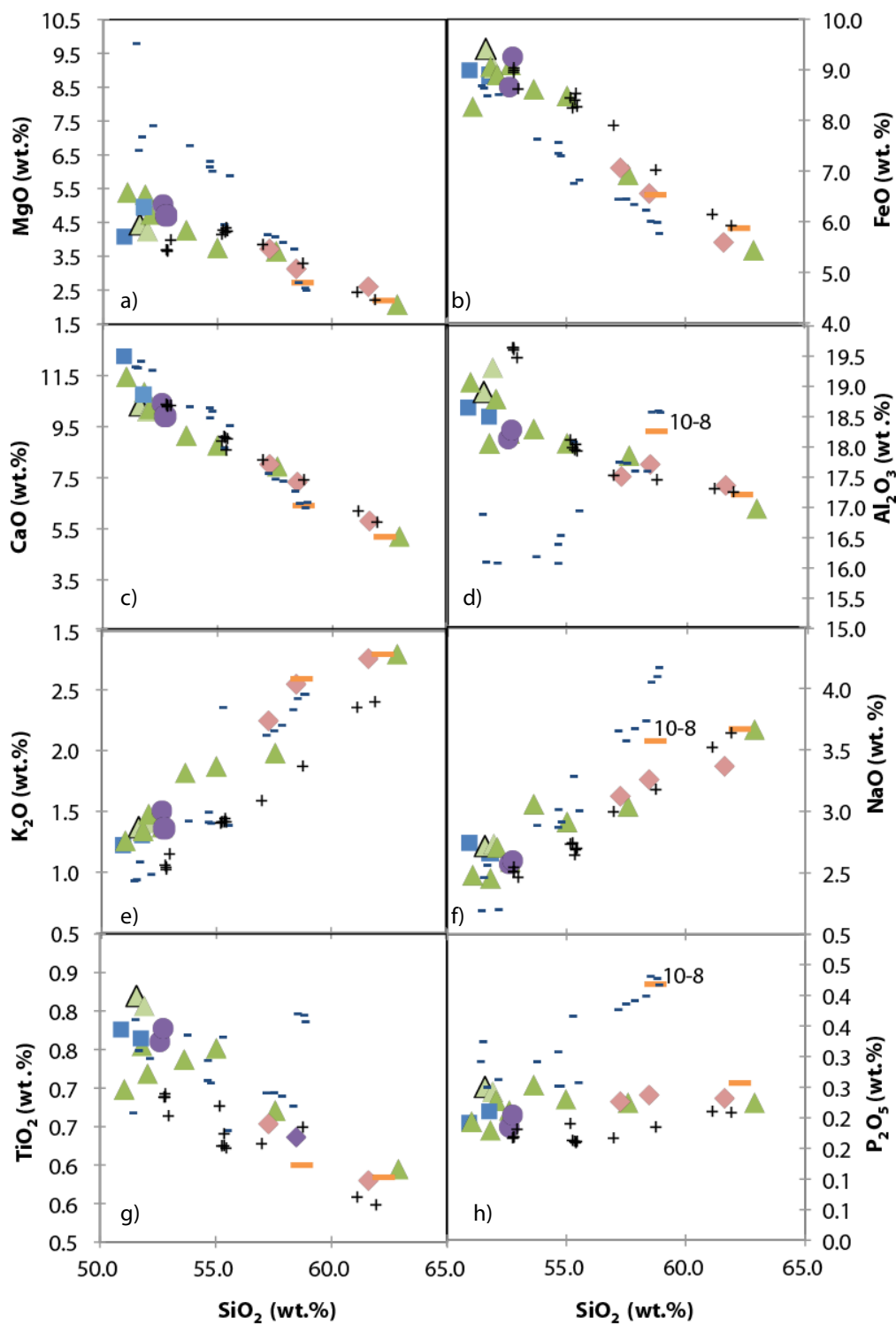
Typical incompatible trace elements Rb, Ba, Th, and U all show trends that increase with increasing  $\text{SiO}_2$  content (Figure 6). Zr and Nb also increase as  $\text{SiO}_2$  increases with the exception of sample Fil 10-8 that shows a higher value of Zr at 138 ppm and a higher value of Nb at 59 ppm compared to other samples with similar  $\text{SiO}_2$ .

The Rare Earth Element (REE) La increases with increasing  $\text{SiO}_2$  contents, with the exception again of one sample, Fil 10-8 that has a much higher value at 43 ppm (Figure 7). La, Nd, Eu and Lu all show increasing abundances with increasing  $\text{SiO}_2$ , albeit with scatter, until the basaltic andesite compositions (~52-56  $\text{SiO}_2$  wt. %) when both increases and decreases are seen, followed by a return to a general increase in the most evolved rocks. For all elements, sample Fil 10-8 has the highest concentrations of these elements.

Typically basalts are the least enriched in REE, whereas andesites are more enriched (Figure 8). The exception is sample Fil 10-8, which has the highest concentration of REE but is not the most silicic (58.72 wt.%  $\text{SiO}_2$ ). Similarly, La/Yb values for the samples range from 9.12 to 16.8, with sample 10-8 being the highest (Table 3, Figure 8). Neither negative nor positive Eu anomalies are evident.

When compared to the nearby islands of Alicudi and Salina, Filicudi's whole rock major element trends fall between Salina's lower values and Alicudi's higher values, with the exception of  $\text{Al}_2\text{O}_3$ , which is lower on Alicudi and higher on Salina (Figure 4) (Salina data provided by Aaron Mayfield and Alicudi data provided by Rachel Hunt (R. Hunt

and A. Mayfield, pers. communication). Overall, Filicudi's trends mimic Salina's more closely with the exception of sample Fil 10-8. For some oxides (e.g.,  $\text{Al}_2\text{O}_3$ ,  $\text{Na}_2\text{O}$ , and  $\text{P}_2\text{O}_5$ ), this sample has abundances that are similar to the higher abundances of Alicudi (Figure 4). Filicudi's Sc abundances mimic those of both Salina and Alicudi, and Sr values for all islands share similar scattered ranges. Ni and Cr are similar between Filicudi and Salina; Alicudi's ranges are much higher and therefore not plotted on Figure 5 (a) and (c). Incompatible trace elements values for Filicudi fall in between Salina's lower values and Alicudi's higher values with the exception of Rb (Figure 6). Filicudi has the highest Rb values at similar  $\text{SiO}_2$  values. For most of the REE, values fall in between Salina's lower and Alicudi's higher values. The exceptions are Eu and Lu, which both show more scatter compared to Alicudi and Salina (Figure 7).



■ Group 1 ▲ Group 2 △ Group 2a ● Group 3 ◆ Group 4 — Group 5 - Alicudi + Salina  
 Figure 4: Whole rock  $\text{SiO}_2$  wt. % plotted against whole rock (a) MgO, (b) FeO (c) CaO, (d)  $\text{Al}_2\text{O}_3$ , (e)  $\text{K}_2\text{O}$ , (f) NaO, (g)  $\text{TiO}_2$ , and (h)  $\text{P}_2\text{O}_5$  wt. %. Symbols are the same as in Figure 3.

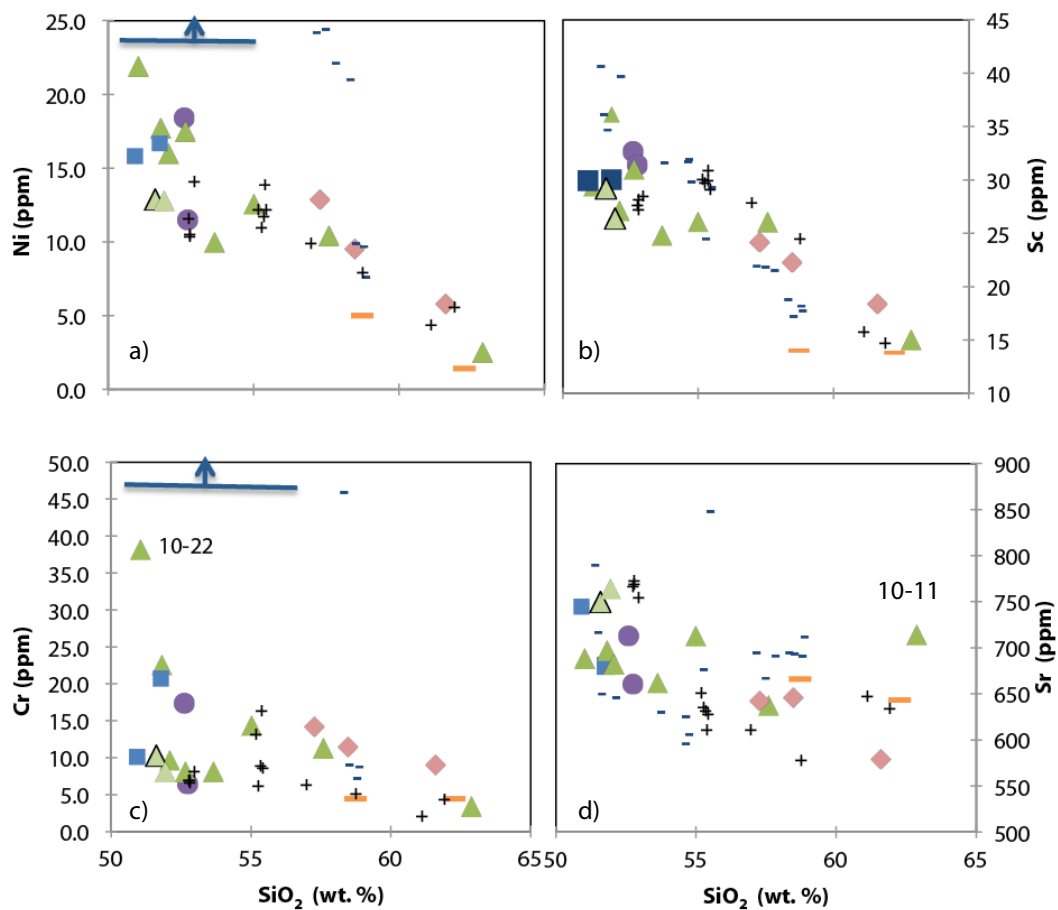


Figure 5: Whole rock  $\text{SiO}_2$  wt. % plotted against whole rock compatible trace elements (a) Ni, (b) Sc, (c) Cr, and (d) Sr ppm for Filicudi samples. Symbols are same as in Figure 3. Because Alicudi Ni and Cr ranges are much higher than both Filicudi and Salina, the symbols out of range are marked by a line and arrow.

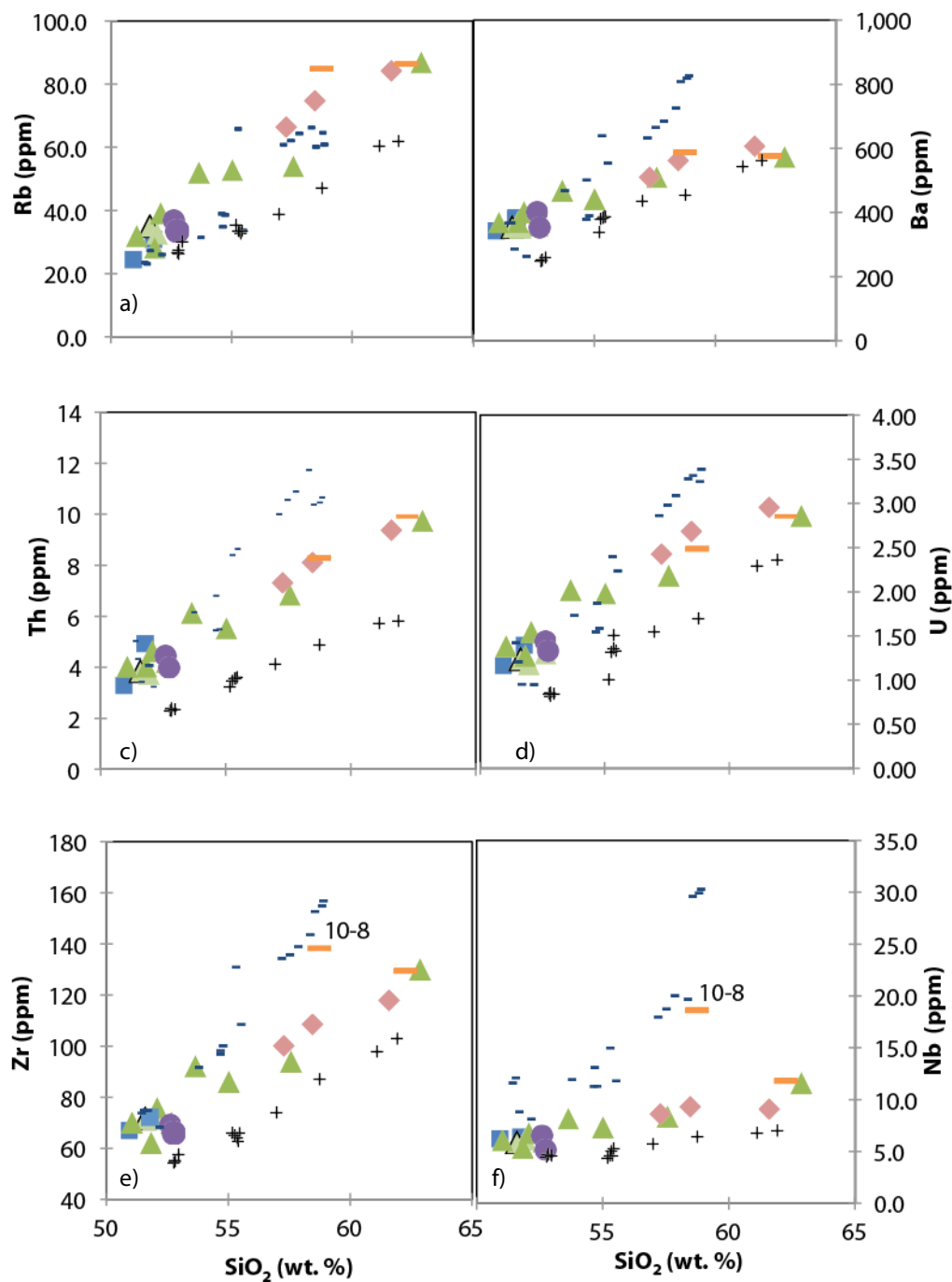


Figure 6: Whole rock  $\text{SiO}_2$  wt. % plotted against whole rock incompatible trace elements (a) Rb, (b) Ba, (c) Th, (d) U, (e) Zr, and (f) Nb ppm for Filicudi samples. Symbols are same as in Figure 3.

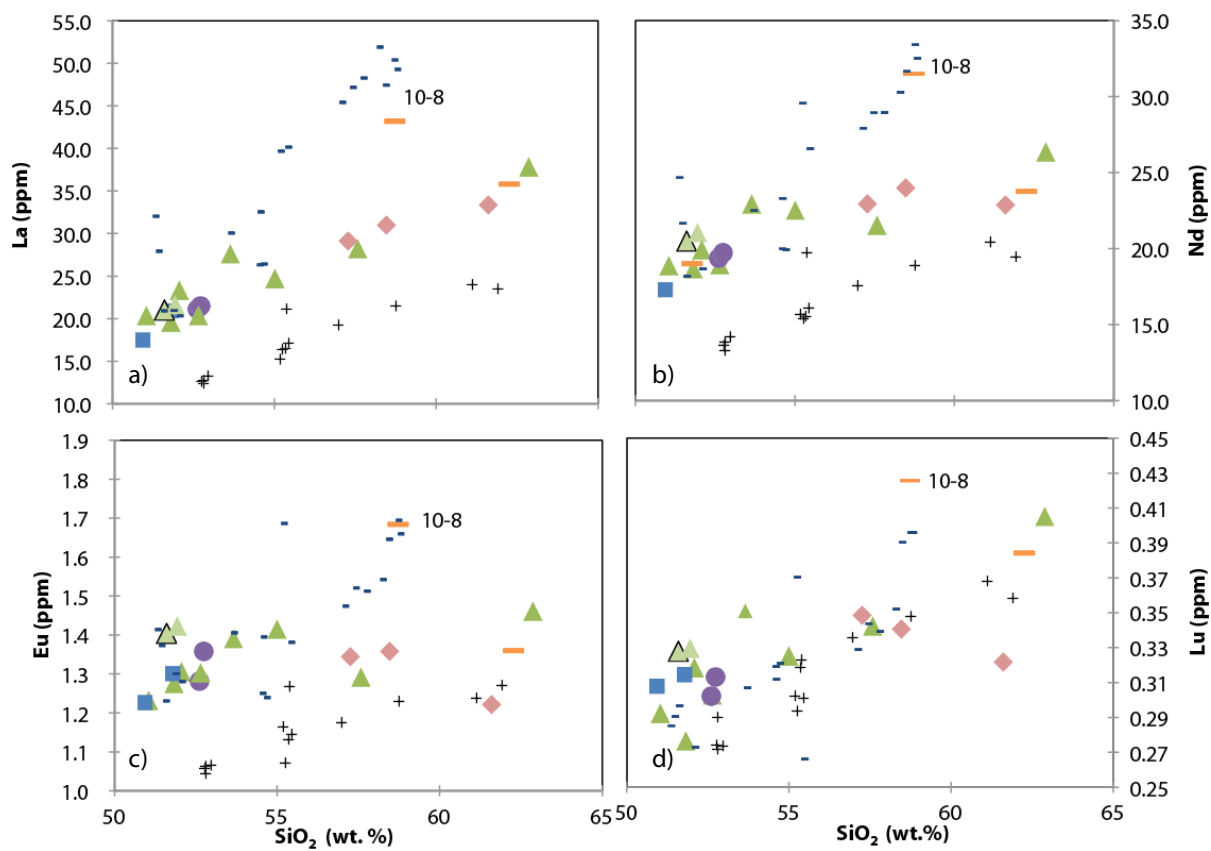


Figure 7: Whole rock  $\text{SiO}_2$  wt. % plotted against whole rock Rare Earth Elements (a) La, (b) Nd, (c) Eu, and (d) Lu ppm for Filicudi samples. Symbols are same as in Figure 3.

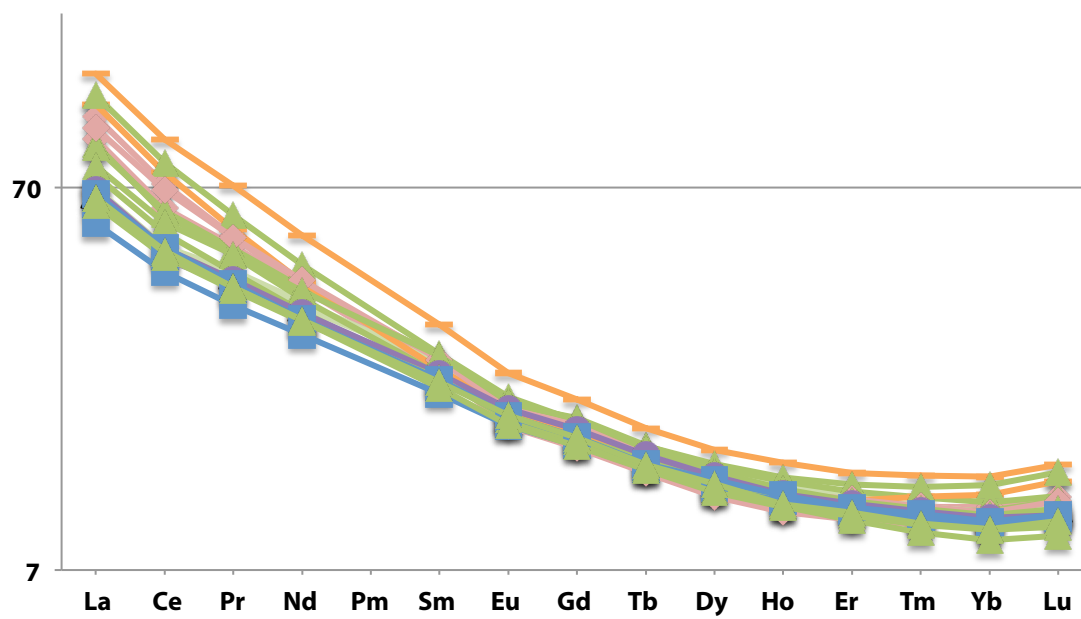


Figure 8: Chondrite-normalized REE diagrams for Filicudi Island. Normalization constants are from Boynton (1984). Symbols are the same as in Figure 3.

Table 3. Whole rock major and trace element data, calc-alkaline volcanic rocks from Filicudi Island, Italy.

Sample	10-16	10-21	10-22	10-20	10-13	10-23
Group	1	1	2	2	2	2
<b>SiO<sub>2</sub> (wt.%)</b>	50.93	51.78	51.04	51.81	52.07	52.64
<b>TiO<sub>2</sub></b>	0.78	0.76	0.70	0.75	0.72	0.74
<b>Al<sub>2</sub>O<sub>3</sub></b>	18.65	18.49	19.07	18.06	18.78	18.22
<b>FeO*</b>	8.98	8.89	8.27	9.06	8.90	9.09
<b>MnO</b>	0.16	0.18	0.16	0.16	0.16	0.17
<b>MgO</b>	4.08	4.96	5.38	5.32	4.74	4.80
<b>CaO</b>	12.27	10.76	11.44	10.86	10.21	10.17
<b>Na<sub>2</sub>O</b>	2.74	2.66	2.48	2.46	2.71	2.59
<b>K<sub>2</sub>O</b>	1.22	1.30	1.26	1.34	1.48	1.37
<b>P<sub>2</sub>O<sub>5</sub></b>	0.19	0.21	0.19	0.18	0.23	0.21
<b>Ni (ppm)</b>	16	17	22	18	16	16
<b>Cr</b>	10	21	38	23	10	10
<b>Sc</b>	30	30	29	36	27	28
<b>V</b>	307	300	281	325	291	316
<b>Ba</b>	344	382	370	370	402	350
<b>Rb</b>	25	31	32	28	39	34
<b>Sr</b>	745	680	688	697	682	754
<b>Zr</b>	67	72	70	62	76	72
<b>Y</b>	20.26	21.15	19.43	18.78	20.32	19.88
<b>Nb</b>	6.2	6.3	6.1	5.4	6.8	6.4
<b>Th</b>	3.29	4.08	4.02	4.03	4.62	4.20
<b>Hf</b>	1.76	1.88	1.80	1.66	1.88	1.77
<b>U</b>	1.16	1.39	1.38	1.28	1.54	1.31
<b>Pb</b>	4.25	4.72	4.40	4.68	4.48	4.21
<b>Cs</b>	0.28	0.30	0.71	0.65	0.57	0.49
<b>La</b>	17.48	20.94	20.40	19.61	23.38	20.41
<b>Ce</b>	34.00	39.35	38.16	37.42	43.07	38.72
<b>Pr</b>	4.21	4.80	4.68	4.61	5.11	4.69
<b>Nd</b>	17.32	19.02	18.88	18.69	19.94	18.93
<b>Sm</b>	3.96	4.31	4.09	4.34	4.27	4.23
<b>Eu</b>	1.23	1.30	1.23	1.28	1.31	1.30
<b>Gd</b>	3.84	4.04	3.83	3.95	4.01	4.01
<b>Tb</b>	0.61	0.63	0.61	0.61	0.65	0.63
<b>Dy</b>	3.69	3.88	3.61	3.65	3.84	3.79
<b>Ho</b>	0.76	0.79	0.73	0.74	0.78	0.75
<b>Er</b>	2.09	2.14	2.04	1.98	2.16	2.08
<b>Tm</b>	0.31	0.32	0.30	0.28	0.31	0.30
<b>Yb</b>	1.92	1.96	1.87	1.75	1.96	1.87
<b>Lu</b>	0.31	0.31	0.29	0.28	0.32	0.30
<b>La/Yb</b>	9.12	10.68	10.94	11.20	11.92	10.90
<b>Eu/Eu*</b>	0.96	0.95	0.95	0.94	0.97	0.97



Table 3. Continued

<b>Sample</b>	<b>10-9</b>	<b>10-15</b>	<b>10-6</b>	<b>10-11</b>	<b>10-2</b>	<b>10-4</b>
<b>Group</b>	<b>2</b>	<b>2</b>	<b>2</b>	<b>2</b>	<b>2a</b>	<b>2a</b>
<b>SiO<sub>2</sub> (wt.%)</b>	53.65	55.01	57.57	62.87	51.59	51.93
<b>TiO<sub>2</sub></b>	0.74	0.75	0.67	0.60	0.82	0.81
<b>Al<sub>2</sub>O<sub>3</sub></b>	18.29	18.06	17.85	16.98	18.90	19.31
<b>FeO*</b>	8.61	8.49	6.93	5.44	9.41	9.03
<b>MnO</b>	0.17	0.16	0.14	0.15	0.18	0.17
<b>MgO</b>	4.26	3.75	3.64	2.08	4.44	4.25
<b>CaO</b>	9.14	8.77	7.95	5.21	10.33	10.12
<b>Na<sub>2</sub>O</b>	3.07	2.91	3.04	3.67	2.72	2.73
<b>K<sub>2</sub>O</b>	1.82	1.87	1.98	2.79	1.37	1.41
<b>P<sub>2</sub>O<sub>5</sub></b>	0.25	0.23	0.23	0.23	0.25	0.24
<b>Ni (ppm)</b>	10	13	10	3	13	13
<b>Cr</b>	8	14	11	3	10	8
<b>Sc</b>	25	26	26	15	29	26
<b>V</b>	274	277	229	125	317	312
<b>Ba</b>	468	442	512	575	355	353
<b>Rb</b>	52	53	54	87	35	33
<b>Sr</b>	662	713	638	714	750	764
<b>Zr</b>	92	86	94	130	72	72
<b>Y</b>	22.65	21.34	21.31	23.51	22.14	21.89
<b>Nb</b>	8.2	7.3	8.4	11.6	5.9	6.2
<b>Th</b>	6.14	5.54	6.85	9.75	3.85	3.75
<b>Hf</b>	2.27	2.23	2.37	3.15	1.85	1.85
<b>U</b>	2.02	1.99	2.18	2.86	1.23	1.17
<b>Pb</b>	6.03	7.22	7.63	6.68	4.69	4.80
<b>Cs</b>	1.09	1.13	1.36	1.62	0.72	0.50
<b>La</b>	27.68	24.74	28.29	37.87	21.02	21.68
<b>Ce</b>	49.10	45.87	48.13	65.85	39.48	39.61
<b>Pr</b>	5.91	5.71	5.68	7.26	5.06	5.19
<b>Nd</b>	22.93	22.57	21.53	26.36	20.48	21.09
<b>Sm</b>	4.94	4.96	4.44	5.01	4.71	4.76
<b>Eu</b>	1.39	1.42	1.29	1.46	1.40	1.42
<b>Gd</b>	4.53	4.50	4.10	4.44	4.27	4.44
<b>Tb</b>	0.70	0.69	0.64	0.70	0.68	0.69
<b>Dy</b>	4.17	4.08	3.89	4.26	4.07	4.12
<b>Ho</b>	0.86	0.82	0.80	0.88	0.84	0.84
<b>Er</b>	2.36	2.23	2.18	2.46	2.24	2.31
<b>Tm</b>	0.35	0.33	0.32	0.37	0.33	0.33
<b>Yb</b>	2.20	2.04	2.09	2.44	2.07	2.07
<b>Lu</b>	0.35	0.33	0.34	0.41	0.33	0.33
<b>La/Yb</b>	12.60	12.15	13.54	15.54	10.15	10.48
<b>Eu/Eu*</b>	0.90	0.92	0.92	0.95	0.96	0.95

Table 3. Continued

<b>Sample Group</b>	<b>10-7 3</b>	<b>10-18 3</b>	<b>10-1 4</b>	<b>10-14 4</b>	<b>10-3 4</b>	<b>10-8 5</b>
<b>SiO<sub>2</sub> (wt.%)</b>	52.60	52.73	57.26	58.46	61.61	58.72
<b>TiO<sub>2</sub></b>	0.76	0.78	0.65	0.64	0.58	0.60
<b>Al<sub>2</sub>O<sub>3</sub></b>	18.13	18.28	17.51	17.70	17.37	18.26
<b>FeO*</b>	8.65	9.25	7.07	6.56	5.58	6.53
<b>MnO</b>	0.16	0.17	0.14	0.14	0.12	0.17
<b>MgO</b>	5.02	4.70	3.72	3.12	2.59	2.71
<b>CaO</b>	10.41	9.92	8.04	7.35	5.80	6.42
<b>Na<sub>2</sub>O</b>	2.58	2.60	3.13	3.26	3.37	3.58
<b>K<sub>2</sub>O</b>	1.50	1.36	2.24	2.54	2.75	2.59
<b>P<sub>2</sub>O<sub>5</sub></b>	0.18	0.21	0.23	0.24	0.23	0.42
<b>Ni (ppm)</b>	18	12	13	10	6	5
<b>Cr</b>	17	7	14	12	9	5
<b>Sc</b>	33	31	24	22	18	14
<b>V</b>	323	335	215	197	187	147
<b>Ba</b>	403	352	510	560	606	589
<b>Rb</b>	37	34	67	75	84	85
<b>Sr</b>	713	661	643	646	580	666
<b>Zr</b>	69	66	100	108	118	138
<b>Y</b>	6.5	21.06	21.42	22.22	19.27	26.59
<b>Nb</b>	4.45	5.2	8.6	9.3	9.1	18.6
<b>Th</b>	4.10	4.00	7.34	8.09	9.37	8.29
<b>Hf</b>	1.44	1.78	2.54	2.71	2.88	3.26
<b>U</b>	5.05	1.33	2.42	2.68	2.96	2.48
<b>Pb</b>	5.20	4.65	7.20	7.42	5.89	6.71
<b>Cs</b>	0.87	0.52	1.64	1.79	1.14	1.93
<b>La</b>	21.18	21.46	29.07	31.04	33.34	43.17
<b>Ce</b>	36.80	39.32	50.13	55.70	57.63	75.58
<b>Pr</b>	4.77	4.91	6.02	6.32	6.38	8.64
<b>Nd</b>	19.37	19.76	22.97	24.01	22.85	31.53
<b>Sm</b>	4.43	4.45	4.80	4.85	4.53	6.00
<b>Eu</b>	1.28	1.36	1.35	1.36	1.22	1.68
<b>Gd</b>	4.04	4.23	4.27	4.34	3.78	5.07
<b>Tb</b>	0.63	0.66	0.66	0.67	0.60	0.78
<b>Dy</b>	3.80	3.97	3.99	3.98	3.50	4.65
<b>Ho</b>	0.77	0.79	0.82	0.80	0.71	0.96
<b>Er</b>	2.08	2.19	2.21	2.25	1.99	2.64
<b>Tm</b>	0.30	0.32	0.33	0.33	0.30	0.40
<b>Yb</b>	1.88	2.01	2.14	2.07	1.99	2.57
<b>Lu</b>	0.30	0.31	0.35	0.34	0.32	0.43
<b>La/Yb</b>	11.29	10.70	13.60	15.02	16.79	16.81
<b>Eu/Eu*</b>	0.93	0.96	0.91	0.91	0.90	0.93

Table 3. Continued

<b>Sample Group</b>	<b>10-10 5</b>
<b>SiO<sub>2</sub> (wt.%)</b>	62.26
<b>TiO<sub>2</sub></b>	0.58
<b>Al<sub>2</sub>O<sub>3</sub></b>	17.21
<b>FeO*</b>	5.87
<b>MnO</b>	0.15
<b>MgO</b>	2.18
<b>CaO</b>	5.18
<b>Na<sub>2</sub>O</b>	3.56
<b>K<sub>2</sub>O</b>	2.75
<b>P<sub>2</sub>O<sub>5</sub></b>	0.26
<b>Ni (ppm)</b>	1
<b>Cr</b>	5
<b>Sc</b>	14
<b>V</b>	142
<b>Ba</b>	576
<b>Rb</b>	87
<b>Sr</b>	644
<b>Zr</b>	130
<b>Y</b>	21.29
<b>Nb</b>	11.8
<b>Th</b>	9.90
<b>Hf</b>	3.15
<b>U</b>	2.85
<b>Pb</b>	6.36
<b>Cs</b>	1.68
<b>La</b>	35.80
<b>Ce</b>	62.00
<b>Pr</b>	6.67
<b>Nd</b>	23.79
<b>Sm</b>	4.57
<b>Eu</b>	1.36
<b>Gd</b>	4.09
<b>Tb</b>	0.64
<b>Dy</b>	3.85
<b>Ho</b>	0.79
<b>Er</b>	2.23
<b>Tm</b>	0.35
<b>Yb</b>	2.30
<b>Lu</b>	0.38
<b>La/Yb</b>	15.56
<b>Eu/Eu*</b>	0.96

\*Major elements normalized on anhydrous basis in wt. %; trace elements in ppm. Major elements and Ni, Cr, Sc, V, Ba, Rb, Sr, Zr, Nb analyses done by X-ray fluorescence (XRF) at Washington State University; all others done by inductively coupled plasma mass spectrometry (ICP-MS) at WSU. Samples are arranged by eruption Group.  $Eu/Eu^* = (Eu/0.0735) * ((Sm/0.195) * (Gd/0.259))^{(-1/2)}$ .

## Whole Rock Sr and Nd Isotope Data

The whole rock samples range in  $^{87}\text{Sr}/^{86}\text{Sr}$  from 0.70423-0.70482 (Table 4, Figure 9a). Samples from ~51-55 wt.%  $\text{SiO}_2$  display both high and low Sr isotope values. Lower Sr isotope values (~0.70423-0.70448) remain constant with a slight decrease in the highest silica samples, while higher Sr isotope values (~0.70466-0.70482) decrease with increasing silica content. There is no systematic relationship in Sr isotopes among samples.

Table 4. Whole rock Sr and Nd isotope data.

Sample	$^{87}\text{Sr}/^{86}\text{Sr}$	$2\sigma$ uncertainty	$^{143}\text{Nd}/^{144}\text{Nd}$	$2\sigma$ uncertainty
<b>Group 1</b>				
Fil 10-21	0.70448	0.000011	0.51276	0.000011
Fil 10-16	0.70482	0.000013	0.51273	0.000013
<b>Group 2</b>				
Fil 10-6	0.70430	0.000010	0.51278	0.000010
Fil 10-9	0.70438	0.000013	0.51276	0.000015
Fil 10-11	0.70423	0.000011	0.51278	0.000028
Fil 10-13	0.70437	0.000013	0.51276	0.000012
Fil 10-15	0.70466	0.000015	0.51271	0.000014
Fil 10-20	0.70431	0.000013	0.51279	0.000010
Fil 10-22	0.70448	0.000013	0.51274	0.000021
Fil 10-23	0.70447	0.000011	0.51272	0.000010
<b>Group 2a</b>				
Fil 10-2	0.70442	0.000014	0.51273	0.000014
Fil 10-4	0.70446	0.000013	0.51272	0.000009
<b>Group 3</b>				
Fil 10-7	0.70438	0.000014	0.51274	0.000009
Fil 10-18			0.51275	0.000012
<b>Group 4</b>				
Fil 10-1	0.70445	0.000013	0.51272	0.000012
Fil 10-3	0.70440	0.000015	0.51273	0.000011
Fil 10-14	0.70449	0.000010	0.51281	0.000014
<b>Group 5</b>				
Fil 10-8	0.70448	0.000011	0.51277	0.000017
Fil 10-10	0.70429	0.000011	0.51288	0.000018

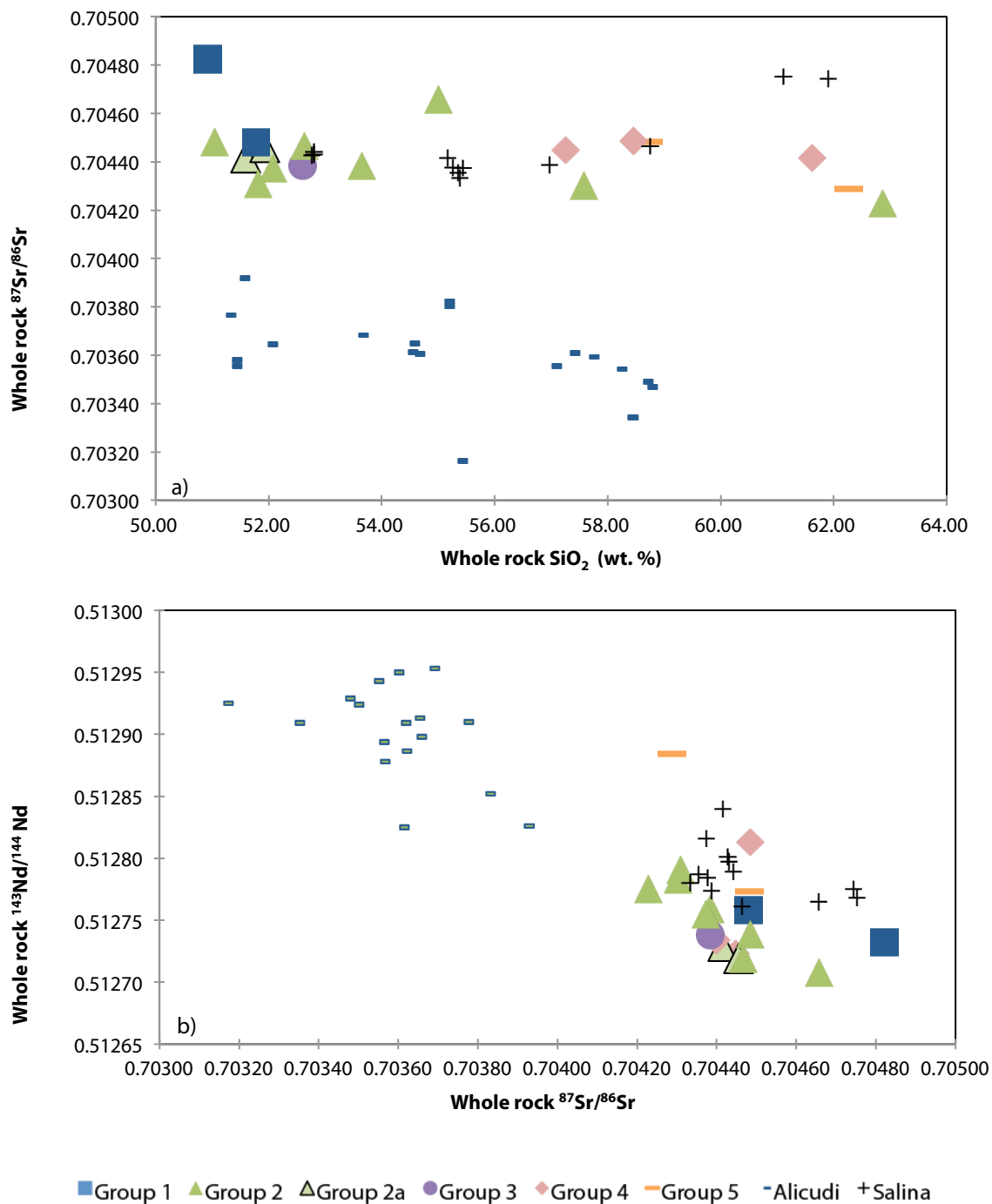


Figure 9: Whole rock isotope results for Filicudi, Alicudi and Salina. a) Whole rock  $\text{SiO}_2$  wt. % plotted against whole rock  $^{87}\text{Sr}/^{86}\text{Sr}$ . b) Whole rock  $^{87}\text{Sr}/^{86}\text{Sr}$  plotted against whole rock  $^{143}\text{Nd}/^{144}\text{Nd}$ . Symbols are same as in Figure 3.

Filicudi Nd isotopic values span a small range from 0.51271-0.51288 (Table 4). There is no systematic trend between Sr and Nd isotopes among samples. Similarly, there is no systematic relationship between Groups and Nd isotope values (Figure 9b).

Filicudi's  $^{87}\text{Sr}/^{86}\text{Sr}$  signatures mimic Salina's, whereas Alicudi has the lowest  $^{87}\text{Sr}/^{86}\text{Sr}$  signatures. Similarly, Filicudi's  $^{143}\text{Nd}/^{144}\text{Nd}$  signatures generally mimic Salina's although Filicudi's values are slightly lower. Sample FIL 10-10 is clearly the exception, as it has the highest  $^{143}\text{Nd}/^{144}\text{Nd}$  value at 0.51288 and lies within the range of the Alicudi data.

### Petrography

Seven samples were investigated microscopically in order to document phenocryst assemblages, plagioclase crystal textures, and to develop a petrographic interpretation (Table 5) (See Electronic Appendix F for detailed thin section descriptions.) For each sample, results will be presented in stratigraphic order from oldest to youngest based on Groups developed using the relative stratigraphy of Tranne *et al.* (2000) (Table 1).

### *Relative Stratigraphy*

Samples Fil 10-13, 10-15, and 10-6 represent distinct eruptive products from separate eruptive vents that are interpreted to have erupted simultaneously (Tranne *et al.*, 2000). Together, they are known as the Fossa Felici Group. Fil 10-2 has been stratigraphically documented as erupting within the same time as the Fossa Felici activity, but from a vent on the opposite side of the island (See Figure 2). Both phases

together make up the Fossa Felici Unit, Group 2, but Fil 10-2 has been noted as belonging to Group 2a since it was sampled from Monte Gaurdia.

Samples Fil 10-1 and Fil 10-3 are both from the Capo Graziano Unit, Group 4 since they are interpreted to have erupted simultaneously, but from separate vents. Fil 10-1 is from the Monte Terrione unit and Fil 10-3 was sampled from the Le Punte unit.

Sample Fil 10-10 is stratigraphically the youngest of all the samples presented in this study and is part of the Monte Montagnola Group/Stimpagnato unit or Group 5.

Table 5. Modal abundances of volcanic rocks from Filicudi Island.

Sample	Plag (%)	Cpx (%)	Ol (%)	Opx (%)	Hbl (%)	Bt (%)	Fe-Ti Oxides (%)	GM (%)	Rock Type
<b>Group 2 and 2a</b>									
Fil 10-2	30	10	9	0	0	0	1	50	B
Fil 10-13	25	15	7	0	0	0	3	50	B/BA
Fil 10-15	20	15	5	0	0	0	1	59	BA
Fil 10-6	25	7	0	3	<1	0	5	50	A
<b>Group 4</b>									
Fil 10-1	20	10	<1	3	0	0	3	53	BA
Fil 10-3	30	3	0	7	10	<1	10	40	A
<b>Group 5</b>									
Fil 10-10	20	5	0	3	3	1	7	61	A

Note: Abbreviations are as follows: plag=plagioclase, cpx=clinopyroxene, ol= olivine, gm=groundmass, opx= orthopyroxene, hbl=hornblende, bt= biotite; % are volume percent (modal abundances); modes are for phenocrysts phases and groundmass; B= Basalt, BA= Basaltic Andesite, A = Andesite. Samples are arranged by eruption Groups.

*Group 2- Fossa Felici*

Sample Fil 10-13 is vesiculated, clinopyroxene-olivine basalt to basaltic andesite with 52 wt.% SiO<sub>2</sub> (Figure 10). The sample is hypocrySTALLINE, and is highly porphyritic, with phenocrysts making up ~50% vol. of the sample. Phenocrysts include: plagioclase (plag, described in more detail below), euhedral clinopyroxene (cpx), anhedral-resorbed olivine (ol) with iddingsite rims, and Fe-Ti oxides. Groundmass microphenocrysts are the same as phenocrysts, but with more anhedral and inter-granular textures. Plagioclase

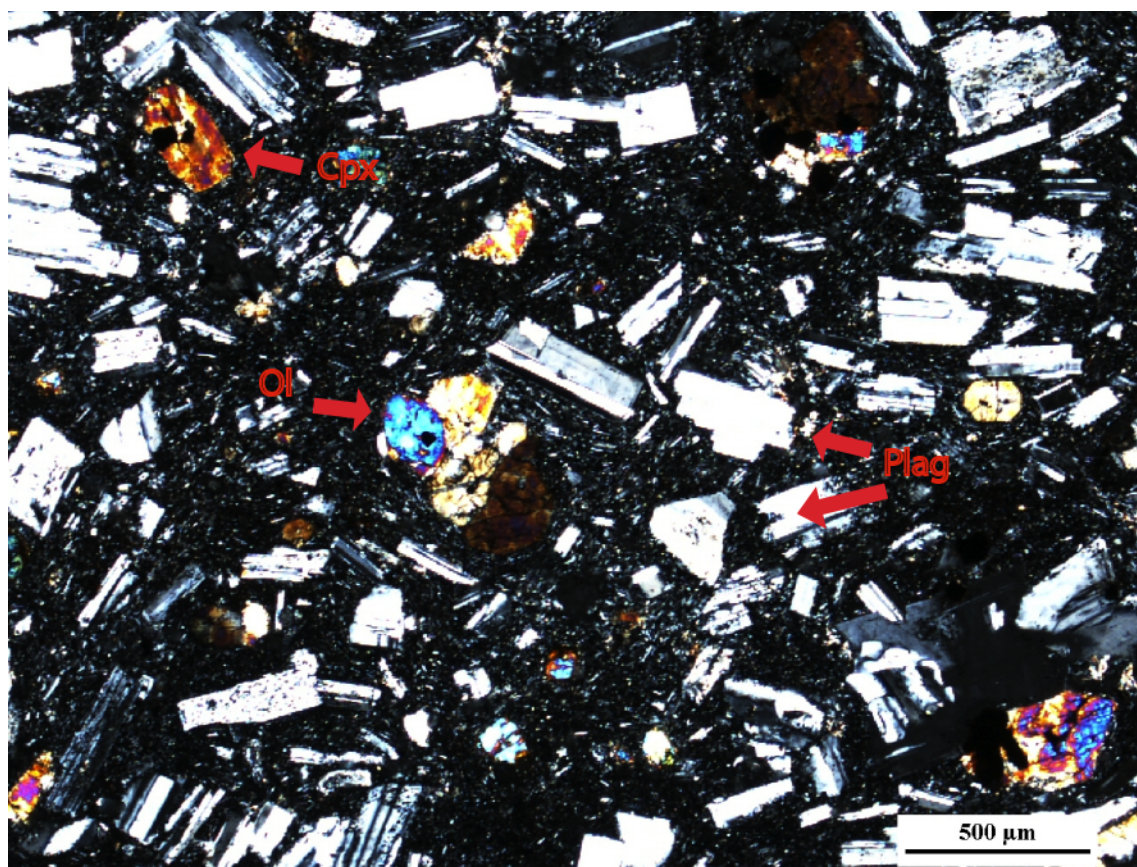


Figure 10: Cross-polar (XP) photomicrograph of basalt, Fil 10-13, from Group 2 on Filicudi. Phases present are plagioclase (plag), clinopyroxene (cpx), and olivine (ol), and Fe-Ti oxides. Groundmass is composed of the same phases as phenocrysts. Black scale bar is 500  $\mu\text{m}$ .



phenocrysts exhibit simple twinning, monotonous cores with occasional cpx inclusions up to 100  $\mu\text{m}$ , and rims that are either anhedral or show spongy sieving followed by euhedral overgrowth (Figures 10 and 11).

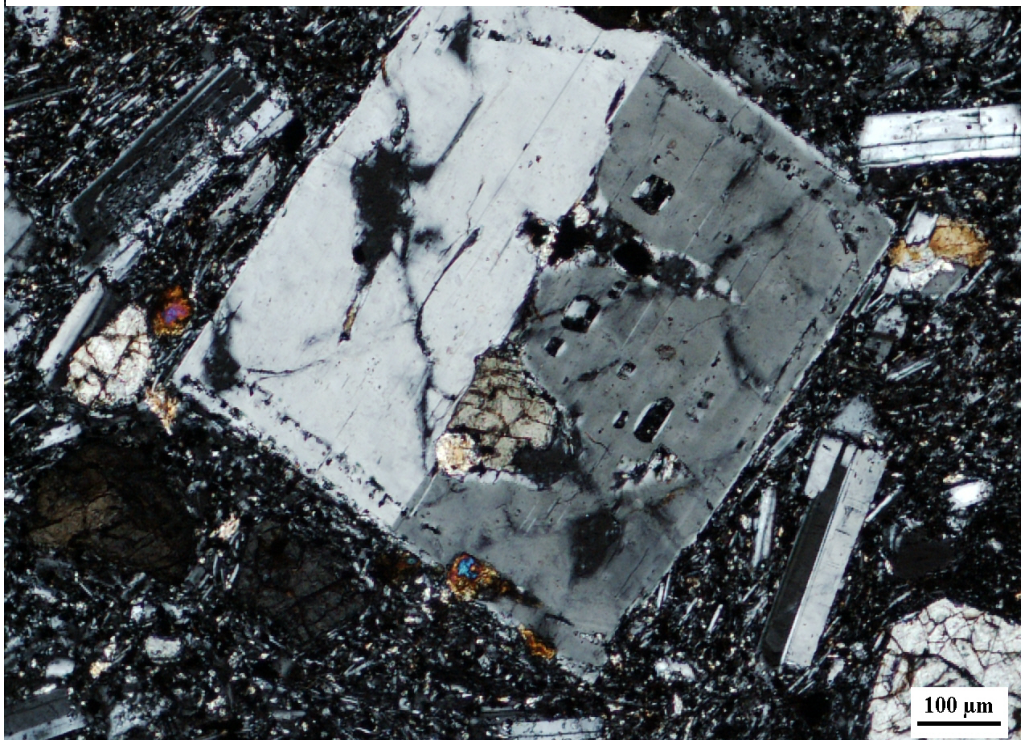


Figure 11: Cross-polar (XP) photomicrograph of plagioclase with clinopyroxene inclusion in basalt, Fil 10-13, from Group 2 on Filicudi. Black scale bar is 100  $\mu\text{m}$ .

Fil 10-15 is a vesiculated, glomerocryst-bearing, olivine-clinopyroxene basaltic andesite with 55 wt.%  $\text{SiO}_2$  (Figure 12). The sample is hypocrystalline, porphyritic (~41% vol. of the sample) and has a glassy/felty/trachytic groundmass texture. Phenocrysts include: plagioclase, anhedral clinopyroxene, anhedral olivine with orthopyroxene (opx) rims (some grains being completely pseudomorphed to opx), and Fe-Ti oxides. Groundmass microphenocrysts are the same as phenocrysts but are more

euohedral and with the added presence of euohedral elongate opx laths and trace hornblende. Glomerocrysts have a similar mineralogy as that of the host rock, are well rounded, annealed together, and contain larger crystals compared to the average phenocryst size. Plagioclase phenocrysts exhibit cores with large glassy regions in an irregular pattern, while rims show sieving and normal or oscillatory zoning.

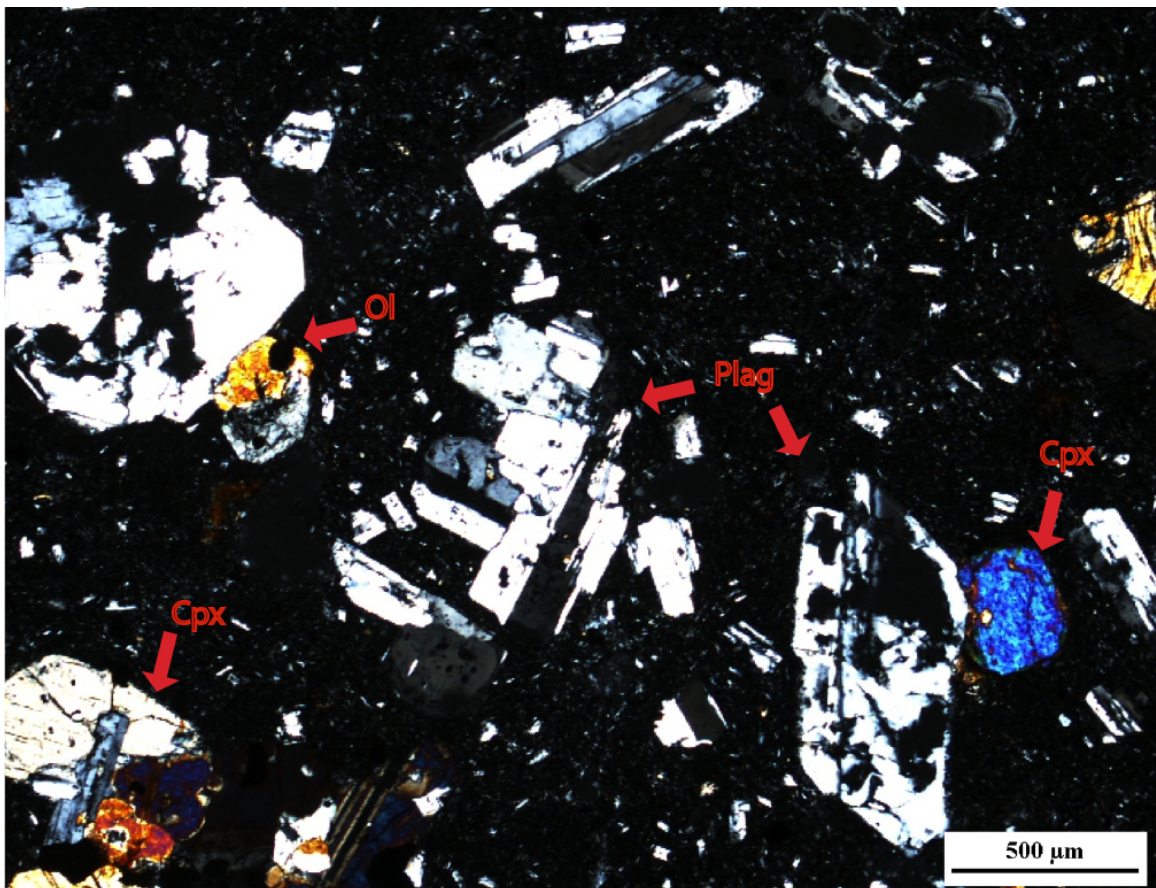


Figure 12: Cross-polar (XP) photomicrograph of basalt/basaltic andesite, Fil 10-15, from Group 2 on Filicudi. Phases present are plagioclase (plag) exhibiting cores with large glassy regions in an irregular pattern, and rims with euhedral growth, clinopyroxene (cpx), olivine (ol) mantled with orthopyroxene (opx), and Fe-Ti oxides. Groundmass microphenocrysts are the same as phenocrysts but more euhedral and with the added presence of euhedral elongate opx laths and trace hornblende. Black scale bar is 500  $\mu\text{m}$



Sample Fil 10-6, is a vesiculated hornblende-bearing, 2-pyroxene andesite with 57.6 wt.% SiO<sub>2</sub> (Figure 13). The sample is hypocrystalline seriate and highly porphyritic, with the phenocryst content making up ~50% vol. of the sample. Phenocrysts include: plagioclase, euhedral clinopyroxene, subhedral resorbed orthopyroxene, and anhedral hornblende that is almost completely reacted to opaque minerals (Figure 14).

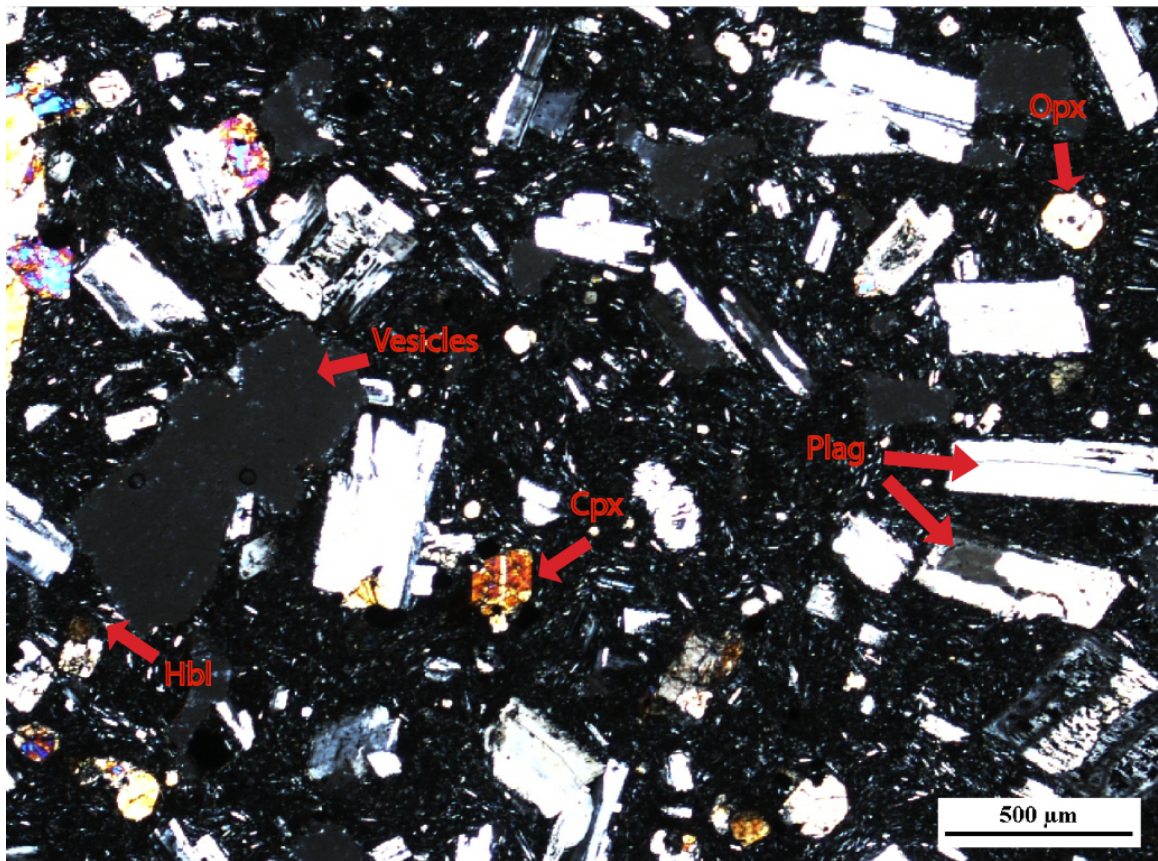


Figure 13: Cross-polar (XP) photomicrograph of basaltic andesite, Fil 10-6, from Group 2 on Filicudi. Phases present are plagioclase (plag), clinopyroxene (cpx), orthopyroxene (opx), hornblende (hbl) and Fe-Ti oxides. Groundmass mineralogy is the same as the phenocrysts but crystals are more anhedral and plagioclase has swallowtail features. Large vesicles are also present. Black scale bar is 500 μm.

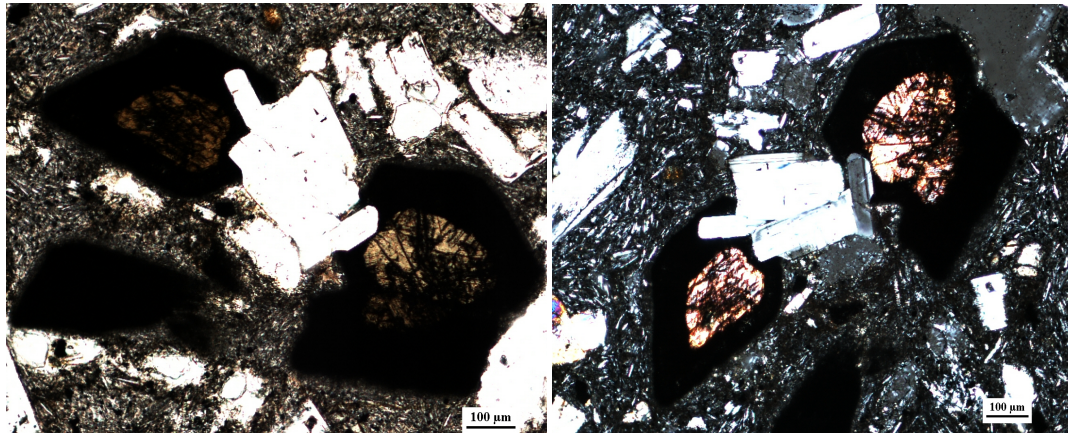


Figure 14: Photomicrographs of anhedral hornblende phenocrysts showing oxides rims in plane polar light (left) and cross-polar light (right). Imaged from basaltic andesite, Fil 10-6, from Group 2 on Filicudi. Black scale bar is 100  $\mu\text{m}$ .

Minor minerals include Fe-Ti oxides and trace amounts of apatite. Groundmass mineralogy is the same as the phenocrysts but crystals are more anhedral, and plagioclase has swallowtail features. Glomerocryst minerals are the same as in the host rock and are well rounded, annealed together, and contain large crystals compared to the average phenocryst size. Plagioclase phenocrysts display cores with monotonous/oscillatory zoning, sieve or patchy textures, and simple twinning, while rims show anhedral spongy sieving, dissolution and/or euhedral overgrowths (Figure 15).



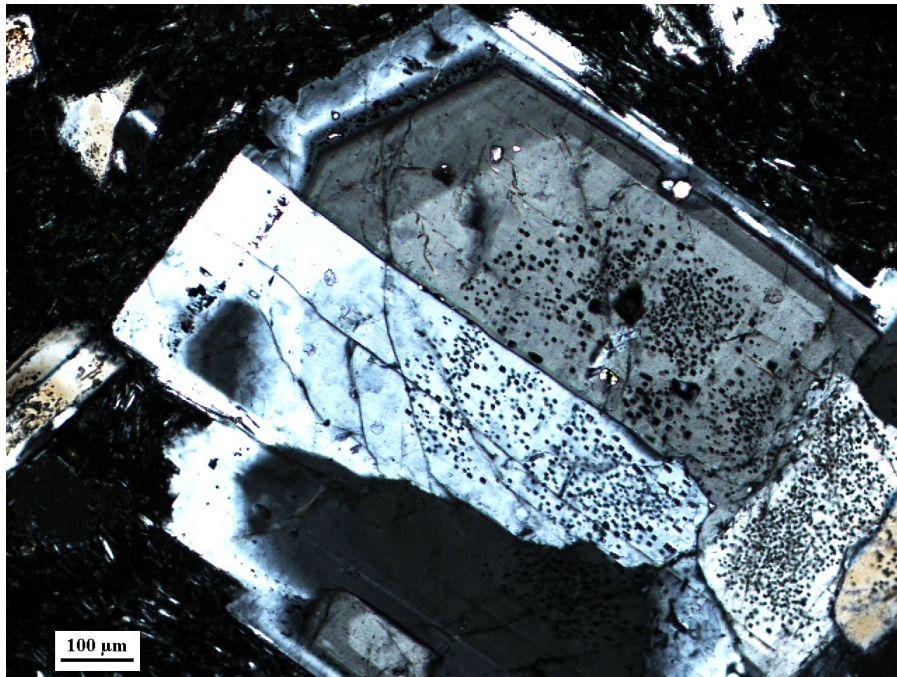


Figure 15: Cross-polar (XP) photomicrograph of plagioclase exhibiting core with boxy sieving and simple twinning, and euhedral rims. Imaged in basaltic andesite, Fil 10-6, from Group 2 on Filicudi. Black scale bar is 100  $\mu\text{m}$ .

Sample Fil 10-2, which is part of Monte Guardia (Group 2a), is highly porphyritic olivine basalt with 51.6 wt.%  $\text{SiO}_2$  (Figure 16). The sample is hypocrystalline seriate, and weakly vesiculated with an intergranular groundmass texture. Phenocrysts are large, between 0.25 and ~2.5 mm, and include: plagioclase, anhedral clinopyroxene, euhedral or skeletal olivine with overgrowth rims, and Fe-Ti oxides. Groundmass is composed of anhedral and intergranular plag, cpx, ol, and Fe-Ti oxides. Plagioclase phenocrysts display anhedral, embayed, patchy and monotonous cores, while rims show euhedral oscillatory to monotonous growth (Figure 17).

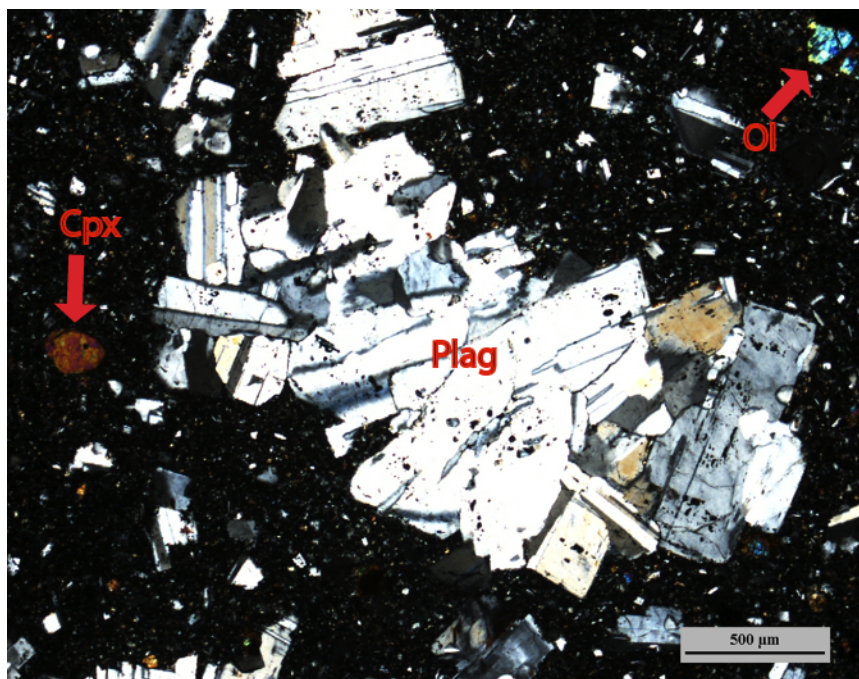


Figure 16: Cross-polar (XP) photomicrograph of basalt, Fil 10-2, from Group 2a on Filicudi. Phases present are plagioclase glomerocrysts (plag), clinopyroxene (cpx), olivine (ol), and Fe-Ti oxides. Groundmass is comprised of same phases as phenocrysts. Black scale bar is 500  $\mu\text{m}$ .

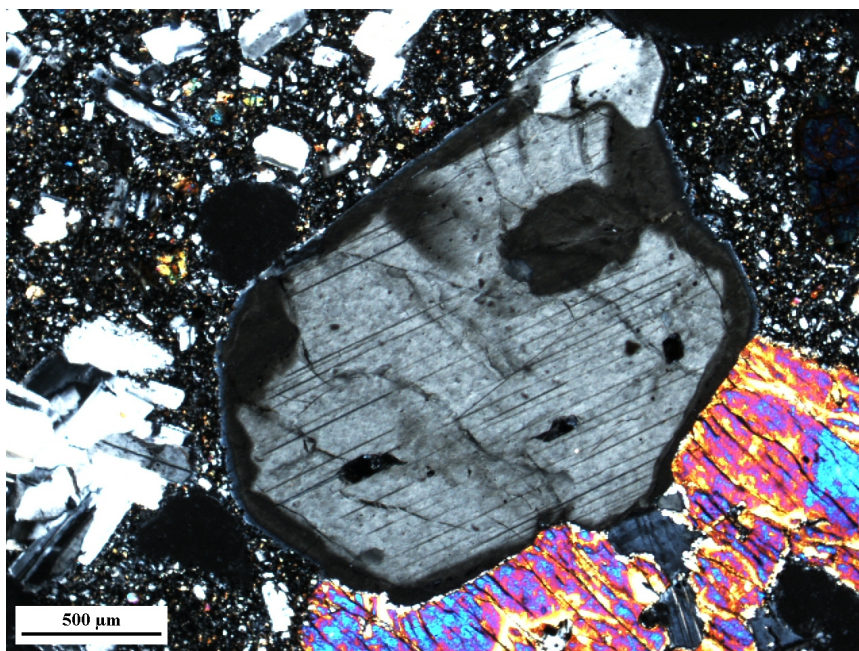


Figure 17: Cross-polar (XP) photomicrograph of plagioclase phenocrysts displaying anhedral, embayed, and monotonous cores, while rims show subhedral monotonous growth. Imaged from basalt, Fil 10-2, from Group 2a on Filicudi. Black scale bar is 500  $\mu\text{m}$ .



*Group 4- Capo Graziano*

Sample Fil 10-1 is from Monte Terrione and is an olivine bearing vesiculated 2-pyroxene andesite with a 57.3 wt.% SiO<sub>2</sub> (Figure 18). The highly porphyritic and vesiculated sample is the only andesite to still have traces of olivine but lack hornblende

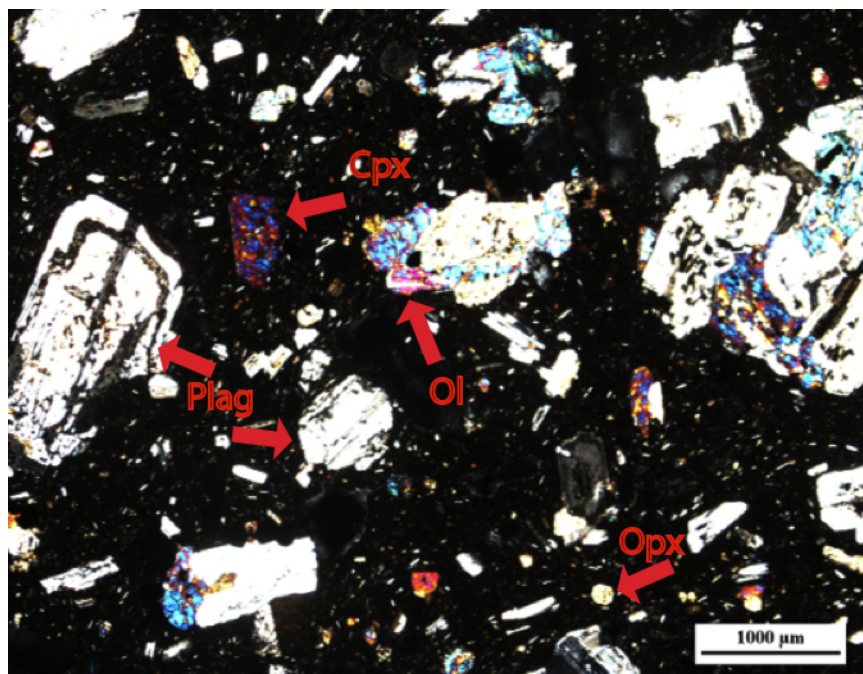


Figure 18: Cross-polar (XP) photomicrograph of basaltic andesite, Fil 10-1, from Group 4 on Filicudi. Phases present are plagioclase glomerocrysts (plag), clinopyroxene (cpx), olivine (ol), orthopyroxene (opx), and Fe-Ti oxides. Groundmass is comprised of same phases as phenocrysts. Black scale bar is 1000  $\mu\text{m}$ .

and biotite. Phenocrysts include: highly bent and broken plagioclase, subhedral and rounded clinopyroxene and orthopyroxene, clinopyroxene mantling orthopyroxene, rounded olivine with iddingsite rims, and anhedral oxides with associated staining.

Groundmass microphenocrysts are more euhedral and of the same identity as phenocrysts with the exception of olivine. Plagioclase microlites show swallowtail and needlelike quick-growth textures, while plagioclase phenocrysts show evidence for crystal breakage

and bending, highly sieved cores (both dusty and spongy), and fairly intact rims (Figure 19). Spongy areas have been filled in with other minerals in places (i.e. plagioclase, Fe-Ti oxides, olivine, cpx) and there is an overall lack of monotonous zoned phenocrysts.



Figure 19: Cross-polar (XP) photomicrograph of plagioclase phenocrysts displaying crystal bending, highly sieved cores (both dusty and spongy), and fairly anhedral monotonous rims. Imaged from basalt, Fil 10-1, from Group 4 on Filicudi. Black scale bar is 100  $\mu\text{m}$ .

Sample Fil 10-3 comes from the Le Punte unit and is a hornblende, 2-pyroxene andesite with 61.6 wt.%  $\text{SiO}_2$  (Figure 20). The porphyritic, hypocrystalline sample has the most hornblende and fewest clinopyroxene phenocrysts of any other andesite sample. Phenocrysts include: plagioclase, large (2.5 mm) euhedral hornblende, euhedral square-shaped orthopyroxene, anhedral clinopyroxene, trace biotite replaced by opaques, and euhedral Fe-Ti oxides. Groundmass microphenocrysts are euhedral and are the same minerals as the phenocrysts. Plagioclase microlites show swallowtail and needlelike



quick-growth textures, while plagioclase phenocrysts are characterized by two main groups of crystal textures (Figure 21). The first group contains plagioclase phenocrysts that are overall larger, euhedral to subhedral, complexly zoned and often are annealed together. Most have anhedral dusty resorption near rims that are mantled by euhedral oscillatory growth zones. The second group contains phenocrysts that are smaller and anhedral, with highly sieved cores that have been in filled with brown glass. Many phenocrysts within the second group are also bent and broken or are entirely filled with glass.

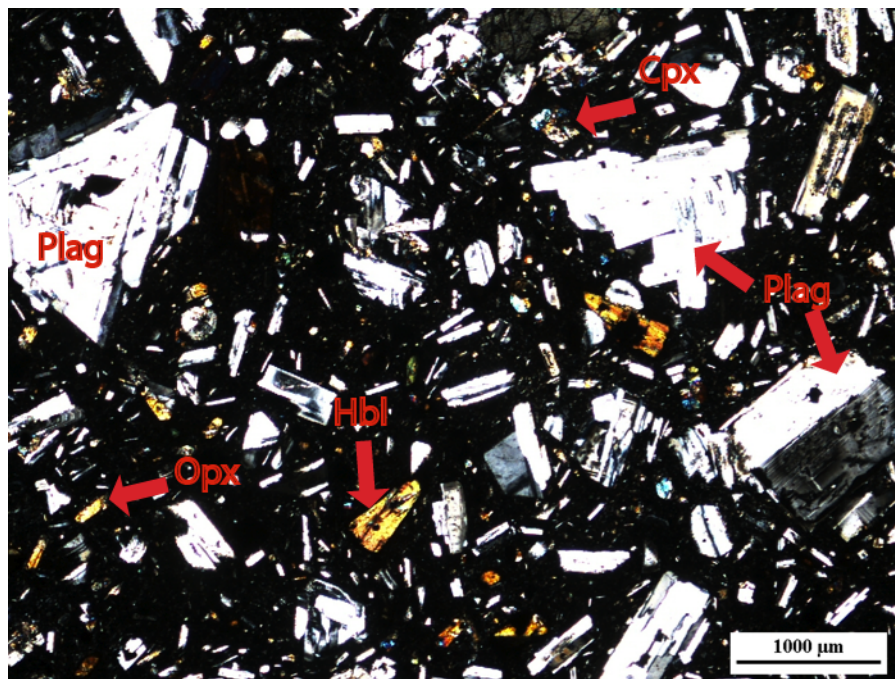


Figure 20: Cross-polar (XP) photomicrograph of andesite, Fil 10-3, from Group 4 on Filicudi. Phases present are plagioclase (plag), clinopyroxene (cpx), hornblende (hbl), orthopyroxene (opx), and Fe-Ti oxides. Groundmass is comprised of same phases as phenocrysts. Black scale bar is 1000  $\mu\text{m}$ .

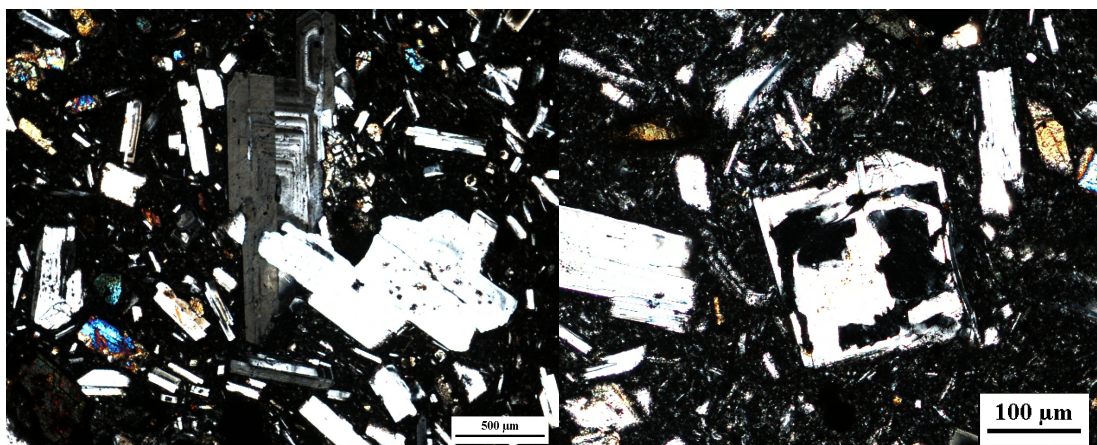


Figure 21: Cross-polar (XP) photomicrographs of the two populations of plagioclase phenocrysts in andesite Fil 10-3, of Group 4 from Filicudi. Left: within this group plagioclase phenocrysts are overall larger in size, euhedral to subhedral, complexly zoned and commonly are annealed together. Black scale bar is 500  $\mu\text{m}$ . Right: plagioclase phenocrysts within this group are smaller and anhedral, with highly sieved cores that have been in filled with brown glass. Black scale bar is 100  $\mu\text{m}$ .

#### *Group 5- Monte Montagnola*

Sample Fil 10-10 is a weakly vesiculated biotite-bearing, hornblende, 2-pyroxene andesite with 62.3 wt.%  $\text{SiO}_2$  (Figure 22). The slightly porphyritic sample has the least phenocrysts (~39 vol. %) of all the rocks examined and a glassy hypocrySTALLINE groundmass. Phenocrysts include: plagioclase, euhedral clinopyroxene and orthopyroxene, subhedral to euhedral hornblende and biotite with resorption rims of pyroxene and oxides. Groundmass microphenocrysts are rounded and anhedral and contain the same mineral assemblage as phenocrysts. Plagioclase microlites show swallowtail and needlelike quick-growth textures. Plagioclase phenocrysts display euhedral, highly sieved to patchy/spongy cores with glassy inclusions (in some cases cores are missing entirely) and oscillatory or monotonously zoned rims (Figure 23).



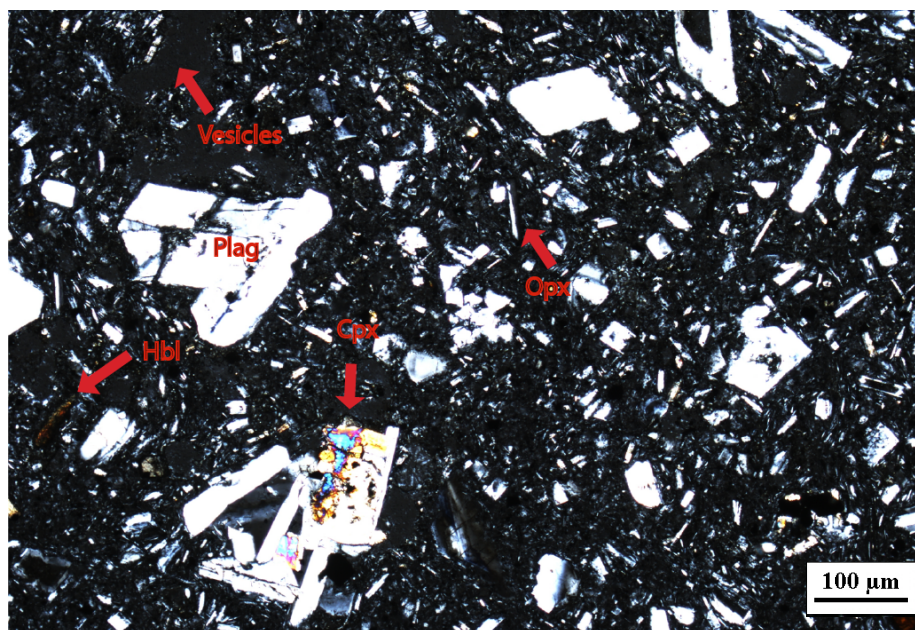


Figure 22: Cross-polar (XP) photomicrograph of andesite, Fil 10-10, from Group 5 on Filicudi. Phases present are plagioclase (plag), clinopyroxene (cpx), hornblende (hbl), orthopyroxene (opx), and Fe-Ti oxides. Groundmass is comprised of same phases as phenocrysts with large vesicles. Black scale bar is 500  $\mu\text{m}$ .



Figure 23: Cross-polar (XP) photomicrograph of plagioclase phenocrysts displaying euhedral highly sieved to patchy/spongy cores with glassy inclusions (in some cases cores are missing entirely) and oscillatory or monotonously zoned rims. Imaged from andesite, Fil 10-10, from Group 5 on Filicudi. Black scale bar is 100  $\mu\text{m}$ .

### *In situ* Plagioclase Data

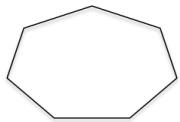
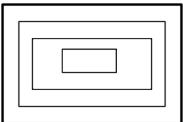
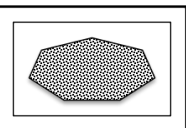
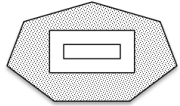
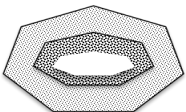
#### *Textural Types Defined by Nomarski Imaging*

Approximately 300 plagioclase crystals were imaged using the NDIC imaging technique at Central Washington University. Five main texture types were identified within the seven samples chosen for thick and thin section analysis. Identified textural types include: monotonous, complex oscillatory, sieved cores with oscillatory rims, oscillatory cores with sieved rims, and sieved cores and rims (Table 6). The five textural types were found in almost all samples within all documented sizes and are listed in order of relative abundance found within all samples.

Textural type 1 (monotonous) was more commonly found in larger crystals (Figure 24). Monotonous growth occurs when there are few to no changes within the melt from which the mineral was growing. Textural type 2 (oscillatory) was less abundant than monotonous, and displayed small-scale (< 30 mol % compositional change) oscillatory growth zones that were truncated, wavy, or displayed complex patterns within oscillations (Figure 25). Oscillations reflect changes in the solid solution end-members of albite and anorthite, and when occurring on a small-scale, represent kinetic effects within the melt from which the mineral was growing.

Textural type 3 (sieved/patchy cores with oscillatory/monotonous rims) was found to be missing completely in andesites (Figure 26). Similar to type 2, oscillations occurred on a small-scale (< 30 mol % compositional change). Sieved/patchy cores are

Table 6. Five textural types identified in Filicudi volcanic rock.

Textual Type	Sketch	Description	Interpretation
Type 1		Monotonous	Core and Rim- few changes in the melt composition from which the mineral was growing <ul style="list-style-type: none"> <li><sup>(1)</sup> High anorthite crystal introduced to a more Na-rich melt</li> </ul>
Type 2		Oscillatory	Core and Rim- reflects changes in solid solution end-members of albite and anorthite <ul style="list-style-type: none"> <li>LAHF*<sup>(2,3)</sup>: Kinetically controlled</li> <li>HALF*<sup>(2,3)</sup>: Dynamic processes (Recharge, Assimilation)</li> </ul>
Type 3		Sieved or patchy core with oscillatory/monotonous rim	Core- corrosion or sieving caused by partial dissolution <ul style="list-style-type: none"> <li><sup>(4)</sup> Albite-rich core introduced to a hotter Anorthite-rich melt (Recharge)</li> <li><sup>(3)</sup> Patchy- in filled with abundant melt (glass) and/or mineral inclusions including plagioclase (ascent)</li> </ul> Rim-return to equilibrium conditions
Type 4		Sieved rim with oscillatory/monotonous core	Rim- corrosion or sieving in rims caused by partial dissolution <ul style="list-style-type: none"> <li>Late-stage introduction of a hotter Ca-rich melt</li> <li><sup>(3)</sup> Mixing and decompression of a volatile-rich magma during ascent</li> </ul>
Type 5		Sieved/patch rim and sieved core	Core and Rim- episodes of partial dissolution <ul style="list-style-type: none"> <li><sup>(4)</sup> Albite-rich core introduced to a hotter calcium-rich melt (Recharge)</li> <li>Late-stage introduction of a hotter Anorthite melt</li> <li><sup>(3)</sup> Mixing and decompression of a volatile-rich magma during ascent</li> </ul>

Textual types are listed in order of abundance found within samples from Groups 2, 4, and 5.

<sup>(1)</sup> Tsuchiyama (1985) <sup>(2)</sup> Ginibre *et al.* (2007) <sup>(3)</sup> Humphreys *et al.* (2006) <sup>(4)</sup> Streck (2008)

\* LAHF- Low amplitude high frequency and HALF- High amplitude low frequency



attributed to rapid growth or dissolution caused by disequilibrium when a crystal reequilibrates through diffusion. Differences between patchy and sieved are related to whether or not patchy areas are filled with another mineral such as plagioclase or clinopyroxene (patchy) or glass (sieved) (Streck, 2008).

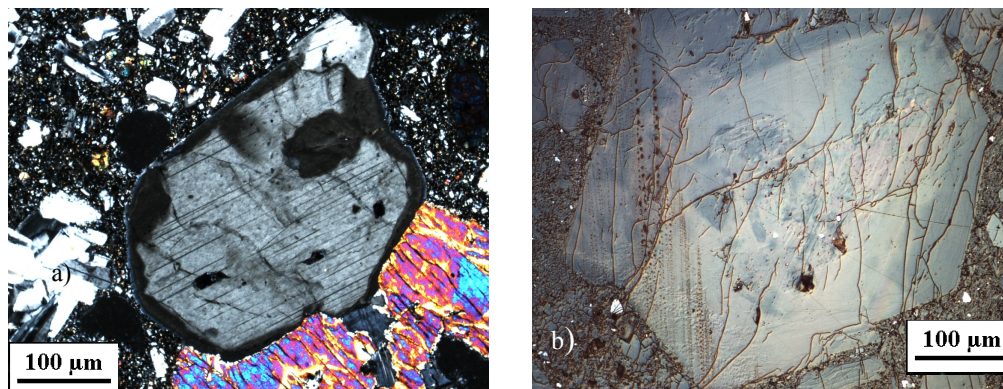


Figure 24: Example of textural type #1 (monotonous) found within Filicudi magmas. a) Cross-polar (XP) photomicrograph. Black scale bar is 100  $\mu\text{m}$ . b) NDIC image. Black scale bar is 100  $\mu\text{m}$ .

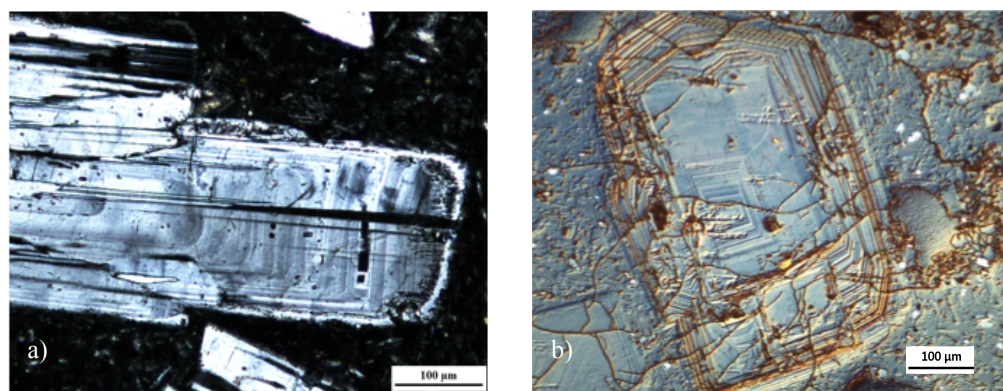


Figure 25: Example of textural type #2 (complex oscillatory) found within Filicudi magmas. a) Cross-polar (XP) photomicrograph. Black scale bar is 100  $\mu\text{m}$ . b) NDIC image. Black scale bar is 100  $\mu\text{m}$ .

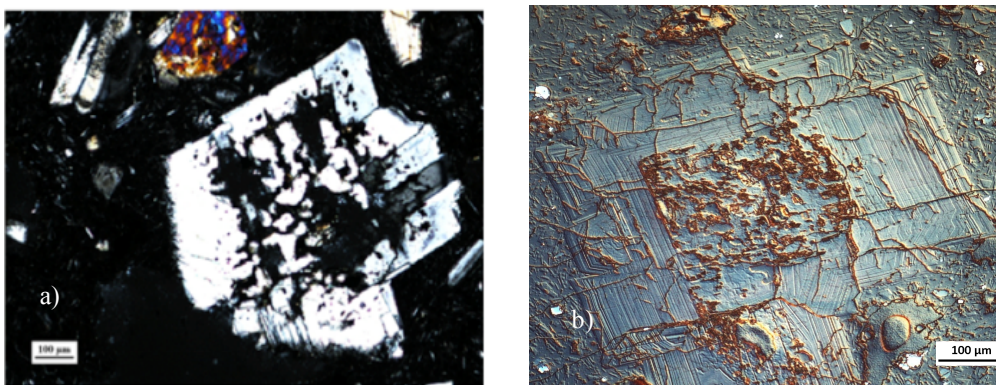


Figure 26: Example of textural type #3 (sieved/patchy core with oscillatory/monotonous rim) found within Filicudi magmas. a) Cross-polar (XP) photomicrograph. Black scale bar is 100  $\mu\text{m}$ . b) NDIC image. Black scale bar is 100  $\mu\text{m}$ .

Textural type 4 (oscillatory/monotonous cores with sieved rims) was found more commonly in medium to small crystals (Figure 27). Sieved or resorbed rims occur when dissolution of crystalline material occurs on the exterior surfaces of a crystal; the result is typically faces that are rounded and anhedral.

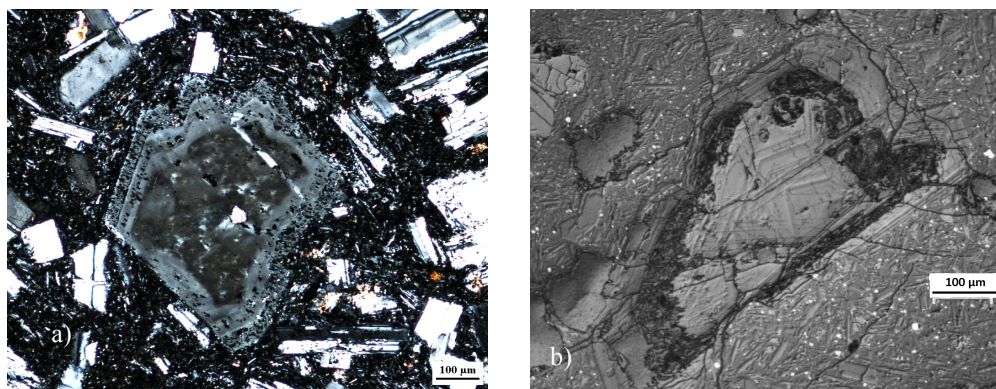


Figure 27: Example of textural type #4 (monotonous/oscillatory core with sieved/patchy rim) found within Filicudi magmas. a) Cross-polar (XP) photomicrograph. Black scale bar is 100  $\mu\text{m}$ . b) NDIC image. Black scale bar is 100  $\mu\text{m}$ .

Textural type 5 (sieved cores and rims) was absent from all basalt samples, occurred most often in andesites, and was found more commonly in medium to large



crystals (Figure 28). This texture is attributed to several dissolution/disequilibrium events, sometimes with periods of normal growth and infilling between them.

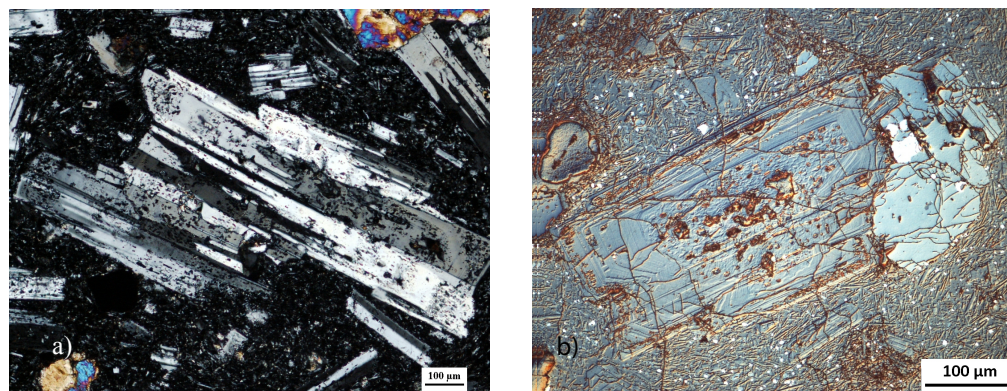


Figure 28: Example of textural type #5 (sieved/patchy core and sieved/patchy rims) found within Filicudi magmas. a) Cross-polar (XP) photomicrograph. Black scale bar is 100  $\mu\text{m}$ . b) NDIC image. Black scale bar is 100  $\mu\text{m}$ .

### *Major Element Electron Microprobe Data*

#### *Group 2- Fossa Felici*

Sample FIL 10-13 cores, intermediates and rims range in anorthite from  $\text{An}_{98}$ - $\text{An}_{53.5}$  (Figure 29) with the average of all analyses in each crystal between  $\text{An}_{93}$ - $\text{An}_{60}$  (Figure 30). Cores range from  $\text{An}_{96}$ - $\text{An}_{70}$ , rims from  $\text{An}_{96}$ - $\text{An}_{59}$ , and intermediates from  $\text{An}_{98}$ - $\text{An}_{53.5}$ . Microlites plot at  $\sim \text{An}_{90}$ ,  $\text{An}_{80}$  and  $\text{An}_{60}$ . Fil 10-15 core, intermediate and rims range from  $\text{An}_{95}$ - $\text{An}_{41.5}$  with the average of all analyses in each crystal between  $\text{An}_{90}$ - $\text{An}_{68}$ . Cores span  $\text{An}_{96}$ - $\text{An}_{46}$ , rims from  $\text{An}_{94}$ - $\text{An}_{41.5}$  and intermediates from  $\text{An}_{95}$ - $\text{An}_{45}$ . Microlites are situated at  $\sim \text{An}_{90}$ ,  $\text{An}_{80}$  and  $\text{An}_{70}$ . Fil 10-6 core, intermediate and rims range from  $\text{An}_{93}$ - $\text{An}_{46.5}$  with the average between  $\text{An}_{89}$ - $\text{An}_{57.5}$ . Cores are



characterized by  $An_{91}$ - $An_{47}$ , rims by  $An_{92}$ - $An_{57}$  and intermediates by  $An_{93}$ - $An_{47}$ .

Microlites fall at  $An_{81}$ ,  $An_{79}$  and  $An_{63}$ .

The second phase (2a) of the Fossa Felici Group, Monte Gaurdia, Fil 10-2, has the most restricted An range of all the samples (Figure 29). Fil 10-2 core, intermediate and rims fluctuate from  $An_{92}$ - $An_{63}$  with the average of all analyses in each crystal sitting between  $An_{86}$ - $An_{80}$  (Figure 30). Cores vary from  $An_{92.5}$ - $An_{77.5}$ , rims from  $An_{86}$ - $An_{80}$  and intermediates from  $An_{87}$ - $An_{75.5}$ . Microlites lie at  $\sim An_{87-73}$ , and  $An_{66-63}$ .

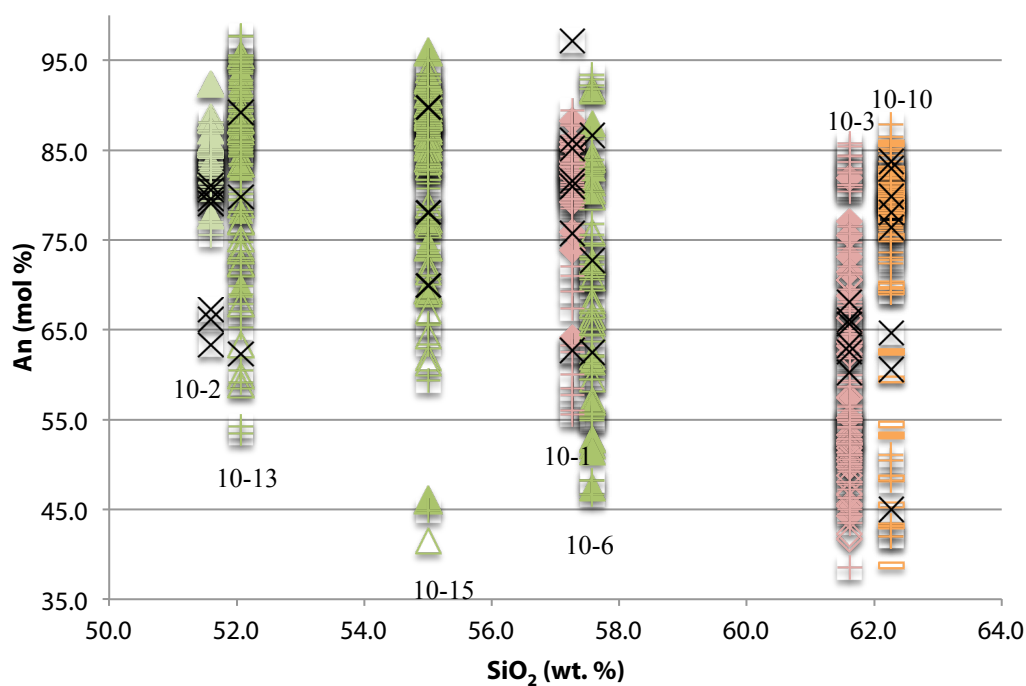


Figure 29: Whole rock  $SiO_2$  wt. % plotted against plagioclase An mol% ranges for Groups 2, 4, and 5 on Filicudi Island. Symbols are the same as in Figure 3, but cores are filled and rims are unfilled. X's correspond to microlites. Analysis locations between the inferred core and inferred rim are called the intermediate region and are marked with a cross of the same color as the group symbol.

*Group 4- Capo Graziano*

Sample Fil 10-1 cores, intermediates, and rims vary from An<sub>89</sub>-An<sub>55.5</sub> (Figure 29) with the average of all analyses in each crystal falling between An<sub>86</sub>-An<sub>61</sub> (Figure 30). Cores are characterized by An<sub>88</sub>-An<sub>64</sub>, rims by An<sub>91</sub>-An<sub>59</sub>, and intermediates by An<sub>88</sub>-An<sub>55.5</sub>. Microlites sit at ~ An<sub>97</sub>, An<sub>86-76</sub>, and An<sub>63</sub>. Fil 10-3 cores, intermediates, and rims extend from An<sub>86</sub>-An<sub>38.5</sub> (Figure 29) with the average of all analyses occurring between An<sub>75.5</sub>-An<sub>49</sub> (Figure 30). Cores vary from An<sub>82</sub>-An<sub>44</sub>, rims from An<sub>70.5</sub>-An<sub>42</sub>, and intermediates from An<sub>86</sub>-An<sub>38.5</sub>. Microlites lie between ~An<sub>68-60</sub>.

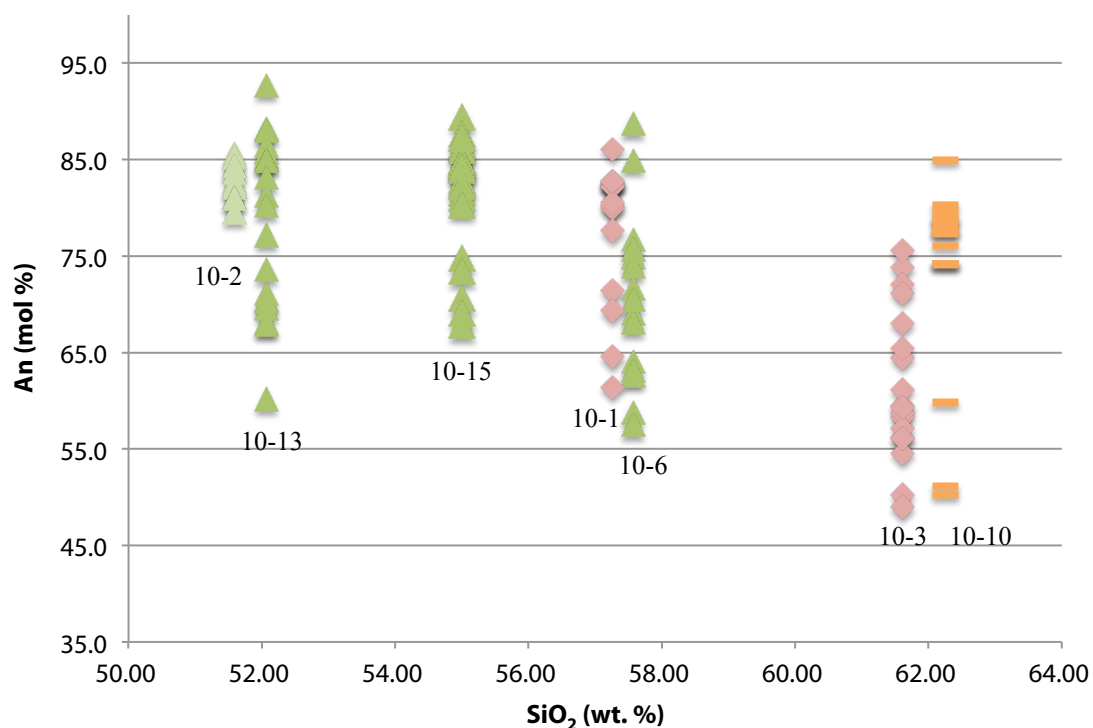


Figure 30: Whole rock SiO<sub>2</sub> wt. % plotted against average plagioclase An mol % for all samples in Groups 2, 4, and 5 on Filicudi Island. Symbols are the same as in Figure 3.


### Group 5- Monte Montagnola

Fil 10-10 core, intermediate and rims range from An<sub>88</sub>-An<sub>39</sub> (Figure 29), with the average of all analyses in each crystal spanning between An<sub>85</sub>-An<sub>74</sub> and An<sub>60</sub>-An<sub>50</sub> (Figure 30). Cores are characterized by An<sub>86</sub>-An<sub>43</sub>, rims by An<sub>82</sub>-An<sub>39</sub>, and intermediates by An<sub>88</sub>-An<sub>42</sub>. Microlites fall at ~ An<sub>84-77</sub>, An<sub>65-60</sub>, and An<sub>45</sub>.

### Changes in An from Core to Rim vs. Core An

Figure 31 shows the delta An values (rim-core) plotted against core An values in order to display normal and reverse zoning patterns. Symbols represent Groups following the stratigraphy of Tranne *et al.* (2000) (Table 1), while colors correspond to whole rock composition. Table 7 has been provided to aid in simplifying understanding of the symbology used. Normal zoning is indicated as a negative  $\Delta$ An and reverse zoning as a positive  $\Delta$ An. There is a strong correlation between core An composition and zoning within all samples. Andesites and basaltic andesites not only show the lowest core An values, but they are the only samples to show reverse zoning. Basalts show the highest core An values and are only found in the normal zoning field.

Table 7. Stratigraphic sequence of groups and rock names documented for each sample. Symbols correspond to groups while colors correspond to compositions. The table is useful for Figure 31, 34, 36, and 37.

Eruptive Group		General Symbol	Basalt	Basalt/Basaltic Andesite	Basaltic Andesite	Andesite
Oldest  Youngest	Group 1	■	■	■		
	Group 2	▲	▲	▲	▲	▲
	Group 2a	▲	▲	▲		
	Group 3	●		●		
	Group 4	◆			◆	◆
	Group 5	▬				▬

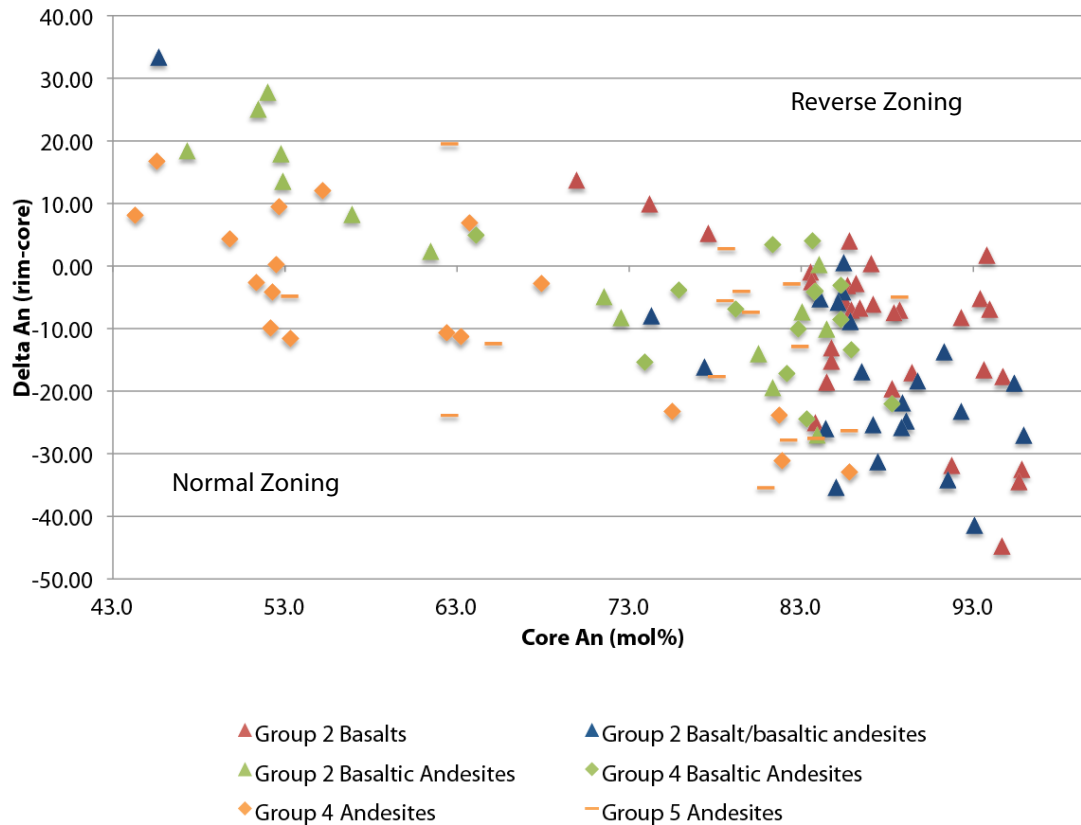


Figure 31: Delta An (rim-core) plotted against core An mol% values reported by composition and group. Colors correspond to compositions, while shapes correspond to groups (See Table 7). Positive values of  $>\Delta An_{10}$  are interpreted as evidence of recharge, while negative values of  $>\Delta An_{10}$  are interpreted as evidence of AFC. Values with changes  $<An_{10}$  are interpreted as evidence of FC processes.

### *Trace Element Data*

#### *Group 2- Fossa Felici*

Within the Group, Mg decreases with increasing whole rock SiO<sub>2</sub> content, albeit a small change, and rims have higher Mg content than cores (Figure 32a). Group 2 samples span the broadest range in Mg. Sample Fil 10-13 cores range in Mg from 314-951 ppm, while rims range from 395-2,145 ppm. Likewise, sample Fil 10-15 cores span in Mg

from 280-984 ppm, while rims range from 412-1,893 ppm. Cores of sample Fil 10-6 have Mg contents from 207-1,254 ppm, and rims from 212-1,813 ppm.

Ti within this Group lacks an overall systematic relationship with whole rock SiO<sub>2</sub> and any relationship between cores and rims (Figure 32b). Sample Fil 10-13 cores range in Ti from 44-276 ppm, while rims span from 56-510 ppm. Similarly, sample Fil 10-15 cores range in Ti from 51-425 ppm, while rims range from 72-452 ppm. Sample Fil 10-6 cores are characterized by Ti ranging in values from 101-390 ppm and rims from 41-522 ppm.

FeO within the Group increases with increasing SiO<sub>2</sub> content, while cores and rims lack any systematic variation (Figure 32c). Sample Fil 10-13 displays cores with FeO values from 0.4-0.8-wt.%, and rims from 0.4-1.0-wt.%. Likewise, Fil 10-15 cores range from 0.5-0.9-wt.%, and rims range from 0.7-1.0-wt.%. Sample Fil 10-6 cores span in FeO from 0.4-1.2-wt.%, and rims span from 0.5-0.9-wt.%.

Within Group 2, Sr lacks an overall systematic relationship with whole rock SiO<sub>2</sub> and any relationship between cores and rims (Figure 32d). Cores in sample FIL 10-13 range from 942-1,397 ppm, and rims from 985-1,944 ppm. Sample Fil 10-15 core values span a range from 668-1,584 ppm while rims range from 1,020-1,515 ppm. Moreover, sample Fil 10-6 cores encompass Sr values from 1,024-1,784 ppm and rims from 803-1,562 ppm.

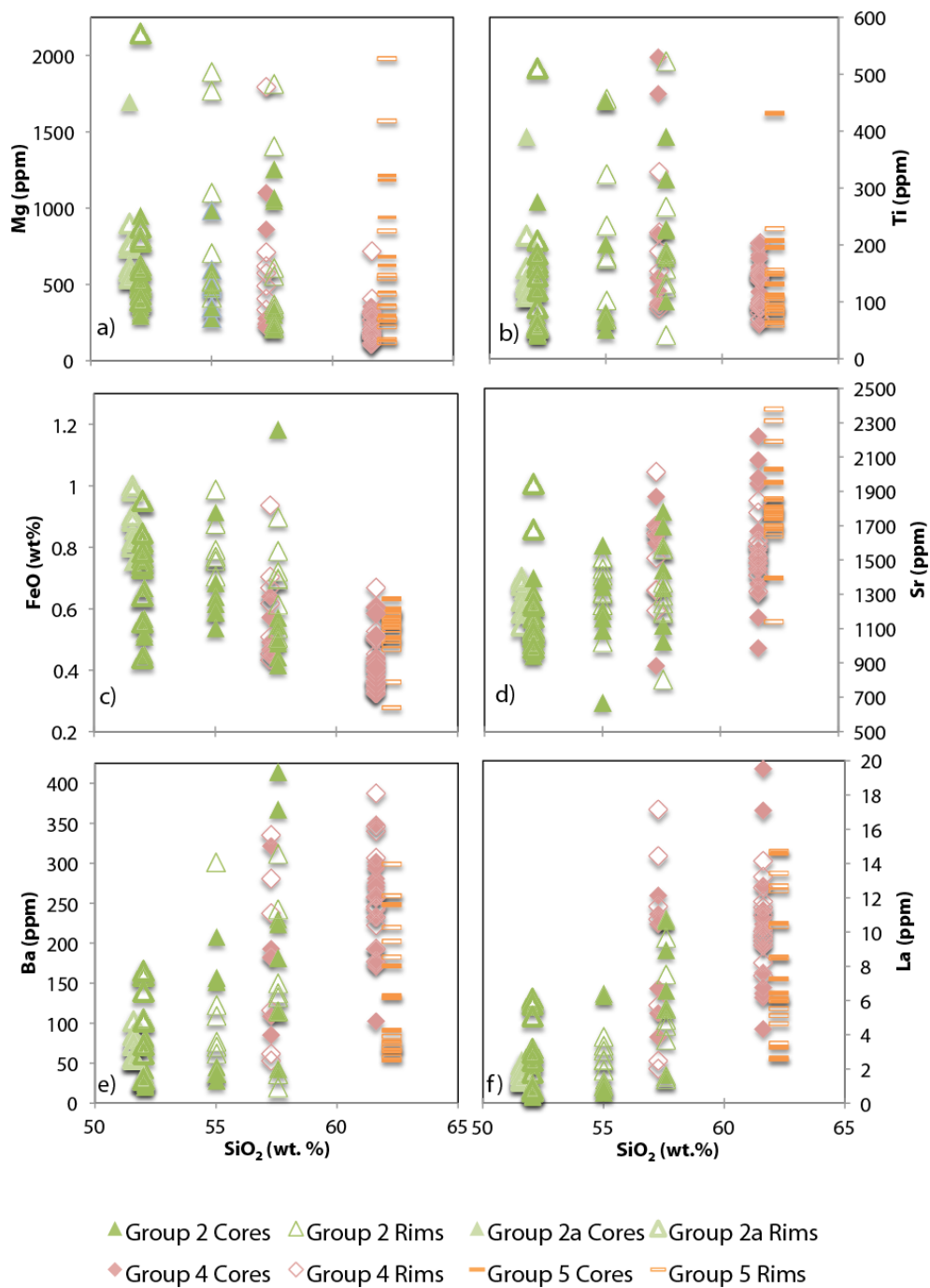


Figure 32: Whole rock  $\text{SiO}_2$  wt.% plotted against plagioclase trace elements (a) Mg (ppm), (b) Ti (ppm), (c) FeO (wt. %), (d) Sr (ppm), (e) Ba (ppm), and (f) La (ppm). Symbols are the same as in Figure 3 but cores are filled and rims are unfilled.

Ba values in Group 2 increase with increasing whole rock SiO<sub>2</sub> and lack any relationship between cores and rims (Figure 32e). Moreover, sample Fil 10-15 cores range from 28-208 ppm and rims range from 38-301 ppm. Fil 10-6 cores encompass a range from 36-414 ppm and rims from 19-312 ppm.

Generally within Group 2, La increases with increasing whole rock SiO<sub>2</sub> and lacks any relationship between cores and rims (Figure 32f). Fil 10-13 span a range from 0.4-3.2 ppm, and rims from 0.8-5.9 ppm. Likewise, cores in Fil 10-15 range from 0.6-6.4 ppm and rims range from 1.4-3.9 ppm. Sample Fil 10-6 cores are characterized by La values from 1.5-11 ppm and rims from 1.4-9.7 ppm.

Similar to An values, trace element values in Sample 10-2 of the Monte Gaurdia unit (Group 2a) were the most restricted within this sample. Cores have lower Mg values than rims with the exception of one anomalous Mg core value at 1,695 ppm. Cores range in Mg from 582-586 ppm, while rims range from 542-900 ppm (Figure 32a). Ti values in Fil 10-2 cores range from 110-138 ppm, and rims range from 109-217 ppm. Cores appear to have lower values than rims with the exception of one anomalous Ti core value at 391 ppm (Figure 32b). FeO values are the highest of all samples with the exception of one anomalous core value in sample Fil 10-6 at 1.2 ppm (Figure 32c). Overall, cores have lower FeO values than rims. Cores in sample 10-2 range from 0.8-0.9-wt.%, while rims span from 0.8-1.0-wt.%. Sr values in Fil 10-2 lack any systematic variation between cores and rims, with the cores encompassing a range from 1,201-1,321 ppm, and rims from 1,120-1,397 ppm (Figure 32d). Ba core values are lower than rim values in Fil 10-2 (Figure 32e). Cores sit between 53-79 ppm, and rims from 55-103 ppm. Lastly, La within

sample Fil 10-2 lacks a systematic variation within cores and rims (Figure 32f). Cores range from 1.3-2.5 ppm, and rims range from 1.3-1.9 ppm.

#### *Group 4- Capo Graziano*

Within Group 4, Mg decreases with increasing SiO<sub>2</sub> content, and rims have higher Mg content than cores (Figure 32a). Fil 10-1 cores range in Mg from 220-1,103 ppm, while rims range from 334-1,794 ppm. Conversely, Fil 10-3 has a very restricted range in Mg compared with the other samples, with the exception of FIL 10-2. Cores range in Mg from 110-332 ppm, with rims ranging from 114-720 ppm.

Ti within this Group decreases with increasing SiO<sub>2</sub> and cores have higher Ti values than rims (Figure 32b). Fil 10-1 cores span a range in Ti from 95-530 ppm, while rims encompass a range from 89-329 ppm. Sample Fil 10-3 has cores with Ti values from 60-204 ppm, and rims with Ti values from 70-195 ppm. Similarly, FeO within the Group decreases with increasing SiO<sub>2</sub> content, while and cores and rims lack any systematic variation (Figure 32c). Sample Fil 10-1 cores range in FeO from 0.4-0.6-wt.%, and rims range from 0.4-0.9-wt.%. Likewise, FeO values with Fil 10-3 cores range from 0.3-0.6-wt.%, and rims range from 0.3-0.7-wt.%. Conversely, Sr within Group 4 increases as SiO<sub>2</sub> increases and lacks any relationship between cores and rims (Figure 32d). Sample Fil 10-1 cores encompass a range of Sr from 883-1,871 ppm, and rims from 1,206-1,214 ppm. Cores from sample Fil 10-3 range from 985-2,200 ppm, while rims span from 1,319-1,848 ppm.



Within Group 4, the trace element Ba increases with increasing SiO<sub>2</sub> and lacks any relationship between cores and rims (Figure 32e). Cores from sample Fil 10-1 range from 85-321 ppm, while rims range from 54-336 ppm. Likewise, Fil 10-3 cores range from 102-347 ppm, while rims cluster in a smaller range from 223-388 ppm. Similar to Ba, La within Group 4 increases with increasing SiO<sub>2</sub> and lacks any relationship between cores and rims (Figure 32f). Cores from sample Fil 10-1 range from 3.8-12 ppm, and rims range from 2-17 ppm, while Fil 10-3 cores range from 4-20 ppm and rims range from 7-14 ppm.

#### *Group 5- Monte Montagnola*

Cores and rims within the Group 5 sample (Fil 10-10) have no systematic variation between them with regards to Mg (Figure 32a). Cores range in Mg from 134-1,212 ppm, while rims range from 117-1,981 ppm. Similarly, Ti value core and rims lack any systematic variations (Figure 32b). Fil 10-10 cores range from 64-431 ppm, and rims range from 59-619 ppm. FeO values are the lowest of all samples (Figure 32c). Overall rims have lower values than cores. Cores span a range from 0.5-0.6-wt.%, and rims span a range from 0.3-0.6-wt.%. Sr values of Fil 10-10 are the highest of all samples and lack any systematic variation between cores and rims (Figure 32d). Cores Sr values range from 1,395-2,030 ppm, while Sr values of rims fall between 1,140-2,379 ppm. Likewise, Ba core and rim values lack any systematic variation in sample Fil 10-10 (Figure 32e). Cores encompass a range from 54-248 ppm, and rims from 58-299 ppm. Moreover, La

within sample Fil 10-10 lacks a systematic variation within cores and rims (Figure 32a). La cores values are between 2.6-15 ppm, and rim values are between 3.5-15 ppm.

#### *Average Trace Element Abundances vs. Silica Content*

In Figure 33, plagioclase trace element core and rim averages with standard deviations are plotted against whole rock silica content. See Table 8 for complete average and standard deviation values. Symbols and colors represent Groups following the stratigraphy of Tranne *et al.* (2000) (Table 1).

Mg averages within plagioclase lack any strong systematic relationship with silica (Figure 33a). Ti averages within plagioclase lack any strong systematic relationship with silica or between cores and rims. At the upper limit, average values increase to ~57 wt. % silica range (Group 4 basaltic andesite), and then they decrease (Figure 33b).

The maximum FeO averages (core and rim) within plagioclase generally decrease with increasing silica contents. All but the most silicic samples (Group 4 and Group 5 andesites) have rim values higher than core values (Figure 33c). The maximum Sr averages (core and rim) within plagioclase generally increase within increasing silica contents. Cores and rims lack any strong systematic relationships. Group 4 samples display almost identical Sr averages and core and rim values are similar (Figure 33d).

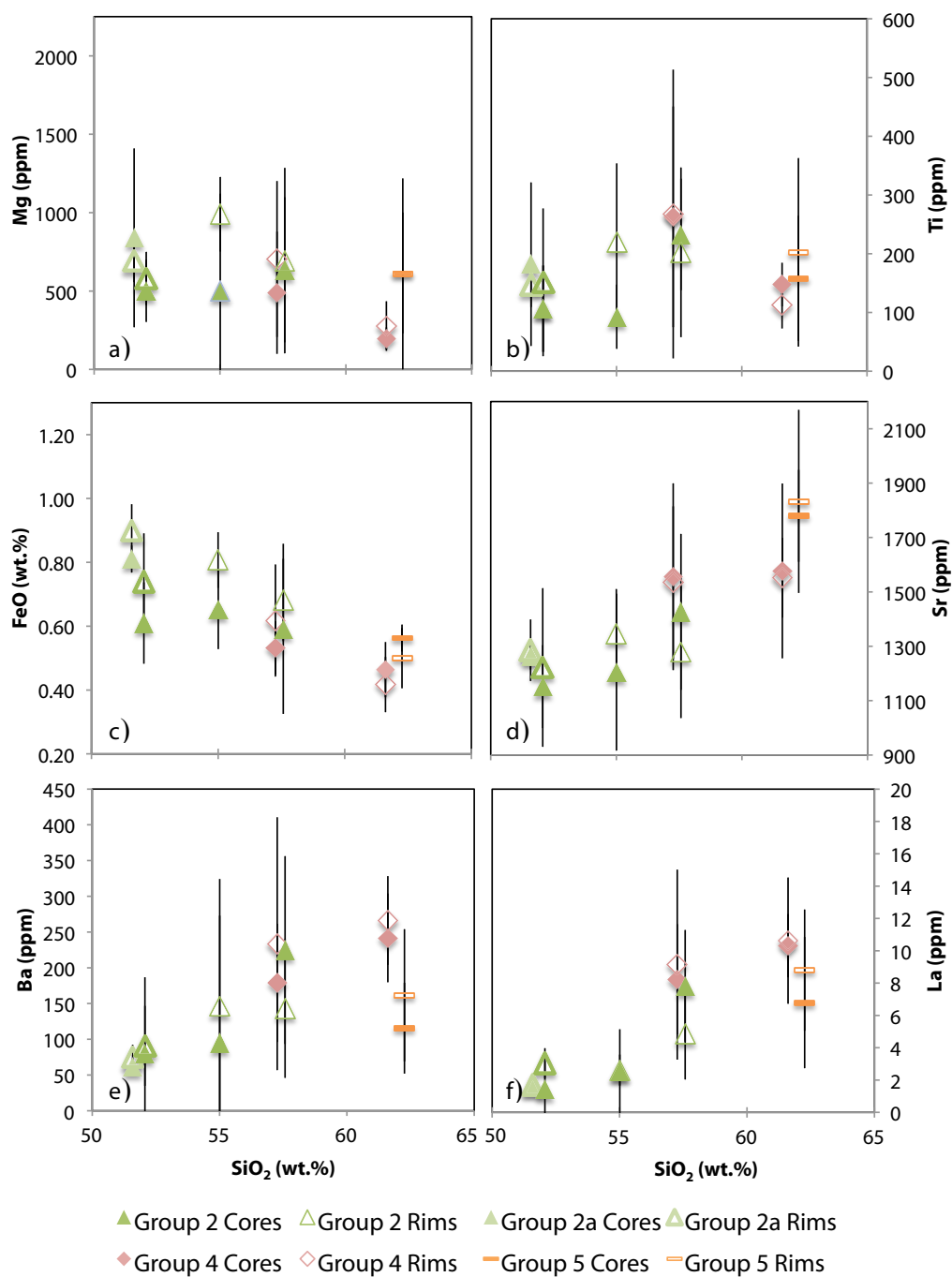


Figure 33: Whole rock  $\text{SiO}_2$  wt.% plotted against average plagioclase trace elements with standard deviations (a) Mg (ppm), (b) Ti (ppm), (c) FeO (wt. %), (d) Sr (ppm), (e) Ba (ppm), and (f) La (ppm). Symbols are the same as in Figure 3 but cores are filled and rims are unfilled.

Table 8. *In situ* plagioclase trace element averages and standard deviations.

		Ba (ppm)		FeO (wt. %)		La (ppm)		Mg (ppm)		Sr (ppm)		Ti (ppm)		
		Core	Rim	Core	Rim	Core	Rim	Core	Rim	Core	Rim	Core	Rim	
<b>Group 2</b>	10-2	AVR	61.4	74.7	0.8	0.9	1.7	1.7	839.6	691.5	1264.6	1285.4	182.2	147.0
		STDEV	10.3	16.1	0.0	0.1	0.5	0.3	494.0	123.2	43.6	103.4	120.6	34.6
	10-13	AVR	79.9	90.8	0.6	0.7	1.4	3.0	501.3	579.7	1151.7	1222.2	106.3	151.3
		STDEV	101.9	53.5	0.1	0.1	0.9	2.1	188.4	161.9	144.6	279.2	70.1	120.4
10-15	AVR	94.9	146.2	0.7	0.8	2.5	2.6	502.8	989.3	1204.9	1345.2	92.7	220.3	
	STDEV	69.2	162.4	0.1	0.1	2.4	0.9	220.0	572.5	267.0	154.6	49.9	123.5	
10-6	AVR	224.8	143.1	0.6	0.7	7.8	4.8	635.4	694.2	1426.4	1278.6	232.8	202.4	
	STDEV	121.6	90.8	0.2	0.1	3.2	2.6	428.5	553.0	265.3	226.9	87.9	135.1	
<b>Group 4</b>	10-1	AVR	178.8	233.8	0.5	0.6	8.2	9.1	489.4	704.2	1555.7	1534.7	262.8	267.6
		STDEV	75.5	163.8	0.1	0.2	3.1	5.4	356.0	460.3	313.3	259.0	171.5	227.5
	10-3	AVR	241.8	266.1	0.4	0.5	10.3	10.6	197.8	276.6	1577.2	1552.3	147.5	113.2
		STDEV	61.6	59.7	0.1	0.1	3.8	1.9	68.2	151.8	312.0	140.7	35.9	38.9
<b>Group 5</b>	10-10	AVR	115.5	161.5	0.6	0.5	6.8	8.8	615.2	609.2	1779.8	1832.7	158.1	158.2
		STDEV	59.9	88.1	0.0	0.1	3.6	3.9	365.8	563.7	160.5	322.4	101.1	153.0

AVR- Average  
STDEV- Standard Deviation

The maximum Ba and La averages (core and rim) within plagioclase increase with increasing silica with the exception of the most silicic sample (Group 5 andesite). Rims have higher Ba averages with the exception of one sample (Group 2 basaltic andesite) (Figure 33e). Core and rim average La values within plagioclase lack any systematic variations (Figure 33f).

#### *Trace Element Abundances vs. Anorthite Content*

In Figure 34, plagioclase trace element core and rim values are plotted against anorthite content and are reported by composition and Group. Symbols represent Groups following the stratigraphy of Tranne *et al.* (2000) (Table 1), while colors correspond to whole rock composition.

Mg lacks any strong systematic relationship with Anorthite content or composition, and the majority of values fall between below detection and 1,000 ppm (Figure 34a). Plagioclase crystals are normally zoned with respect to Mg in basalts, and normally and reversely zoned in basaltic andesites to andesites. The trace element Ti lacks strong correlation with An. Most values sit between ~50- 200 ppm (Figure 34b). There is a group of mainly core values with  $An_{\sim 70-85}$  that sit above the 300 ppm range. Overall, plagioclase FeO increases with increasing An content. Plagioclase FeO values in the andesites span a very restricted range from ~0.4-0.6 wt.%, while those in basalts span a larger range from ~0.4- 1.0 wt. % (Figure 34c). Basaltic andesite plagioclases overlap both the basalt and andesite ranges with values between ~0.4-0.8. Similar to Mg,

plagioclase crystals are all normally zoned within basalts with respect to FeO, and display evidence of reverse zoning within basaltic andesites and andesites.

Generally, Sr decreases with increasing An content. Andesite plagioclase crystals have the highest Sr concentrations range between 1100-2300 ppm. Plagioclases in basalts have the lowest, between 900-1500 ppm, and basaltic andesites values overlap both compositions between 1000-2100 ppm (Figure 34d). Likewise, Ba contents generally decrease with increasing An content and decreasing SiO<sub>2</sub>. Ba in plagioclase in the andesites and basaltic andesites ranges between ~50-400 ppm and basalt plagioclase shows a much more restricted range between ~20-100 ppm (Figure 34e). Similar to Sr and Ba, La values also generally decrease with increasing An content. Plagioclase in andesites has the largest range in La from ~5-16 ppm, while that in basalts has a more restricted between ~1-6 ppm. Basaltic andesite plagioclase crystals overlap both, ranging from below detection to ~10 ppm (Figure 34f).

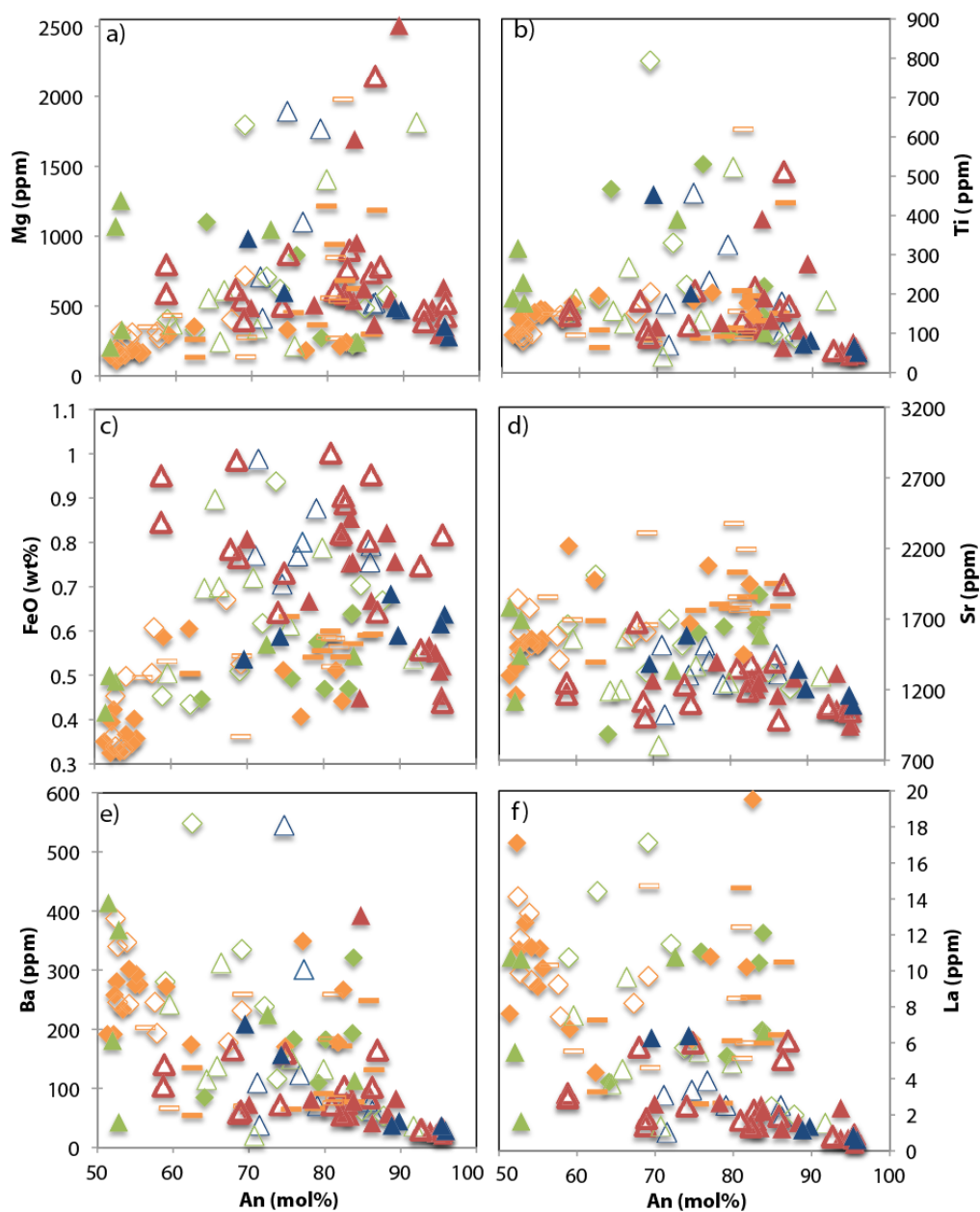


Figure 34: Plagioclase An (mol%) content plotted against plagioclase trace elements (a) Mg (ppm), (b) Ti (ppm), (c) FeO (wt. %), (d) Sr (ppm), (e) Ba (ppm), and (f) La (ppm). Colors correspond to composition, while shapes correspond to groups (See Table 7). Filled symbols represent cores values and unfilled symbols represent rim values.

*In situ Sr Isotope Data**Group 2- Fossa Felici*

Plagioclase Sr isotopes within the Group 2 samples are unsystematic with increasing whole rock silica content. Sample 10-13 has the lowest values (0.70359-0.70433), 10-15 has the highest (0.70388-0.70482), and 10-6 has the most restricted range (0.70399-0.70455) (Figure 35). Smaller phenocrysts all plot within the given ranges. There appears to be no systematic correlation between core and rim values within Group 2.

Similar to An and trace element values, Sr isotopic values for sample Fil 10-2 of the Monte Gaurdia unit (Group 2a) are the most restricted compared to all other samples. Sr isotopes range from 0.70412-0.70429, with all smaller phenocrysts falling within this restricted range (Figure 35). There appears to be no correlation between core and rim values.

*Group 4- Capo Graziano*

Group 4 plagioclase crystals exhibit increasing ranges in Sr isotopes with increasing silica contents (Figure 35). Sample Fil 10-1 ranges from 0.70407-0.70446 while Fil 10-3 ranges from 0.70368-0.70480. Smaller phenocrysts from both samples fall within the middle of each range. Both samples lack any core to rim systematic relationships.

*Group 5- Monte Montagnola*

Sample Fil 10-10 shows two main clusters of Sr isotopes (Figure 35). The first sits in the higher range between 0.70441-0.70477 and the second in the lower range



between 0.70382-0.70400. The two smaller phenocrysts also plot within each of these two main clusters. There appears to be no systematic relationships between cores and rims.

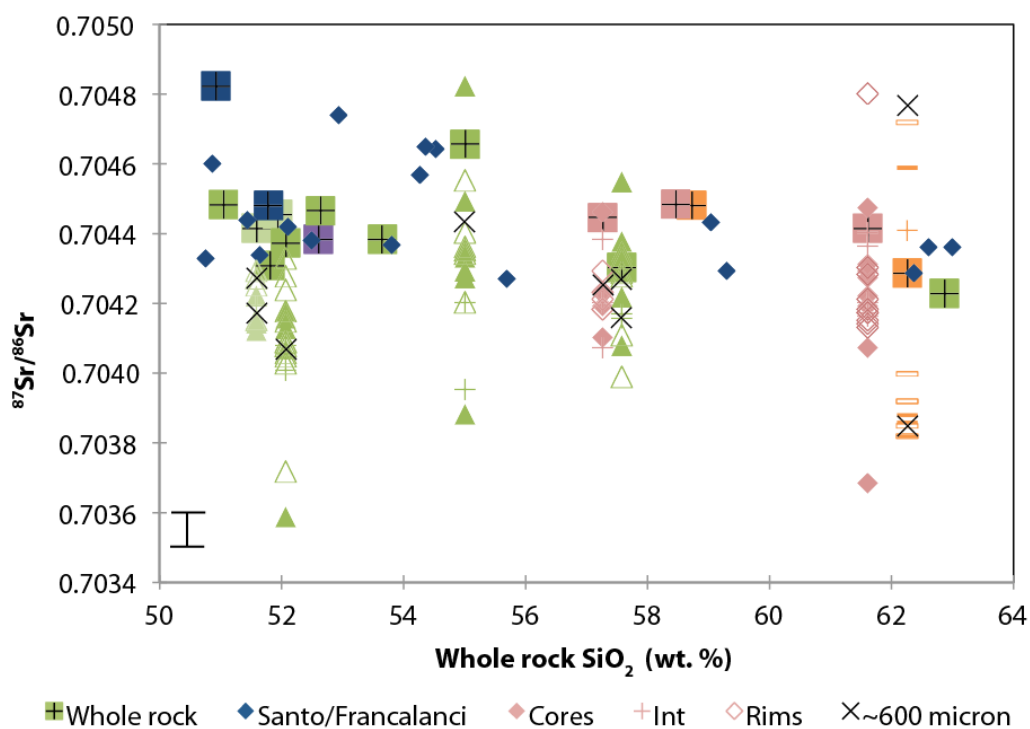


Figure 35: In situ plagioclase  $^{87}\text{Sr}/^{86}\text{Sr}$  isotopes plotted against whole rock  $\text{SiO}_2$  (wt. %) for Groups 2, 4, and 5. Uncertainty bar associated with in situ analysis. Symbols are the same as in Figure 3 but cores are filled and rims are unfilled. X's correspond to whole analyzed crystals of sufficient size (~600 microns). Whole rock  $^{87}\text{Sr}/^{86}\text{Sr}$  are plotted as squares with crosses and are colored by Group. Uncertainty is smaller than symbols ( $\pm 0.00002$ ). Blue diamond symbols represent whole rock data from Francelanci and Santo (1993) and Santo *et al.* (2004).

Table 9. *In situ* plagioclase  $^{87}\text{Sr}/^{86}\text{Sr}$  data for Groups 2, 4, and 5.

	<b>Sample</b>	$^{87}\text{Sr}/^{86}\text{Sr}$	<b>Uncertainty</b>	
<b>Group 2</b>	<b>FIL 10-13</b>	FIL 10-13-12-C	0.70413	0.00016
		FIL 10-13-12-I	0.70408	0.00016
		FIL 10-13-12-R	0.70418	0.00016
		FIL 10-13-2-R	0.70428	0.00016
		FIL 10-13-2-R2	0.70415	0.00016
		FIL 10-13-26-C	0.70416	0.00016
		FIL 10-13-26-I	0.70401	0.00016
		FIL 10-13-26-R	0.70405	0.00016
		FIL 10-13-23-C	0.70359	0.00016
		FIL 10-13-23-R	0.70372	0.00016
		FIL 10-13-36-R	0.70424	0.00016
		FIL 10-13-36-R2	0.70433	0.00016
		FIL 10-13-37-C	0.70407	0.00016
		FIL 10-13-37-R1	0.70408	0.00016
		FIL 10-13-37-R2	0.70409	0.00016
		FIL 10-13-39-R	0.70403	0.00016
		FIL 10-13-39-R2	0.70406	0.00016
		Fil 10-13-600 micron	0.70407	0.00016
		FIL 10-13-51-C	0.70418	0.00016
		FIL 10-13-51-R	0.70409	0.00016
	<b>FIL 10-15</b>	FIL 10-15-48C	0.70433	0.00039
		FIL 10-15-48R	0.70436	0.00039
		FIL 10-15-47C	0.70435	0.00039
		FIL 10-15-25C	0.70482	0.00039
		FIL 10-15-25I	0.70420	0.00039
		FIL 10-15-25R	0.70420	0.00039
		FIL 10-15-30C	0.70427	0.00039
		FIL 10-15-30R	0.70440	0.00039
		FIL 10-15-20C	0.70388	0.00039
		FIL 10-15-20I	0.70395	0.00039
		FIL 10-15-20R	0.70434	0.00039
		FIL 10-15-8- C	0.70429	0.00039
		Fil 10-15-8- R	0.70455	0.00039
FIL 10-15-41-C		0.70449	0.00039	
Fil 10-15-41-R		0.70435	0.00039	
FIL 10-15- 600 micron	0.70443	0.00039		
<b>FIL 10-6</b>	FIL 10-6-1-C	0.70438	0.00018	
	FIL 10-6-38-C1	0.70428	0.00018	
	Fil 10-6-38-R2	0.70429	0.00018	
	FIL 10-6-33-C	0.70422	0.00018	
	FIL 10-6-33-R	0.70411	0.00018	
	FIL 10-6-33-I	0.70416	0.00018	
	FIL 10-6-43-I	0.70417	0.00018	
	FIL 10-6-51	0.70455	0.00018	
	FIL 10-6-76-C	0.70435	0.00018	
	FIL 10-6-76-R	0.70433	0.00018	
	Fil 10-6-73-C	0.70408	0.00018	
	Fil 10-6-73-R	0.70399	0.00018	
	FIL 10-6-600 micron 1	0.70427	0.00018	

Table 9.Continued

		Sample	$^{87}\text{Sr}/^{86}\text{Sr}$	Uncertainty
<b>Group 2a</b>	<b>FIL 10-2</b>	FIL 10-2-27-I	0.70419	0.00039
		FIL 10-2-27-R	0.70415	0.00039
		FIL 10-2-27-C	0.70415	0.00039
		FIL 10-2-25-C	0.70412	0.00039
		FIL 10-2-25-R	0.70427	0.00039
		FIL 10-2-11-C	0.70422	0.00039
		FIL 10-2-11-R	0.70425	0.00039
		FIL 10-2-10-C	0.70414	0.00039
		FIL 10-2-10-R	0.70429	0.00039
		FIL 10-2- 600 micron1	0.70427	0.00039
		FIL 10-2-600 micron2	0.70417	0.00039
<b>Group 4</b>	<b>FIL 10-1</b>	FIL 10-1-6-R	0.70418	0.00009
		FIL 10-1-6-I	0.70407	0.00009
		FIL 10-1-9-C	0.70419	0.00009
		FIL 10-1-9-R	0.70423	0.00009
		FIL 10-1-20-C	0.70410	0.00009
		FIL 10-1-20-R	0.70418	0.00009
		FIL 10-1-24-C	0.70423	0.00009
		FIL 10-1-24-I	0.70420	0.00009
		FIL 10-1-24-R	0.70421	0.00009
		FIL 10-1-49-C	0.70446	0.00009
		FIL 10-1-49-I	0.70438	0.00009
		FIL 10-1-49-R	0.70429	0.00009
		FIL 10-1-600micron	0.70425	0.00009
		<b>FIL 10-3</b>	FIL 10-3-64-C	0.70447
	FIL 10-3-64-I		0.70420	0.00025
	FIL 10-3-64-R		0.70417	0.00025
	FIL 10-3-65-C		0.70422	0.00025
	FIL 10-3-65-I		0.70436	0.00025
	FIL 10-3-65-R		0.70430	0.00025
	FIL 10-3-66-C		0.70427	0.00025
	FIL 10-3-66-I		0.70416	0.00025
	FIL 10-3-66-R		0.70421	0.00025
	FIL 10-3-45-C		0.70419	0.00025
	FIL 10-3-45-R		0.70414	0.00025
	FIL 10-3-38-R		0.70418	0.00025
	FIL 10-3-36-C		0.70407	0.00025
	FIL 10-3-36-R		0.70417	0.00025
	FIL 10-3-28-C	0.70429	0.00025	
FIL 10-3-28-I	0.70440	0.00025		
FIL 10-3-28-R	0.70428	0.00025		
FIL 10-3-7-C	0.70368	0.00025		
FIL 10-3-7-R	0.70480	0.00025		
FIL 10-3-16-C	0.70431	0.00025		
FIL 10-3-16-I	0.70417	0.00025		
FIL 10-3-16-R	0.70413	0.00025		
FIL 10-3-600micron1	0.70422	0.00025		

Table 9. Continued

		<b>Sample</b>	<b><math>^{87}\text{Sr}/^{86}\text{Sr}</math></b>	<b>Uncertainty</b>
<b>Group 5</b>	<b>FIL 10-10</b>	FIL 10-10-17-R	0.70382	0.00017
		FIL 10-10-13-C	0.70382	0.00017
		FIL 10-10-13-R	0.70392	0.00017
		FIL 10-10-25-C	0.70386	0.00017
		FIL 10-10-25-R	0.70385	0.00017
		FIL 10-10-32- R	0.70382	0.00017
		Fil 10-10-32-R2	0.70400	0.00017
		FIL 10-10-29-C	0.70459	0.00017
		Fil 10-10-29-I	0.70441	0.00017
		Fil 10-10-29-R	0.70472	0.00017
		FIL 10-10-39-C	0.70388	0.00017
		FIL 10-10-39-R	0.70392	0.00017
		FIL 10-10-600micron 1	0.70477	0.00017
		FIL 10-10-600micron 2	0.70385	0.00017

<sup>1</sup> Inferred core values are indicated with a “C”.

<sup>2</sup> Areas between core and rim termed intermediate and indicated with an “I”.

<sup>3</sup> Inferred rim values are indicated with a “R”.

<sup>4</sup> Crystals with highly sieved core not suitable for analysis had a second rim value analyzed and are marked with a “R2”.

<sup>5</sup> Crystals analyzed as representative of smaller phenocrysts of sufficient size are indicated by “600 micron”.

### *Changes in Sr Isotopes and Sr Isotopes vs. Anorthite*

Changes in Sr isotopes (rim-core) are plotted on a bar graph for each crystal analyzed in order to determine which crystals show evidence of assimilation (positive values) or recharge (negative values) (Figure 36). Colors correspond to composition (i.e., rock name). Most samples are within the 2-sigma uncertainty and therefore display neither positive nor negative differences. The exceptions are samples Fil 10-15 of Group 2 and Fil 10-3 of Group 4, which show both negative and positive values outside of uncertainty.

Figure 37 shows  $^{87}\text{Sr}/^{86}\text{Sr}$  for core/rim/intermediate values plotted against An cores/rims/intermediate values for all crystals. Generally basalts and basalt-basaltic andesite plagioclase cores have the highest An values and show the most restricted range in Sr isotope values from 0.70395-0.70435. Conversely, basaltic andesite and andesite plagioclase cores have the lowest An values and have a slightly less restricted Sr isotope range from 0.70368-0.70459. However, a large amount of overlap occurs when examining rims and intermediates in both An contents and isotope ratios. There is a lack of any systematic relationship between Groups.

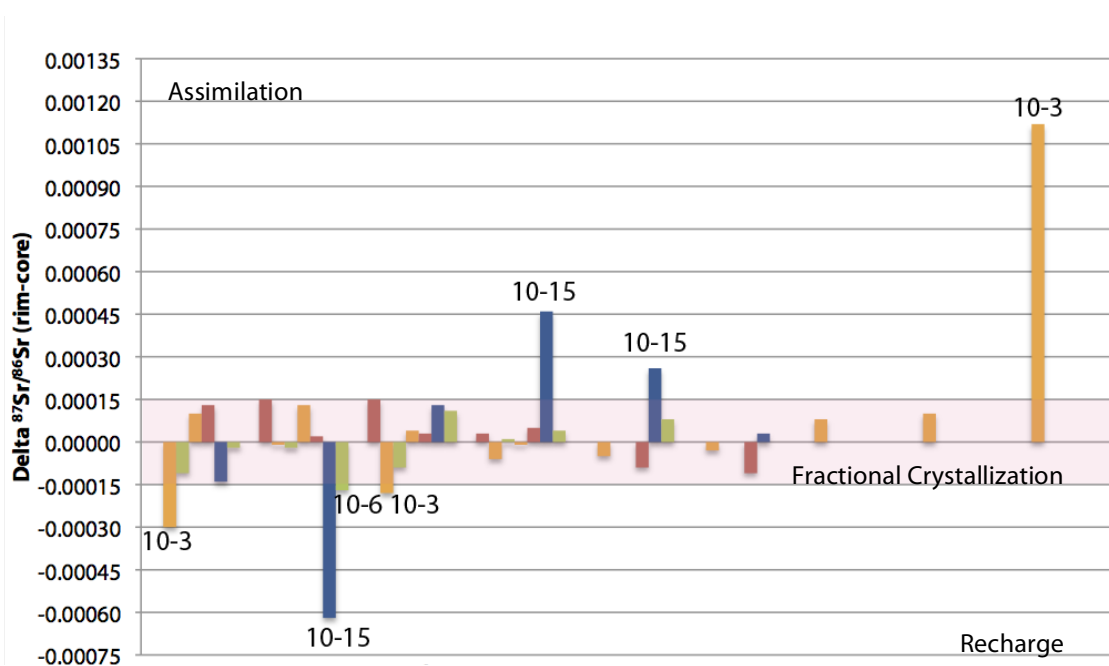


Figure 36: Delta (rim-core)  $^{87}\text{Sr}/^{86}\text{Sr}$  values plotted on a bar graph for samples from Groups 2, 4, and 5. Colors represent composition, similar to Figure 33 (See Table 7). The 2-sigma error range is highlighted with a pink box. Only three samples show values outside of error. Positive values are interpreted as evidence for assimilation, while negative values are interpreted as evidence for recharge.

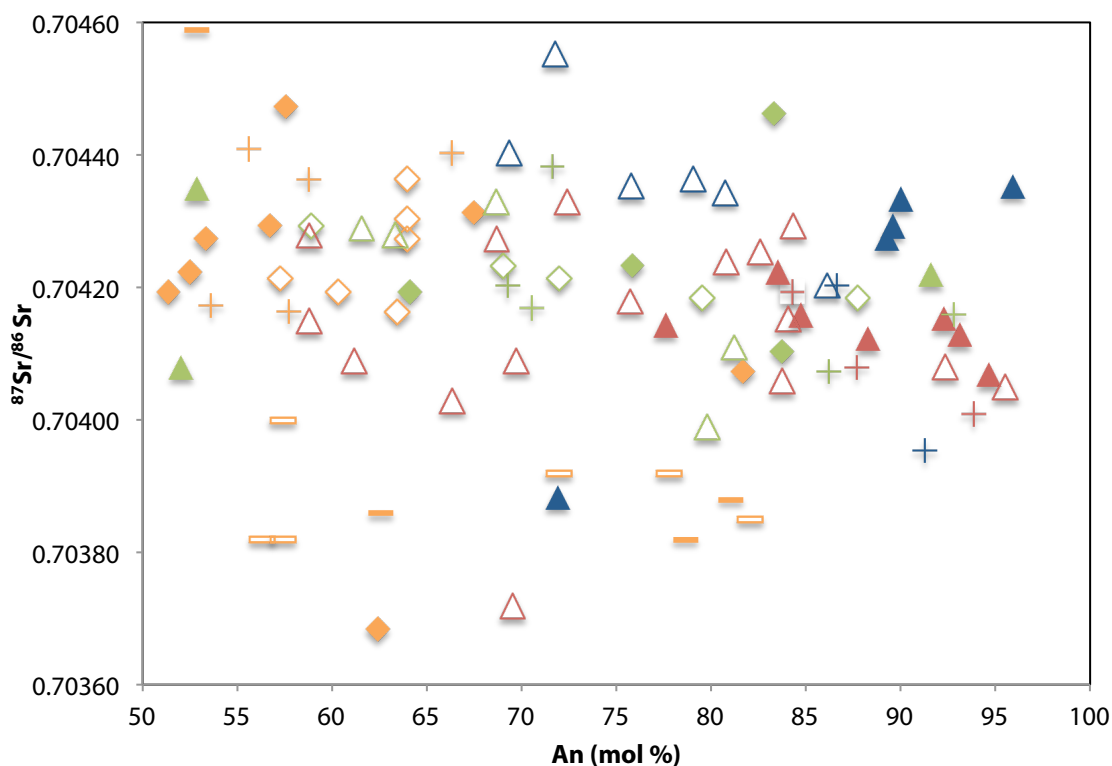


Figure 37: Plagioclase *in situ*  $^{87}\text{Sr}/^{86}\text{Sr}$  values plotted against An (mol %) for cores (filled symbols), rims (unfilled symbols), and intermediates (crosses). Symbols correspond to groups while colors correspond to composition (See Table 7).

### MELTS Models

Filicudi's whole rock data were compared to the results of 15 MELTS models to determine the best-fit model runs. Simulations were run using Fil 12 from Santo (2000) as the parental magma composition and parameters listed in the Methods chapter. Two simulations were chosen that best bracket Filicudi's whole rock data (Figure 38). The results document fractional crystallization began between 1183-1188°C during polybaric ascent from 2-4 kb and continued to the surface.

MELTS results indicate the magma within a deeper part of the magma system had an initial H<sub>2</sub>O content of between 3-4.5 wt. %, and Mg-rich cpx, ol, and magnetites were fractionating. In the shallower part of the system (0.5-1.2 kilobars) high An plagioclase (An<sub>89-90</sub>) and water fractionated. At lower pressures (0.6 kbar) orthopyroxene came on the liquidus. Amphibole was not a fractionating phase, but this is not unexpected (M. Ghiorso, pers. communication, 2012).

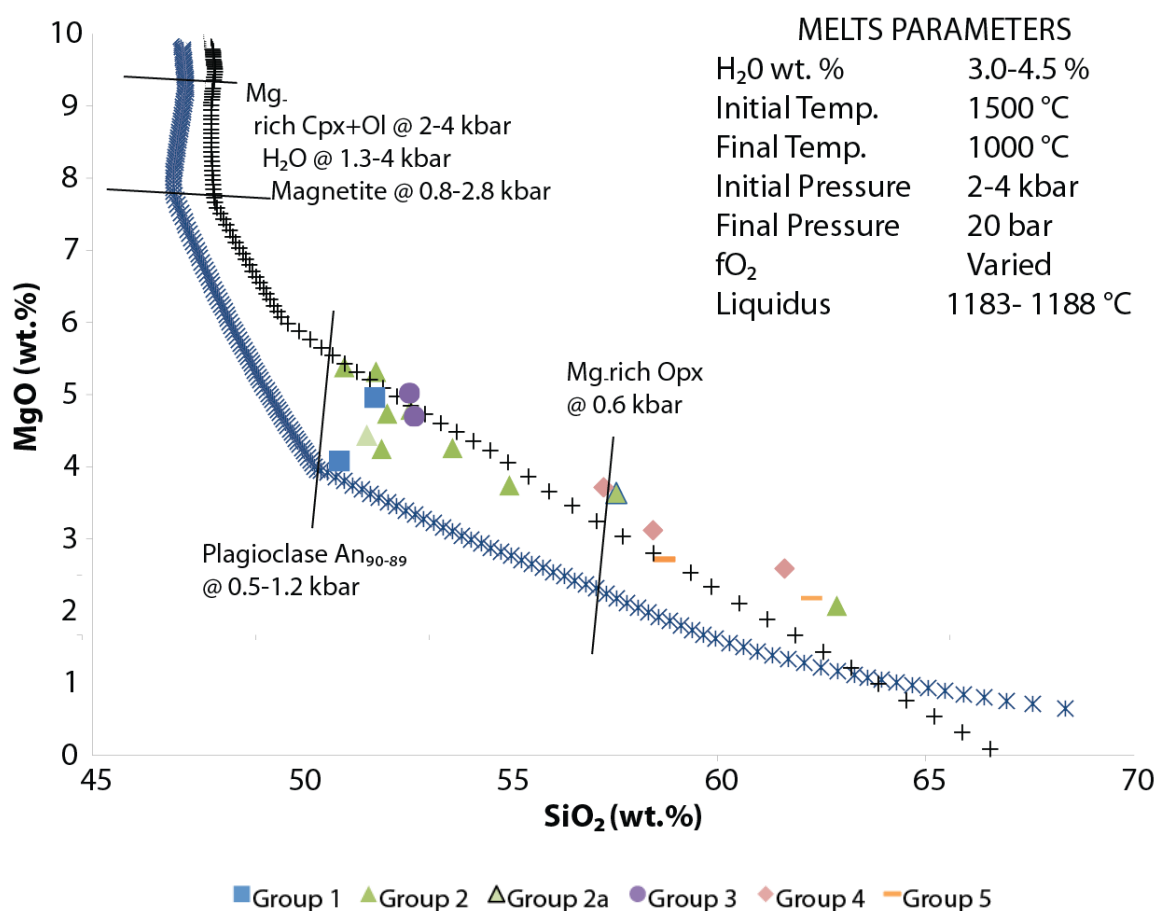


Figure 38: MgO (wt%) plotted against SiO<sub>2</sub> (wt. %) for the polybaric best-fit MELTS runs 12 and 15 and Filicudi whole rock data. Symbols are the same as in Figure 3. MELTS parameters are listed in the top right corner. Initial H<sub>2</sub>O and pressures are indicated for each run. Mineral fractionation is indicated with a line.

## CHAPTER V

### DISCUSSION

#### Overview

Together, MELTS modeling, whole rock data and *in situ* plagioclase data document the magmatic processes impacting Filicudi Island and provide insight into the magma chamber structure. Results not only augment existing magma chamber models (Santo, 2000, Santo *et al.*, 2004), but also elucidate a time-integrated view of Filicudi's magma evolution.

Table 10 presents the roles that recharge and fractional crystallization played in the Filicudi magmatic system by highlighting my interpretations and detailing supporting data. Results support previous interpretations of the magmatic system beneath Filicudi being polybaric (Santo, 2000, Santo *et al.*, 2004). Crystallization occurred over range of pressures. In the deeper part of the system, water-rich magma began fractionating cpx+ol+sp at ~ 3.5-4 kilobars. At this depth, crystallization of plagioclase was suppressed. In a shallower part of the magmatic system, H<sub>2</sub>O+cpx+ol+sp+plag+opx were on the liquidus at ~0.5-1.2 kilobars (Figure 38). Examination of whole rock major and trace elements support fractional crystallization as a dominant process in the formation of the magmas at Filicudi. However, in contrast to previous whole rock investigations (Francalanci & Santo, 1993, Santo, 2000, Santo *et al.*, 2004), results from *in situ* plagioclase textural, compositional and Sr isotopic data indicate complex occurrences of recharge also played a dynamic role. Below, I present a brief overview of the stratigraphic controversies that exist on Filicudi, elucidate the stratigraphic nomenclature



I have adopted, and provide a discussion of the different RAFC processes that affected the magma systems at Filicudi Island. Then, using the relative stratigraphy of Tranne *et al.* (2000) and data presented here, I propose an evolutionary magma chamber model for Filicudi Island.

Table 10. Summary of interpretations and evidence for magmatic processes for Groups 2, 4, and 5.

Pressure range	Interpretation	Method	Evidence
2-4 kilobars	Fractional crystallization of Fe-Mg phases	MELTS	Ol+Cpx+Sp fractionating with an initial H <sub>2</sub> O content of 3-4.5 wt. %
	Plagioclase suppression	<i>In situ</i> plagioclase trace elements	Normally zoned, high An plagioclase in andesites have higher Sr concentrations than normally zoned, high An plagioclase within basalts
0.5-1.2 kilobars	Fractional crystallization	MELTS	Presence of high An plagioclase and opx fractionating
		<i>In situ</i> plagioclase major elements	Formation of high An (~95 mol %) plagioclase with normal zoning and low An (~55 mol %) plagioclase
	Rapid formation of plagioclase	<i>In situ</i> plagioclase major and trace elements	Few variations in major and trace elements across crystal profiles
		Plagioclase textures	Abundance of large unzoned/monotonous plagioclase
	Recharge from the deeper part of the system	<i>In situ</i> plagioclase trace elements	Low An crystals show core to rim increases in Fe
		<i>In situ</i> plagioclase major elements	Low An crystals are reversely zoned (high An rims)
	Plexus of sills and dikes	<i>In situ</i> plagioclase <sup>87</sup> Sr/ <sup>86</sup> Sr	Few variations across profile and unsystematic differences within-sample in <sup>87</sup> Sr/ <sup>86</sup> Sr

## Stratigraphy

In contrast to four eruptive cycles based on stratigraphic and radiometric dating proposed by Santo (2000), six are identified using the stratigraphic relationships documented by the geologic map of Tranne *et al.* (2000). Furthermore, differences in radiometric ages have been documented for the Punta Dello Zucco Grande Formation (Table 1, Figure 2). This formation was once interpreted as the oldest subaerial eruptive product in all of the Aeolians (Francalanci & Santo, 1993, Santo, 2000, Santo *et al.*, 2004, Santo *et al.*, 1995).  $^{40}\text{Ar}/^{39}\text{Ar}$  dating performed by Santo *et al.* (1995) yielded an age of  $1020 \pm 20$  ka, and therefore multiple authors utilized this age constraint in their stratigraphic investigations (Francalanci & Santo, 1993, Santo, 2000, Santo *et al.*, 2004, Santo *et al.*, 1995). Other investigations using unspiked K/Ar (De Rosa *et al.*, 2003) and  $^{40}\text{Ar}/^{39}\text{Ar}$  (Creamer *et al.*, 2011) dating techniques, instead, indicate this formation to be closer to 200 ka (Table 1). The discussion presented below relies upon the stratigraphy of Tranne *et al.* (2000) and utilizes the age constraints of  $192.1 \pm 2.2$  (Creamer *et al.*, 2011) for this eruptive unit.

## Magma Chamber Processes

### *Documentation of Fractional Crystallization in Deeper Part of the Magmatic System*

Fractional crystallization (FC) played a vital role in the magmatic system at Filicudi Island. MELTS models run using the parameters outlined in the Methods chapter revealed that olivine and cpx came onto the liquidus at a temperature of 1,188 °C and pressures of 2-4 kilobars, with magnetite fractionating soon after at 0.8-2.8 kilobars and 1127°C. At these pressures, the initial H<sub>2</sub>O content of 3-4.5 wt.% suppressed plagioclase

crystallization, thereby supporting the formation of high calcium and aluminum MELTS. Fractional crystallization at these pressures, in the deeper part of the magmatic system, yielded approximately 2-3 wt. % olivine, 50 wt. % cpx, and 2-3 wt. % spinel solids prior to plagioclase coming on the liquidus. It was not until the magma within the deeper system was able to ascend to shallower pressures that water saturated and plagioclase was able to crystallize (discussed in next section).

Documentation of cpx stability at higher pressures supports findings from Nazzarini *et al.* (2001) who used cpx cell and M1 site volumes to interpret pressures of crystallization. Nazzarini *et al.* (2001) indicate cpx from Filicudi Island had similar cell and M1 site volumes as those documented in high pressure ultramafic xenoliths- (spinel ilherzolite) (Malgarotto *et al.*, 1993, Nazzareni *et al.*, 2001).

The absence of plagioclase as a crystallizing phase in the deeper part of the magmatic system is indicated by *in situ* plagioclase average Sr concentrations within andesitic plagioclase crystals, which are higher than average Sr concentrations within basaltic plagioclase crystals (~1800 ppm compared to 1200 ppm) (Figure 33d). This result implies that the andesitic melt from which the plagioclase grew had experienced fractionation without plagioclase on the liquidus, causing Sr to remain incompatible within the melt. Because the basaltic magma underwent less fractional crystallization in the deeper system than andesitic magma, it had less Sr available to it prior to onset of plagioclase crystallization.

Although not stable in the MELTS runs, whole rock MREE patterns suggest that amphibole was a crystallizing phase in the deeper part of the system. Convex up patterns

seen in whole rock MREE (Figure 39) as well as shallow linear trends seen in La/Yb and Dy/Yb plotted against whole rock SiO<sub>2</sub> indicate that amphibole may have been on the liquidus (Figure 40). Furthermore, experimental studies of amphibole stability at water-rich subduction zone volcanoes indicate that amphibole begins to breakdown once it reaches pressures of 1.6-2.6 kbars (Rutherford & Hill, 1993). These findings indicate the crystallization of amphibole most likely occurred prior to plagioclase crystallization at 0.5-1.2 kbars.

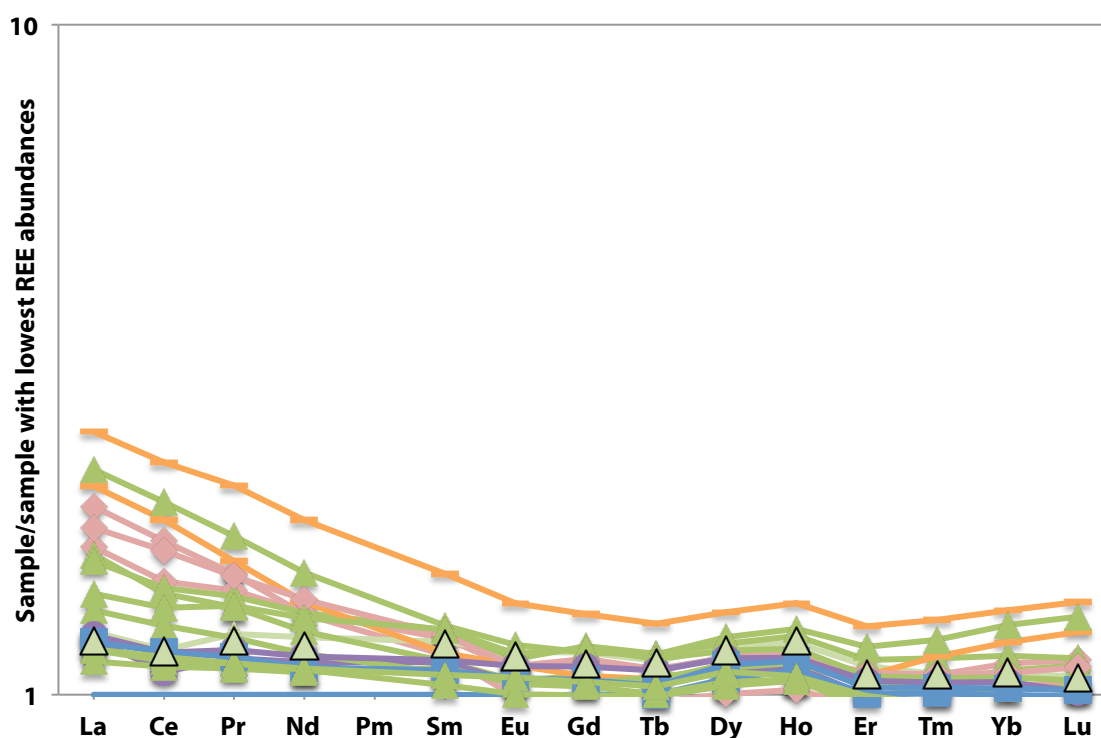


Figure 39: Whole rock REE divided by their lowest values. The concave up anomaly in the MREE suggests amphibole fractionation (Davidson *et al.*, 2007).

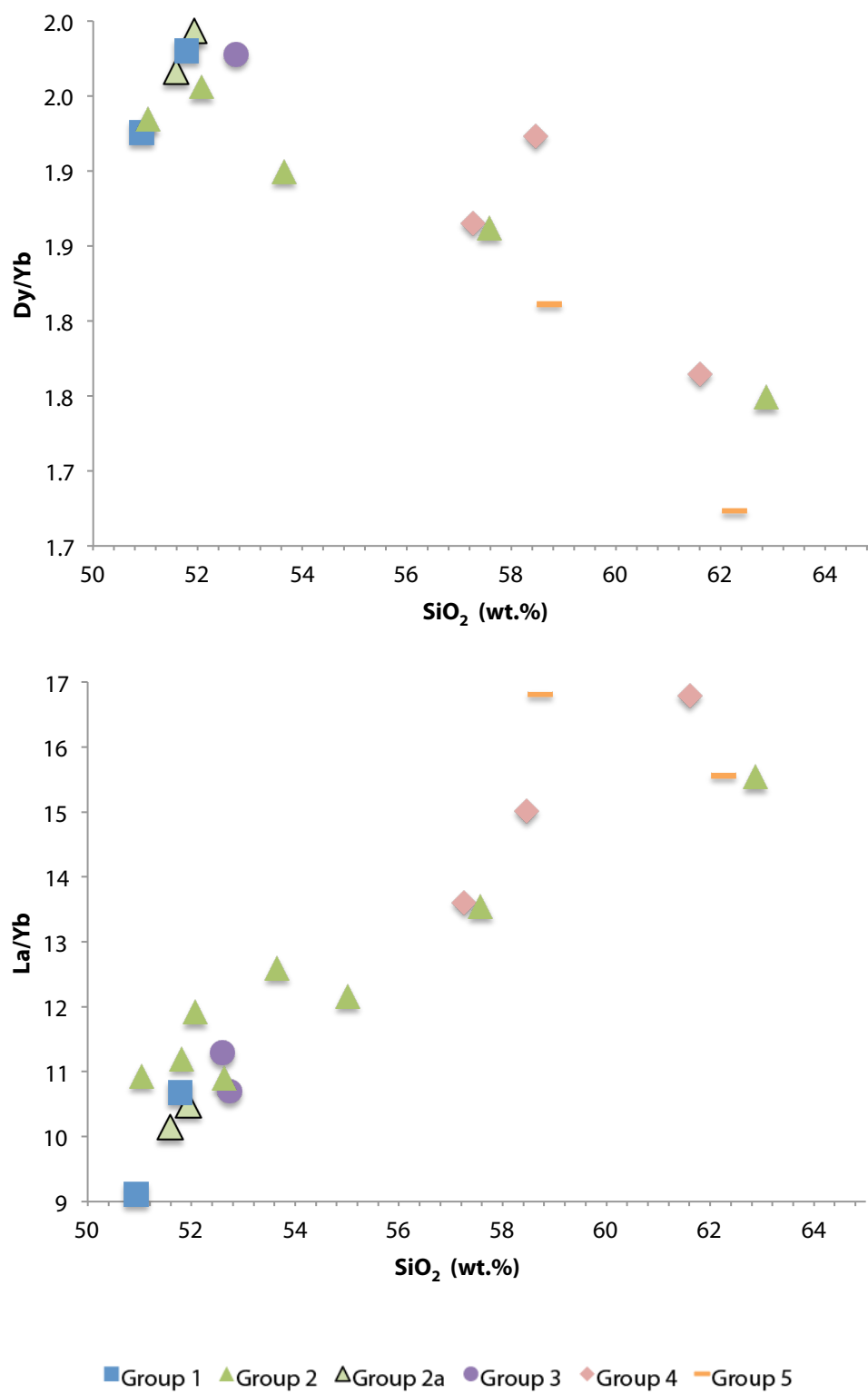


Figure 40: Rare Earth Elements Dy/Yb and La/Yb plotted against whole rock  $\text{SiO}_2$ . Decreasing Dy/Yb with increasing whole rock  $\text{SiO}_2$  suggests amphibole fractionation (Davidson *et al.*, 2007).

*Documentation of Fractional Crystallization in the Shallower Part of the Magmatic System*

Fractional crystallization at shallower depths is documented with MELTS results, plagioclase textures, and whole rock and *in situ* plagioclase data. MELTS models are consistent with differentiated melt from the deeper part of the system ascending to pressures of 0.5-1.2 kilobars. At these pressures, melt has 49.7-50.5 wt. % SiO<sub>2</sub> and was at temperatures between 1049-1107° C (Figure 38). The water saturated melt potentially devolatilized, which allowed plagioclase to crystallize with an initial An of between 89-90 mol%. Fractional crystallization continued and orthopyroxene came onto the liquidus at 0.6 kilobars and 1020° C. Because whole rock compositions collected on Filicudi Island range from 50.93-62.87 wt.% SiO<sub>2</sub>, whole rock trace elements are likely dominated by fractional crystallization that occurred within the upper part of the system, and after plagioclase formation (Figures 5-7).

Plagioclase textures, coupled with *in situ* major element data provide additional insight into the crystallization history. Most zoned crystals documented in Filicudi samples are normally zoned, with delta An (rim-core) of 0 to -45 mol % (Figure 31). Crystals are also characterized by an abundance of core An contents of 82 to 97 mol %. The abundance of normally zoned to unzoned crystals, combined with an abundance of monotonous textures, is consistent with fractional crystallization as the dominant mechanism of melt evolution. The abundance of large (~2.5 mm) monotonously zoned plagioclase crystals revealed by Nomarski images potentially indicate relatively fast

growth in a magma system in which diffusivity of critical elements was faster than the crystal growth rate (Pearce, 1994, Streck, 2008).

*In situ* plagioclase trace elements, with the exception of Sr discussed above, provide support for continued fractional crystallization after plagioclase came on the liquidus. As anorthite values in normally zoned plagioclase decrease with increasing whole rock silica content, the minimum Mg and Fe compatible trace element values decrease slightly, while incompatible trace elements Ba and La are generally more abundant in andesites compared to more mafic rocks (Figure 34).

Consistent with fractional crystallization as the dominant magma chamber process when plagioclase was forming, most within-crystal *in situ*  $^{87}\text{Sr}/^{86}\text{Sr}$  are homogeneous within uncertainty (Figure 36). This observation indicates that individual crystals grew in an isotopically homogeneous environment. The few exceptions (crystals with core to rim decreases in Sr isotopes outside of uncertainty) reflect crystal growth in an environment that was isotopically heterogeneous on the scale of a plagioclase crystal. In addition, crystals within a single sample have Sr isotope signatures that are heterogeneous (Figure 35), suggesting that MELTS with different Sr isotope characteristics were available to form crystals that erupted in a distinct volcanic product. The diversity of whole rock Sr isotope values in basalts (0.70430 to 0.70480) and andesites (0.70430 to 0.70450) (Figure 35) supports the suggestion that there was a mechanism that introduced Sr isotope variability into the magmatic system associated with Filicudi. Possible explanations for this heterogeneity is preservation of MELTS that acquired distinct Sr isotope signatures

from the mantle or incomplete homogenization of assimilants from wall rock. Additional work is required to further elucidate the origin of the Sr isotope variability at Filicudi.

*Evidence for Magma Recharge and Magma Mixing in Shallower Part of Magmatic System*

Recharge within the shallower part of the magma system is indicated by the occurrence of a population of plagioclase crystals that display different textural zoning, and reverse zoning with respect to *in situ* major and trace element data (Figures 21 and 34). Because the reversely zoned plagioclase is documented within two separate eruptive Groups, results suggest at least two recharge events occurred.

The reversely zoned plagioclase crystals have highly sieved cores that have been in filled with other minerals or glass and have euhedral rims (textural type # 3). Because experimental results indicate high-An plagioclase reacts little to the introduction of low-An melt (Tsuchiyama, 1985), the core textural dissolution was likely caused by the introduction of a high-Ca magma or a change in parameters such as pressure or temperature. Likewise, *in situ* major elements document the crystals to be reversely zoned with core anorthite values of between 43-53 mol % and rim anorthite values of 75-95 mol % (Figure 34). As the rim An values closely match those of normally zoned core values, interpreted to be formed from fractional crystallization, the source of recharge was likely magma from the deeper, plagioclase-suppressed part of the magma system.

Additionally, the crystal population that shows reverse An zoning also shows reversely zoned trace element trends, with the exception of Sr. As reversely zoned



plagioclase An values increase from core to rim, compatible trace elements Mg and Fe also increase, while incompatible trace elements Ba and La decrease, albeit slightly (Figure 34). These findings imply the rims grew after a recharge and magma-mixing event; the likely source of mafic magma was from the deeper part of the system.

### Magma Chamber Structure and Evolution

MELTS modeling coupled with investigations of *in situ* plagioclase textural, compositional, and isotopic data permit the development of a hypothesis about the magma chamber structure. By integrating the magma chamber structure with the stratigraphy adopted for this study (Tranne *et al.* (2000) Groups 2, 4, and 5), a general time-integrated view of Filicudi's magmatic evolution is documented and schematically illustrated in Figure 41. It is recognized that such a view is incomplete because samples from all Groups have not been studied in detail.

#### *Group 2- Fossa Felici*

MELTS results indicate that fractional crystallization of Mg-rich cpx+ol+sp occurred in a deeper (2-4 kbar), water-rich part of the Filicudi system while crystallization of plagioclase was suppressed. Whole rock REE element abundances indicate amphibole could have also been on the liquidus at these depths. Differentiation without plagioclase fractionation produced MELTS of slightly different SiO<sub>2</sub> abundances. More mafic MELTS were characterized by higher Mg and Fe concentrations, while those that were slightly less mafic had higher Ba, Sr, and La.

Results suggest the intrusion into the upper system that produced Group 2 was of the most mafic magmas. The upper chamber structure was most likely a plexus of sills and dikes in order to account for the within and between sample isotopic heterogeneities seen with *in situ* plagioclase  $^{87}\text{Sr}/^{86}\text{Sr}$  data. At lower pressure, water within melt potentially devolatilized, and plagioclase was able to crystallize relatively rapidly, forming texturally monotonous or unzoned cores with high values of FeO (0.6-1.0 wt. %) and An (90-98 mol %).

Whole rock compositions of Group 2 samples span a range from basalt to basaltic andesite (51.0-57.7 wt.%  $\text{SiO}_2$ ). Continued fractional crystallization of Group 2 magmas within the shallow part of the system likely produced this  $\text{SiO}_2$  range and is indicated by rims of plagioclase crystals with lesser average amounts of Mg and FeO, lower An, and greater amounts of Ba and La (Figure 33).

*In situ* major and trace elements reveal continued fractional crystallization of Group 2 magmas also produced new plagioclase cores with relatively low values of FeO (0.3-0.4 wt. %) and An (50-55 mol%). *In situ* trace element results indicate that following formation of this new plagioclase, recharge of magma of the same composition as the most mafic magmas from the deeper part of the system intruded into the upper complex. The recharged magma mixed with existing magma and created another population of plagioclase with higher values of FeO (0.5-0.9 wt. %) and An (75-85 mol %), albeit not as high as the initial values. The recharged magma also reacted with the low An (50-55 mol %) cores and produced reversely zoned rims.

Sr concentrations (900-1300 ppm) within the plagioclase formed from the recharged magma were approximately the same as the concentrations within the preexisting plagioclase (900-1500 ppm) (Figure 34d). This potentially suggests that the recharged magma had slightly higher Sr concentrations than the initial Group 2 intrusion. The resulting mixed-magma erupted with a whole rock basaltic andesite composition.

#### *Group 4- Capo Graziano*

Results suggest the magmatic plumbing system and associated processes were similar for Group 4 as they were for Group 2. As Sr concentrations (1500-1900 ppm) within plagioclase growing from the initial intruded magma of Group 4 were higher than those in plagioclase (900-1300 ppm) (Figure 34d) from the initial intruded magma of Group 2, the Group 4 intrusion from the deeper, water-rich part of the system was likely of a more felsic composition than that of the Group 2 intrusion. Likewise, plagioclase cores that formed relatively rapidly upon intrusion and possible devolatilization in the shallower part of the system had lower values of An (75-90 mol %) and FeO (0.5-0.6 wt. %), than those that formed in the initial Group 2 intrusion (Figure 34). Moreover, erupted products from Group 4 samples span a compositional range from basaltic andesites to andesites (57.26- 61.61 wt.% SiO<sub>2</sub>).

Differentiation proceeded within the upper part of the system, and the rims of the plagioclase crystals grew with lesser amounts of Mg, FeO, lower An, and greater amounts of Ba and La (Figure 34). Similar to Group 2, new plagioclase cores formed with lower concentrations of FeO (0.3-0.4 wt. %) and An (50-60 mol %) (Figure 34c) and

a recharge event from the deeper part of the system is documented by reversely zoned plagioclase and a new population of higher An (65-85 mol %) crystal cores. Unlike the Group 2 evolution, the recharged magma produced plagioclase containing higher amount of Sr (1500-2300 ppm) than the initial intruded magma plagioclase (1500-1900 ppm), possibly indicating that the batch of recharged magma was more Sr rich than the initial intrusion in Group 4 (Figure 34d). The resulting mixed magma erupted with an andesitic whole rock composition.

#### *Group 5- Monte Montagnola*

Group 5 marks the end of Filicudi's active volcanism to date. Results imply the structure of the polybaric system remained the same as in Group 4, but some processes changed. The whole rock composition erupted is only of an andesite composition (62.26 wt. % SiO<sub>2</sub>). Since Sr concentrations with plagioclase were higher than either Group 2 or Group 4 plagioclase (1400-2400 ppm), the magma being intruded from the deep system into the shallow system was most likely evolving through time to a more silicic composition. Moreover, the relatively rapid plagioclase growth upon intrusion into the shallow system produced core crystals with lower An (65-90 mol %) and FeO (0.4-0.5 wt. %) values (Figure 34c). Differentiation within the shallow system continued, leaving plagioclase normally zoned in both An and trace elements. However, unlike Groups 2 and 4, evidence of a recharge event from the deeper system is not documented within Group 5 products. The resulting magma was erupted as an andesite (Figure 41).

Consistent with the observation that no volcanism has occurred since the eruption of the Group 5 products, there is no evidence that the deeper system was experiencing recharge from a mantle source. Perhaps the increasingly felsic nature of the magma within the deeper system had too high of a viscosity and stalled within the crust.

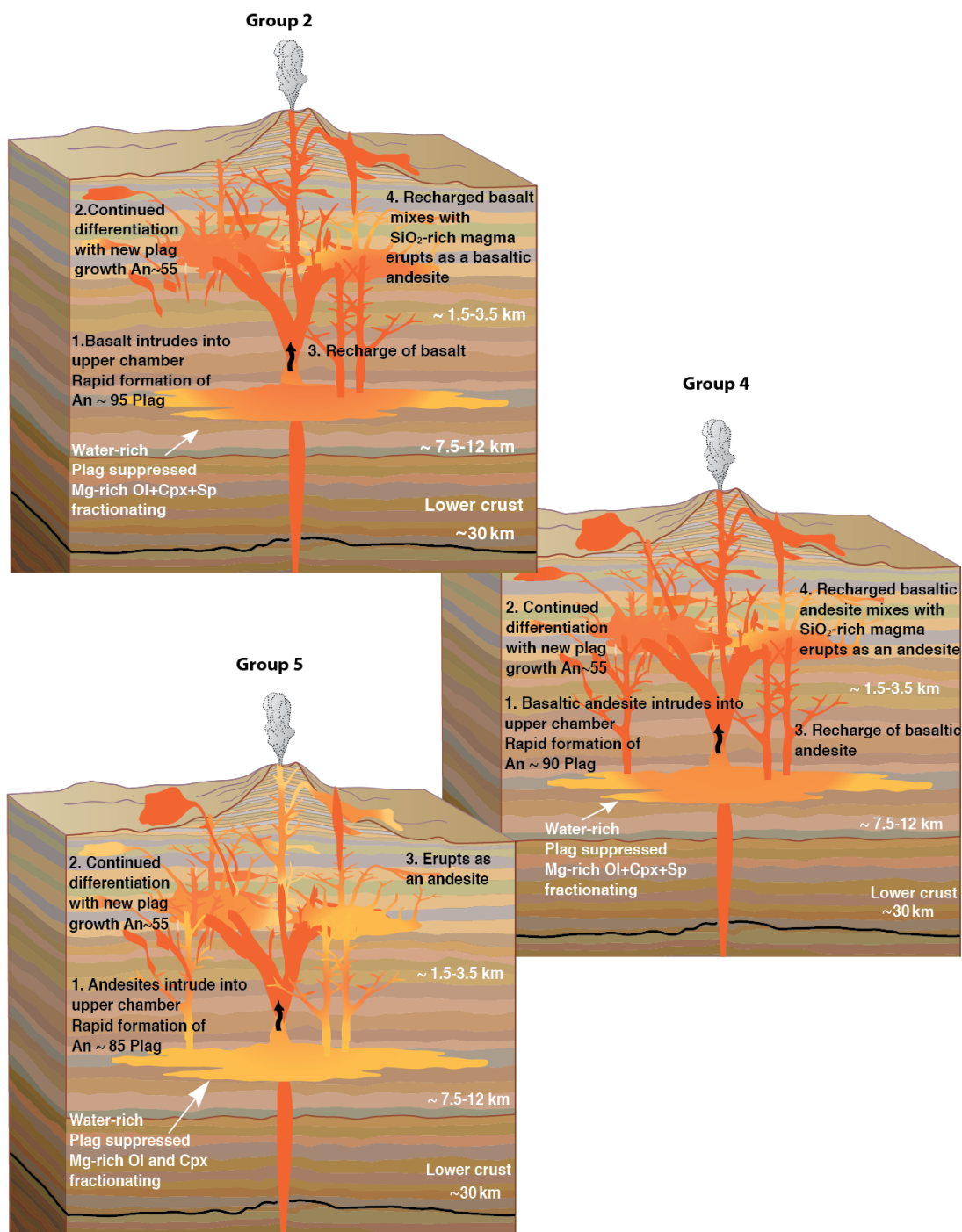


Figure 41: Schematic illustrations of the polybaric magma plumbing system beneath Filicudi Island associated with Groups 2, 4, and 5. During eruptions of Group 2 rocks, only basalts intruded from the lower system into the upper system. After the eruption of Group 5 rocks, volcanic activity on Filicudi Island ceased.

## CHAPTER VI

### CONCLUSIONS

My study (to my knowledge) is the first to integrate MELTS modeling, whole rock compositional and isotopic data, and plagioclase textural, *in situ* compositional and Sr isotopic data to document magmatic processes on Filicudi Island, Italy. Results document the relative chronology and roles that fractional crystallization and recharge played in the magmatic evolution of Filicudi Island, as well as reveal the polybaric dynamics of the magma chamber and provide information about the relative timing of differentiation vs. plagioclase crystallization.

The magmatic system beneath Filicudi was found to be polybaric. Within the deeper system at 3.5-4 kilobars, fractional crystallization played a dominant role in magmatic differentiation, while high water contents (3-4.5 wt.% H<sub>2</sub>O) acted to suppress plagioclase crystallization. Olivine and clinopyroxene came onto the liquidus at pressures of 2-4 kilobars, with magnetite beginning to fractionate at 0.8-2.8 kilobars. Differentiation within the deeper system acted to produce regions of more mafic MELTS high in Mg, Fe, and Al and more felsic MELTS high in Ba, Sr, and La.

The shallow system at 0.5-1.2 kilobars was a plexus of sills and dikes that was repeatedly recharged from the deeper system throughout most of the island's magmatic evolution. Initial intrusions were of the most mafic compositions, and upon ascent, the magma devolatilized allowing plagioclase to crystallize relatively rapidly from a melt that produced An-rich (90-98 mol %), Fe-rich (0.6-1.0 wt. %), and Sr-depleted (900-1300 ppm) plagioclase. Continued fractional crystallization formed new populations of

plagioclase with lower An (50-55 mol%) and Fe (0.3-0.4 wt. %) contents, while recharge events from the deeper system caused the new populations to become reversely zoned.

As the magmatic evolution proceeded, intrusions from the deeper chamber became progressively more felsic suggesting continued FC processes within the deeper system. Plagioclase crystals that formed rapidly upon ascent into the shallower system were not as An-rich (75-90 mol %), and as FeO levels decreased (0.5-0.6 wt. %), Sr contents increased (1500-1900 ppm). Fractional crystallization within the shallower system continued to yield lower An (50-60 mol %) and FeO (0.3-0.4 wt. %) cores and the newly formed cores continued to become reversely zoned due to recharge events.

During the last stage of volcanism recorded thus far at Filicudi Island, intrusions from the deeper system were more differentiated. Rapidly formed plagioclase had high An (65-90 mol %), low FeO (0.4-0.5 wt. %), and the highest Sr concentrations documented (1400-2400 ppm). Fractional crystallization continued long enough to produce normally zoned rims prior to eruption, and then volcanism ceased (to date). If another recharge event occurred, it was not documented by samples studied in this work.

This study shows that the integration of MELTS models, with whole rock and plagioclase *in situ* compositional and isotopic data provides an excellent tool by which to document the processes and chronological order of processes that affected a volcano's magmatic evolution. In contrast to previous whole rock investigations (Francalanci & Santo, 1993, Santo, 2000, Santo *et al.*, 2004) results from this study indicate repeated occurrences of recharge played a dynamic role in the magmatic evolution on Filicudi Island and may have been a triggering mechanism for the individual eruption cycles.



### Future Work

Suppression of plagioclase crystallization within the deeper system of the polybaric chamber documented at Filicudi Island does not allow plagioclase to be used to document processes that occurred there. Investigations of *in situ* compositional and isotopic data of clinopyroxene would provide a more complete deep magma system process history. Moreover, examinations of melt inclusions, which have been observed within pyroxenes, would not only provide insights into potential parental magma composition(s) within the deep system, but would also allow for documentation of the volatile contents.

Additional sample collection and microsampling, particularly of < 600  $\mu\text{m}$  plagioclase, would also afford a more comprehensive view of the roles that mantle source heterogeneity vs. crustal contamination had in generating Sr isotope heterogeneity.

## REFERENCES

- Barberi, F., Innocenti, F., Ferrara, G., Keller, J. & Villari, L. (1974). Evolution of Eolian arc volcanism (southern Tyrrhenian Sea). *Earth and Planetary Science Letters* **21**, 269-276.
- Clynne, M. A. (1999). A Complex Magma Mixing Origin for Rocks Erupted in 1915, Lassen Peak, California. *Journal of Petrology* **40**, 105-132.
- Creamer, J. B., Calvert, A. T. & Spera, F. J. (2011). New  $^{40}\text{Ar}/^{39}\text{Ar}$  eruption ages for the western Aeolian Arc, Southern Italy. *Fall Meeting AGU*. San Francisco, CA.
- Davidson, J. P., Hora, J. M., Garrison, J. M. & Dungan, M. A. (2005). Crustal forensics in arc magmas. *Journal of Volcanology and Geothermal Research* **140**, 157-170.
- Davidson, J. P., Morgan, D. J. & Charlier, B. L. A. (2007a). Isotopic Microsampling of Magmatic Rocks. *ELEMENTS* **3**, 253-259.
- Davidson, J. P., Morgan, D. J., Charlier, B. L. A., Harlou, R. & Hora, J. M. (2007b). Microsampling and isotopic analysis of igneous rocks: Implications for the study of magmatic systems. *Annual Review of Earth and Planetary Sciences* **35**, 273.
- De Rosa, R., Guillou, H., Mazzuoli, R. & Ventura, G. (2003). New unspiked K-Ar ages of volcanic rocks of the central and western sector of the Aeolian Islands: reconstruction of the volcanic stages. *Journal of Volcanology and Geothermal Research* **120**, 161-178.
- Francalanci, L. & Santo, A. P. (1993). Magmatological evolution of Filicudi volcanoes, Aeolian Islands, Italy: constraints from mineralogical, geochemical and isotopic data. *Acta Vulcanol* **3**, 203-227.
- Ghiorso, M. S. (1997). Thermodynamic models of igneous processes *Annual Review of Earth and Planetary Sciences* **25**, 221-241.
- Ghiorso, M. S. & Sack, R. O. (1995). Chemical mass transfer in magmatic processes IV. A revised and internally consistent thermodynamic model for the interpolation and extrapolation of liquid-solid equilibria in magmatic systems at elevated temperatures and pressures. *Contributions to Mineralogy and Petrology* **119**, 197-212.
- Ginibre, C., Worner, G. & Kronz, A. (2002). Minor-and trace-element zoning in plagioclase: implications for magma chamber processes at Parinacota volcano, northern Chile. *Contributions to Mineralogy and Petrology* **143**, 300-315.

- Ginibre, C., Worner, G. & Kronz, A. (2007). Crystal Zoning as an Archive for Magma Evolution. *ELEMENTS* **3**, 261-266.
- Hildreth, W. & Moorbath, S. (1988). Crustal contributions to arc magmatism in the Andes of central Chile. *Contributions to Mineralogy and Petrology* **98**, 455-489.
- Humphreys, M. C. S., Blundy, J. D. & Sparks, R. S. J. (2006). Magma evolution and open-system processes at Shiveluch Volcano: Insights from phenocryst zoning. *Journal of Petrology* **47**, 2303-2334.
- Johnson, D., Hooper, P. & Conrey, R. (1999). XRF analysis of rocks and minerals for major and trace elements on a single low dilution Li-tetraborate fused bead. *Advances in X-ray Analysis* **41**, 843-867.
- Knaack, C., Cornelius, S. & Hooper, P. (1994). Trace element analyses of rocks and minerals by ICP-MS. *Open File Report. Department of Geology, Washington State University, Pullman, USA*.
- Lang, W. (1969). Nomarski differential interference-contrast microscopy. *ZEISS INFORMATION--OBERKOCHEN--* **16**, 114-120.
- Malgarotto, C., Molin, G. & Zanazzi, P. F. (1993). Crystal chemistry of clinopyroxenes from Filicudi and Salina (Aeolian Islands, Italy). Geothermometry and barometry. *European journal of mineralogy* **5**, 915-923.
- Manetti, P., Pasquar, G. & Tsegaye, A. (1995). A new geovolcanological map of Filicudi Island (Aeolian Arc, Italy). *Acta Vulcanologica* **7**, 1-5.
- Morelli, C., Giese, P., Cassinis, R., Colombi, B., Guerra, I., Luongo, G., Scarascia, S. & Schutte, K. (1975). Crustal structure of Southern Italy. A seismic refraction profile between Puglia-Calabria-Sicily. *Boll. Geofis. Teor. Appl* **18**, 183-210.
- Nazzareni, S., Molin, G., Peccerillo, A. & Zanazzi, P. (2001). Volcanological implications of crystal-chemical variations in clinopyroxenes from the Aeolian Arc, Southern Tyrrhenian Sea (Italy). *Bulletin of Volcanology* **63**, 73-82.
- Pearce, T. (1994). Recent work on oscillatory zoning in plagioclase. *NATO ASI Series C Mathematical and Physical Sciences-Advanced Study Institute* **421**, 313-350.
- Ramos, F. C. & Tepley, F. J. (2008). Inter-and intracrystalline isotopic disequilibria: techniques and applications. *Reviews in Mineralogy and Geochemistry* **69**, 403.

- Ramos, F. C., Wolff, J. A. & Tollstrup, D. L. (2004). Measuring  $^{87}\text{Sr}/^{86}\text{Sr}$  variations in minerals and groundmass from basalts using LA-MC-ICPMS. *Chemical Geology* **211**, 135-158.
- Rutherford, M. J. & Hill, P. M. (1993). Magma ascent rates from amphibole breakdown: an experimental study applied to the 1980, 1986 Mount St. Helens eruptions. *Journal of Geophysical Research* **98**, 19667-19685.
- Santo, A. & Peccerillo, A. (2008). Oxygen isotopic variations in the clinopyroxene from the Filicudi volcanic rocks (Aeolian Islands, Italy): Implications for open-system magma evolution. *The Open Mineralogy Journal* **2**, 22-33.
- Santo, A. P. (2000). Volcanological and geochemical evolution of Filicudi (Aeolian Islands, south Tyrrhenian Sea, Italy). *Journal of Volcanology and Geothermal Research* **96**, 79-101.
- Santo, A. P., Jacobsen, S. B. & Baker, J. (2004). Evolution and genesis of calc-alkaline magmas at Filicudi Volcano, Aeolian Arc (Southern Tyrrhenian Sea, Italy). *Lithos* **72**, 73-96.
- Santo, C. Y., Clark, A. H., Farrar, E. & Tsegaye, A. (1995).  $^{40}\text{Ar}/^{39}\text{Ar}$  ages of the Filicudi Island volcanics: implications for volcanological history of the Aeolian Arc, Italy. *Acta Vulcanologica* **7**, 13-18.
- Sisson, T. & Grove, T. (1993). Experimental investigations of the role of  $\text{H}_2\text{O}$  in calc-alkaline differentiation and subduction zone magmatism. *Contributions to Mineralogy and Petrology* **113**, 143-166.
- Spera, F. J. & Bohron, W. A. (2004). Open-system magma chamber evolution: an energy-constrained geochemical model incorporating the effects of concurrent eruption, recharge, variable assimilation and fractional crystallization (EC-EC-RAFC). *Journal of Petrology* **45**, 2459-2480.
- Streck, M. J. (2008). Mineral Textures and Zoning as Evidence for open system processes. *Reviews in Mineralogy and Geochemistry* **69**, 595-622.
- Tranne, C. A., Lucchi, F., Calanchi, N., Rossi, P.L., Campanella, T., Sardella, A. . (2000). Geological map of the island of Filicudi (Aeolian Islands). L.A.C. Firenze.
- Tsuchiyama, A. (1985). Dissolution kinetics of plagioclase in the melt of the system diopside-albite-anorthite, and origin of dusty plagioclase in andesites. *Contributions to Mineralogy and Petrology* **89**, 1-16.

Viccaro, M. (2010). Dynamics of magma supply at Mt. Etna volcano (Southern Italy) as revealed by textural and compositional features of plagioclase phenocrysts. *Lithos*.

Villari, L. & Nathan, S. (1978). Petrology of filicudi, aeolian archipelago. *Bulletin of Volcanology* **41**, 81-96.